Surface modification of graphite electrodes for lithium-ion batteries by chemical and electrochemical approaches

Zur Erlangung des akademischen Grades einer

DOKTORIN DER NATURWISSENSCHAFTEN

(Dr. rer. nat.)

von der KIT-Fakultät für Chemie und Biowissenschaften

des Karlsruher Instituts für Technologie (KIT)

genehmigte

DISSERTATION

von

M. Sc. Marina Bauer

1. Referent: Prof. Dr. Helmut Ehrenberg
2. Referent: Prof. Dr. Patrick Théato

Tag der mündlichen Prüfung: 08.02.2022

Selbstständigkeitserklärung

Hiermit versichere ich, dass ich die vorliegende Arbeit selbstständig verfasst habe, dass ich keine anderen als die angegebenen Quellen und Hilfsmittel benutzt habe, dass ich die wörtlich oder inhaltlich übernommenen Stellen als solche gekennzeichnet habe und dass ich die Satzung des KIT zur Sicherung guter wissenschaftlicher Praxis in der jeweils gültigen Fassung beachtet habe. Die Dissertation wurde bisher an keiner anderen Hochschule oder Universität eingereicht.

Karlsruhe, den 10.01.2022

Marina Bauer

Acknowledgement

This work would not have been possible without the throughout support and contribution of the following:

Therefore, first and foremost I would like to thank Prof. Dr. Helmut Ehrenberg, who gave me the opportunity to work in his group, the greatest possible freedom in working on the topic and always good advice when I needed it.

Thanks to Prof. Dr. Patrick Théato for taking over the second review and for all project-related discussions within the CRC.

Speaking of which, I want to thank the CRC 1176 for financially supporting my work and all its members, who I had good discussions and nice conversations with, especially at workshops. Moreover, Prof. Dr. Christopher Barner-Kowollik, Prof. Dr. Stefan Bräse and Prof. Dr. Michael Meier who gave me access to their labs and devices for organic synthesis and their PhD students who introduced me to the labs.

Thanks a lot to Dr. Frieder Scheiba, who supervised and guided me throughout my PhD, always had an open door and ear for all my matters and gave me maximum freedom with my topic.

Also, I would like to thank Dr. Sonia Dsoke, who always welcomed and included me in her group whenever I worked in MZE and for supporting me during my PhD.

Thanks to the Karlsruhe House of Young Scientists (KHYS) for financing my research project in Dublin.

Many thanks to Prof. Dr. Wolfgang Schmitt for inviting me to his lab at Trinity College in Dublin and always showing his excitement for our mutual project.

Special thanks to the Schmitt group who warmly welcomed me to their group making my stay abroad unforgettable. In particular, I would like to thank Joseph Eiffe, Mariah O'Doherty, Dr. Joaquín Soriano-López, Muhamed Mulahmetović, Dean McCreary, Dr. Sébastien Vaesen and Èadaoin Whelan for their support, especially with the ligand synthesis and all the laughs. I had such a great time! In addition, I would like to thank Dr. John O'Brian for NMR measurements and Dr. Manuel Ruether for device instructions.

Thanks to Prof. Dr. Valeria Nicolosi, for giving me the opportunity to use her lab and equipment for battery testing at Trinity. In this context, I would also like to thank Dr. Sergio Pinillas for his nice guidance in the lab.

Many thanks to my wonderful friends and flatmates in Dublin. I will always have fond memories of our time together.

Thanks to Dr. Oleksandr Dolotko, Dr. Angelina Sarapulova and Dr. Qiang Fu for their great help and support with XRD measurements and analyses. Thanks to Dr. Raheleh Azmi for XPS measurements.

Thanks to all students I worked with and assisted me with practical work. Thank you for good cooperation Philipp Konnerth, Tria Malliaridou, Felix Bauer, Mattes Renner, Eugen Zemlyanushin, Simon Heckmeier, Lucas Faustka and Marcel Häringer.

I am very thankful to Hannes Radinger for lots of helpful discussions, throughout support as well as SEM and XPS measurements.

A big thank you goes to Dr. Xianlin Luo and Dr. Chengping Li for their support and lots fun at and after work. Also, I would like to thank Xianlin Luo for XPS measurements and analysis.

I am extremely grateful to Dr. Kristina Pfeifer for all her support, the discussions and SEM measurements during my PhD. Thank you so much for your help at all times and your throughout friendship. In addition, I would like to thank Dr. Mathias Widmaier for helpful discussions.

Thanks to all colleagues of the IAM-ESS for the nice working atmosphere and many entertaining coffee breaks. Special thanks to my dear colleagues I shared the office with! I would like to thank our secretary Almut Kriese and all technicians for their support with measurements, devices and IT-related issues.

Many thanks to my family and friends from home who helped me to get my mind off work from time to time and for emotionally supporting me.

A big thank you goes to Dr. Günter Staufer for lots of helpful discussion and remarks as well as emotional support.

Last but not least, I want to express my deep gratitude to my brother and especially my mother for their throughout emotional support and always pushing me to my best.

Table of contents

Abbreviations

General

ADS	Aryl diazonium salt
a.u.	Arbitrary unit
b	Basal planes of graphite
CE	Coulombic efficiency
CNT	Carbon nanotubes
COF	Covalent organic framework
COP	Covalent organic polyhedra
CV	Cyclic voltammetry
e	Edge planes of graphite
Eq.	Equivalent
FTO	Fluorine-doped tin oxide
GCPL	Galvanostatic cycling with potential limitation
GNR	Graphene nanoribbon
LIB	Lithium-ion battery
MOF	Metal-organic framework
MOP	Metal-organic polyhedra
PAH	Polyaromatic hydrocarbons
SBR	Styrene-butadiene rubber
SBU	Secondary building unit
SEI	Solid-electrolyte interphase
SHE	Standard hydrogen electrode
v/v	Volume by volume
w/w	Weight by weight

Formulas

$C - rate$	Capacity rate / $1 \cdot h^{-1}$
CE	Coulombic efficiency / %
E_{charge}	Voltage at which charging occurs / V
$E_{discharge}$	Voltage at which discharging occurs / V
E_s	Specific energy / $Wh \cdot g^{-1}$

ε_E	Energy efficiency
F	Faraday constant / 96485 C·mol^{-1}
I	Current / mA·g^{-1} / mA
M	Molecular mass / g·mol^{-1}
m_a	Mass of active material / g
n	Amount of charge carriers
$\frac{dQ}{dV}$	Differential capacity / mAh·V^{-1}·g^{-1}
Q	Charge / mAh·g^{-1}
$Q_{ex.}$	Extracted charge / mAh·g^{-1}
$Q_{in.}$	Inserted charge / mAh·g^{-1}
$Q_{theor.}$	Theoretical capacity of a material / mAh·g^{-1}
t	Time / h
V_c	Cell voltage / V
z	Ionic valency

Chemicals

BTEB	4,4’,4’’-(Benzene-1,3,5-triyltris(ethyne-2,1-diyl)tribenzoic acid
n-BuLi	*n*-Buthyllithium
CMC	Carboxymethyl cellulose
DCM	Dichloromethane
DIPA	Diisopropylamine
DMF	Dimethyl formamide
DMSO	Dimethyl sulfoxide
EC	Ethylene carbonate
H_2BDC	Benzene-1,4-dicarboxylic acid
H_3BTC	Benzene-1,3,5-tricarboxylic acid
H_4BPTC	[1,1’-Biphenyl]-3,3’,5,5’-tetracarboxylic acid
PEEK	Polyether ether ketone
PC	Propylene carbonate
PVdF	Polyvinylidene fluoride
TAP	4,4',4''-(((1,3,5-triazine-2,4,6-triyl)tris(benzene-4,1-diyl))tris(ethyne-2,1-diyl))tribenzoic acid
TBAF	Tetrabutylammonium fluoride

TBAHFP	Tetrabutylammonium hexafluorophosphate
TBATFB	Tetrabutylammonium tetrafluoroborate
THF	Tetrahydrofuran
TIPS	Triisopropylsilyl
TMS	Trimethylsilyl

Analyses

IR		Infrared spectroscopy
	$\tilde{\nu}$	Wavenumber / cm^{-1}
	m	Medium
	s	Strong
	w	Weak
NMR		Nuclear magnetic resonance spectroscopy
	$CDCl_3$	Deuterated chloroform
	DMSO-d6	Deuterated DMSO
	ppm	Parts per million
	δ	Chemical shift / ppm
	d	Doublet
	m	Multiplet
	q	Quartet
	s	Singlet
	t	Triplet
SEM		Scanning electron microscopy
	EsB	Energy-selective backscatter
XPS		X-ray photoelectron spectroscopy
XRD		X-ray diffraction

Figures

Zusammenfassung

Kontrolle über Oberflächeneigenschaften ist in vielen Anwendungen hilfreich, um Materialien aller Art ständig weiterzuentwickeln. Von aktuellem Interesse sind Lithium-Ionen-Batterien (LIBs), da sie derzeit der am häufigsten verwendete Batterietyp sind, um den Bedarf an Energiespeicherung in tragbaren Geräten oder Elektrofahrzeugen zu decken. Dennoch gilt es immer noch Herausforderungen zu bewältigen, z. B. den irreversiblen Lithium-Ionen-Verlust aufgrund der Bildung der Festkörper-Elektrolyt-Interphase (SEI) auf Graphitelektroden. Die Funktionalisierung der Graphitoberfläche ist ein nützlicher Ansatz, um ein besseres Verständnis über SEI-Bildung und Batterieleistung in LIBs zu erlangen. In dieser Arbeit werden verschiedene Konzepte für die Oberflächenfunktionalisierung von Graphit und die Leistung als negative Elektrode in LIBs untersucht, um neue Informationen auf diesem Gebiet zu liefern.
Durch Electrografting und *in situ* grafting von Aryldiazoniumsalzen (ADS) wurden Ethinyl-, Amino-, Carboxy- und Nitrogruppen auf die Graphitoberfläche aufgebracht. Die Ethinylgruppen wurden durch Alkylsilylgruppen geschützt, die nach dem Graftingprozess entfernt wurden. Die Nachteile der electrogegrafteten und insbesondere der entschützten Proben wurden bewertet und mit den entsprechenden *in situ* gegrafteten Proben verglichen. Während elektrogegraftete Proben die Delithierungskapazitäten tendenziell verringern, weisen *in situ* gegraftete Proben (mit Ausnahme der Aminogruppen) höhere Kapazitäten auf. Außerdem war die Coulombsche Effizienz des ersten Zyklus bei *in situ* gegrafteten Proben höher. *In situ* gegraftete Ethinylgruppen zeigen sogar eine bessere Zyklenstabilität bei hohen Raten als die unbehandelte Graphitelektrode. In einem anderen nicht-kovalenten Ansatz wurde die Verwendung von kommerziell erhältlichen funktionalisierten Pyrenen als Additiv für Graphitelektroden einerseits und als adsorbierte Spezies andererseits untersucht. Die untersuchten funktionellen Gruppen waren Carboxy, Butylcarboxy, Amino und Butylamino. Als Additiv zeigen die Pyrene bei niedriger Stromdichte eine ähnliche Leistung wie die unbehandelte Graphitelektrode, verschlechtern sich jedoch bei höherer Stromdichte. Die adsorbierten Pyrene zeigen bei Pyren, Amin und Carboxy bereits bei niedrigen Stromdichten eine Verschlechterung der Delithierungskapazitäten, während Butylamin und Butylcarboxy bei hohen Stromdichten besser abschneiden als in der Additiv-Variante. Für Butylcarboxy wurden höhere Kapazitäten und eine verbesserte Zyklenstabilität bei hohen Stromdichten erreicht. Abschließend wurde ein Ansatz mit metallorganischen Gerüststrukturen (MOFs) untersucht. Dieser Teil umfasst das Wachstum von zwei Zn-basierten MOFs mit Carboxyl-Linkern in Kombination mit Graphit. MOF-modifizierte Graphitelektroden wurden sowohl vor als auch nach Karbonisierung untersucht. Mit getempertem MOF-modifiziertem Graphit wurde eine verbesserte Zyklenstabilität bei hohen Stromdichten erreicht. Der Zn-MOF mit dem kleineren Liganden zeigte die höchste Stabilität ohne vorheriges Karbonisieren.

Abstract

Control over surface properties is desired in many applications to constantly develop all kinds of materials. A recent area of interest is lithium-ion batteries (LIBs), as up-to-date they are the most used battery-type to cover the demand of energy storage in portable devices or electric vehicles. Nevertheless, challenges to face remain, for instance, the irreversible lithium-ion loss due to the formation of a solid-electrolyte interphase (SEI) on graphite electrodes. The functionalisation of the graphite surface is a useful approach to gain a better understanding of SEI formation and battery performance in LIBs. This work examines different concepts for surface functionalisation of graphite and the performance as negative electrode in LIBs, to provide new information in this field.

Electrografting and *in situ* grafting of aryl diazonium salts (ADS) were performed to introduce ethynyl, amino, carboxy and nitro groups to the graphite surface. Ethynyl groups were protected by alkyl silyl groups, which were removed after the grafting process. The drawbacks of electrografted and especially deprotected samples were evaluated and compared to corresponding *in situ* grafted samples. While electrografted samples tend to lower the delithiation capacities, *in situ* grafted samples (except amino groups) reveal higher capacities. Additionally, the Coulombic efficiency of the first cycle was enhanced for *in situ* grafted samples. *In situ* grafted ethynyl groups even show a better cycling stability at high rate compared to the pristine graphite electrode. In a different non-covalent approach, the use of commercially available functionalised pyrenes as additive for graphite electrodes on the one hand and as adsorbed species on the other hand is addressed. The functional groups under investigation were carboxy, butylcarboxy, amino and butylamino. As additive, the pyrenes show similar performance to the pristine graphite electrode at low current densities but deterioration at higher current densities. Adsorbed pyrenes show degradation of delithiation capacities already at low current densities for pyrene, amine and carboxy, but butylamine and butylcarboxy perform better at high current densities compared to the additive variant. For butylcarboxy higher capacities and enhanced cycling stability was achieved at high current densities compared to the pristine graphite electrode. Finally, graphite functionalisation using metal-organic frameworks (MOFs) was studied. This part includes the growth of two Zn-based MOFs with carboxylic linkers in combination with graphite. The MOF-modified graphite electrodes itself but also after a carbonisation step were investigated. Enhanced cycling stabilities at high current densities were achieved with the carbonised MOF-modified graphite electrodes. The Zn-MOF with the smaller ligand showed the highest stability without prior carbonisation.

1. Introduction

Tailoring the properties of surfaces is of high interest in many applications. Water-repellent clothes for outside activities, anti-corrosion coatings for cars, non-stick coated pans or - on given occasion - antiviral door handles are just a few examples from everyday life, where surface treatments have become essential. To obtain the desired characteristics, the bulk material is functionalised with suitable modifiers. A very relevant example and target for surface modifications are lithium-ion batteries (LIBs).

Ever since the commercialisation by Sony in 1991,[1, 2] LIBs have conquered the society and in 2019, the work on the development of LIBs by Stanley Whittingham, Akira Yoshino and John Goodenough was awarded with the Nobel Prize for chemistry[3]. Light weight and high energy density compared to other battery systems, make LIBs the first choice in various applications.[4] They are used to power mobile phones, laptops, electric vehicles and to store energy from renewable sources. Facing climate change and the required energy revolution, convincing energy storage systems to counterbalance the fluctuation of available energy provided by renewable sources and power electric vehicles that can compete with combustion engines are needed. Therefore, it is of high interest to permanently improve the performance of LIBs

Up to date, graphite is the material of choice for negative electrodes in commercial LIBs.[1, 2, 5, 6] However, irreversible lithium-ion loss and capacity fading during the charging process due to electrolyte decomposition on the graphite surface is a major drawback.[7] On the other hand, the decomposition leads to the formation of a layer with protective features,[7] making the graphite surface an ideal target for surface modification to prevent irreversible lithium-ion loss but preserve the protective properties. Common strategies to address this issue are chemical, thermal or electrochemical treatment of the graphite active material itself.[7] Although these approaches achieved enhanced performance of graphite electrodes, the control over the surface composition is not very precise. Therefore, the elucidation of the underlying mechanisms is rather difficult.

This work focuses on an alternative method to achieve graphite surfaces with high control over certain surface groups to give a deeper insight and understanding into the structure-property-relation. Instead of a pre-treatment of native graphite surface groups, anchor molecules with defined functionalities are introduced to the graphite surface. This thesis encompasses covalent approaches using aryl diazonium salts and a non-covalent approach with pyrenes as anchor molecules. Moreover, the possibilities of metal-organic frameworks as a surface-covering network are investigated. The electrochemical behaviour of the modified graphite as electrodes in LIBs is under study. The following Chapter 2 gives an overview of the relevant basics concerning LIBs and the modifier's chemistry, before Chapter 3 will elaborate their potential for the modification of graphite electrodes for LIBs.

2. Theoretical background

2.1 Lithium-ion batteries

Rechargeable batteries are indispensable in many areas of daily lives and the demand is constantly increasing. The combination of high gravimetric and volumetric energy density, low self-discharge and long cycle life let lithium-ion batteries (LIBs) occupy an important position amongst rechargeable battery systems.[4] In Table 1, these characteristics of LIBs are compared to lead-acid, nickel-cadmium (Ni-Cd) and nickel-metal hydride (Ni-MH) batteries.

Table 1. Characteristics of LIBs, Lead-acid batteries, Ni-Cd batteries and Ni-MH batteries. Adapted and modified from [4].

	LIB	**Lead-acid battery**	**Ni-Cd battery**	**Ni-MH battery**
Gravimetric energy density [Wh·kg^{-1}]	170 – 250	30 – 50	40 – 60	60 – 120
Volumetric energy density [Wh·L^{-1}]	350 – 700	60 – 110	150 – 190	140 – 300
Self-discharge per month [%]	<10	5	20	30
Cycle life (to 80% of the initial capacity)	500 – 2000	300	1500	1000

Nevertheless, the development of LIB technology is of high importance to further improve portable devices, electric vehicles and the storage of renewable energy. The following subchapters 2.1.1 – 2.1.3 give an overview of the relevant basics of LIBs with a special focus on graphite as negative electrode material.

2.1.1 Components and working principle

A LIB consists of a negative and a positive electrode soaked in electrolyte and divided by a separator. The negative electrode of a LIB is often referred to as anode and the positive electrode as cathode, even though this is only true for the discharging process.[8] The electrodes should deliver high capacities and offer a large voltage window to achieve high energy densities.[9, 10] In this regard lithium metal is an optimal candidate for the negative electrode providing a theoretical capacity of 3861 mAh·g^{-1} and a standard potential of –3.04 V *vs.* SHE.[11, 12] However, dendrite formation over cycling and the resulting safety issues only allow their usage in non-rechargeable lithium-metal batteries.[11] Therefore, commercial LIBs resort to graphite as negative electrode material, which provides a theoretical capacity of 372 mAh·g^{-1} and a lithium-ion intercalation potential down to 0.01 V *vs.* Li$^+$/Li.[2] A more detailed review for graphite as active material in LIBs is discussed in chapter 2.1.3. For the positive

electrode, the most common materials are layered oxides such as $LiCoO_2$. Besides the active material, battery electrodes consist of conductive additive and a polymeric binder, for example polyvinylidene fluoride (PVdF) or carboxymethyl cellulose (CMC) and are attached to a current collector like copper or aluminium foil. Since the conductive additive and the polymeric binder are electrochemically inactive, their amount is supposed to be kept to a minimum. The electrolyte usually is a lithium salt like $LiPF_6$ in a mixture of cyclic and aliphatic organic carbonates, which enables lithium-ion transport between the electrodes. To prevent an electrical short-circuit the electrodes have to be physically separated by a lithium-ion permeable separator. Common materials are microporous polymer films.[8]

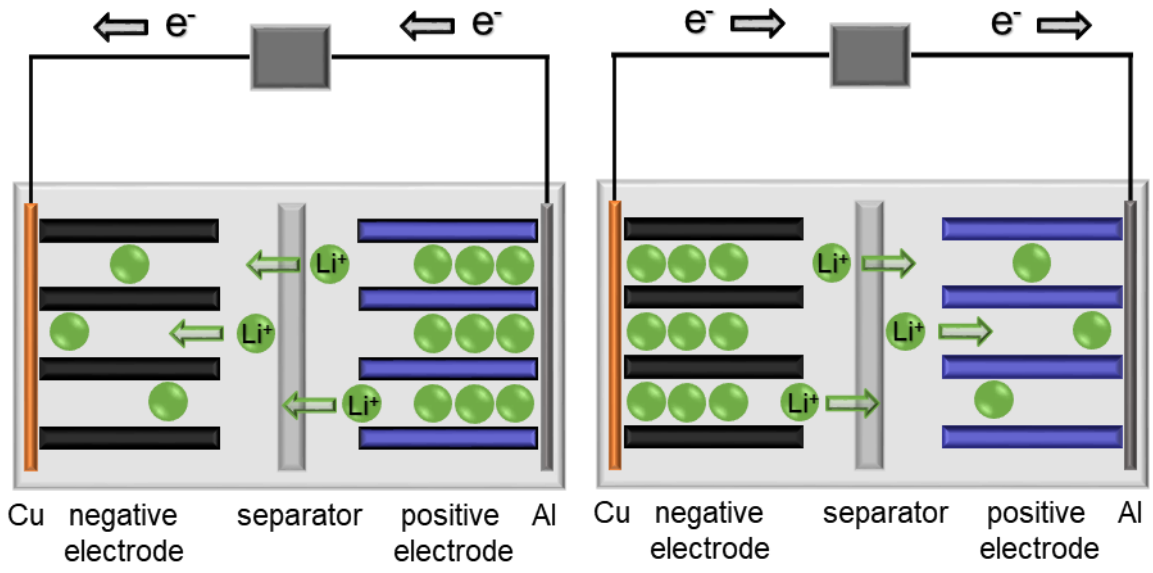

Figure 1. Working principle of a lithium-ion battery during charging (left) and discharging (right). Adapted and modified from [13].

To charge the battery a current is applied between the electrodes to extract lithium-ions from the positive electrode and insert them into the negative electrode *via* the electrolyte. During this process, the positive electrode is oxidised, whereas the negative electrode is reduced. All processes occur *vice versa* for the discharge of the battery, meaning lithium-ions are extracted from the negative electrode and inserted into the positive, whilst the negative electrode is oxidised and the positive is reduced. The discharge process is driven by the potential difference of the electrodes and therefore occurs spontaneously. As a result, the electrons flowing through the external circuit are available to perform electrical work.[14] A schematic diagram of both processes is shown in Figure 1.

Considering a LIB with graphite as negative electrode and $LiCoO_2$ as positive electrode, the corresponding redox reactions are:[15]

$$positive\ electrode: \quad LiCoO_2 \rightleftharpoons Li_{0.5}CoO_2 + 0.5\,Li^+ + 0.5\,e^- \tag{1}$$

$$negative\ electrode: \quad C_6 + Li^+ + e^- \rightleftharpoons LiC_6 \tag{2}$$

In this case, the lithium-ions intercalate and deintercalate back and forth between layered host structures. Therefore, this type of battery is referred to as “rocking-chair” battery.[1], [16]
Besides intercalation, the negative electrode can be lithiated *via* conversion or alloying mechanisms. Conversion mechanism means, lithium-ions are inserted into binary compounds, *e.g.* a transition metal oxide, to form the corresponding lithium oxide while the transition metal is reduced. Alloying mechanism means, lithium-ions are inserted into a host element, *e.g.* silicon, to form the corresponding Li-Si alloy.[17], [18]

2.1.2 Galvanostatic cycling

A common technique to determine the electrochemical performance of an electrode is galvanostatic cycling, where a constant current is applied between a working (electrode under study) and a counter electrode (usually lithium metal). To only characterise the working electrode’s behaviour, a three-electrode setup with a currentless reference electrode is required.
At constant current I the relation between time t and charge Q is:

$$Q\ [mAh \cdot g^{-1}] = I\ \cdot t \tag{3}$$

The charge $Q_{in.}$ inserted into and $Q_{ex.}$ extracted from the battery quantifies the battery’s capacity. The theoretical capacity $Q_{theor.}$ of a material is calculated considering the amount of charge carriers n, the Faradaic constant F, the ions’ valency z and the molecular mass M:

$$Q_{theor.}\ [mAh \cdot g^{-1}] = \frac{n \cdot F \cdot z}{M} \tag{4}$$

The applied current I is commonly expressed as capacity-rate (C-rate), which includes the theoretical capacity $Q_{theor.}$ of the active material:

$$C-rate\ [\frac{1}{h}] = \frac{I}{Q_{theor.}} = \frac{\frac{Q_{theor.}}{t}}{Q_{theor.}} = \frac{1}{t} \tag{5}$$

The current that is needed to fully charge the cell within an hour is therefore described as 1C. Another important parameter is the Coulombic efficiency (CE), which is given by the ratio of extracted charge $Q_{ex.}$ to inserted charge $Q_{in.}$:

$$CE\ [\%] = \frac{Q_{ex.}}{Q_{in.}} \cdot 100 \qquad (6)$$

The CE gives information about the reversibility of capacity and loss of charge due to irreversible side reactions. Cell setups with lithium metal as counter electrode provide an unlimited lithium-ion source. Therefore, the CE cannot give information about the net lithium-ion loss.[19] However, it allows a comparison between different working electrodes.

In galvanostatic cycling experiments the potential is measured as a function of time in a defined voltage range by applying a well-defined current. Hence, the capacities and CEs of a material can be extracted from the measurement according to Equation (3) and (6). Furthermore, the capacity retention after several cycles can be determined.

Elucidation of insertion/extraction potentials and determination of side reactions is possible by plotting the differential capacity $\frac{dQ}{dV}$ *versus* voltage, where redox reactions appear as peaks. A specific example is visualised and explained at the end of the following Chapter 2.1.3.

2.1.3 Graphite as active material

Graphite is a natural occurring allotrope of carbon and consists of sp^2 hybridised graphene layers, which are connected by *π-π* interactions and weak van der Waals forces. The layers are stacked in the order ABAB or ABCABC and exhibit edge (e) and basal (b) planes (Figure 2, left and middle). Mechanical, thermal and electrical properties vary along edge and basal planes making graphite an anisotropic material. Graphite is able to intercalate one lithium-ion per six carbon atoms leading to the formation of AA stacked LiC_6 (Figure 2, right), which entails a reversible volume change of ~ 10 %.[2] The lithium-ions intercalate through the edge sites of graphite. Intercalation through basal planes is only possible at defect sites.[2], [20]

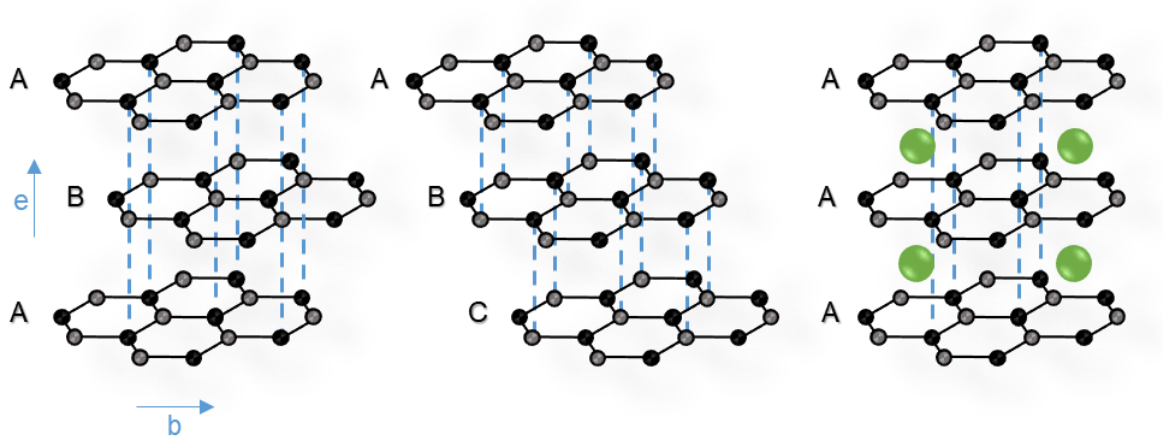

Figure 2. ABA (left) and ABC (middle) stacking of graphite and AA stacking in LiC6. Adapted and modified from [21].

The interplay of required energy to expand the van der Waals gap between graphene layers and the repulsion between lithium-ions leads to a staging mechanism during intercalation. The voltage-depending stages of lithium-ion intercalation have been reported in the literature.[2], [20] Mainly, two different four-stage intercalation models are discussed provided by Rüdorff and Hofmann[22] and Daumas and Hérold[23] (Figure 3). According to the Rüdorff-Hofmann model the layers are filled up one by one. In stage four every fourth layer is lithiated, in stage three every third, in stage two every second and in the final stage one every layer, which corresponds to LiC_6. Since inter-basal diffusion is rejected, this model fails to describe the stage transitions, because lithium-ions would have to be de- and re-intercalated. Hence, Daumas and Hérold presented an alternative model, where the layers form flexible islands around the intercalated lithium-ions, while preserving the number of empty layers between intercalated layers.

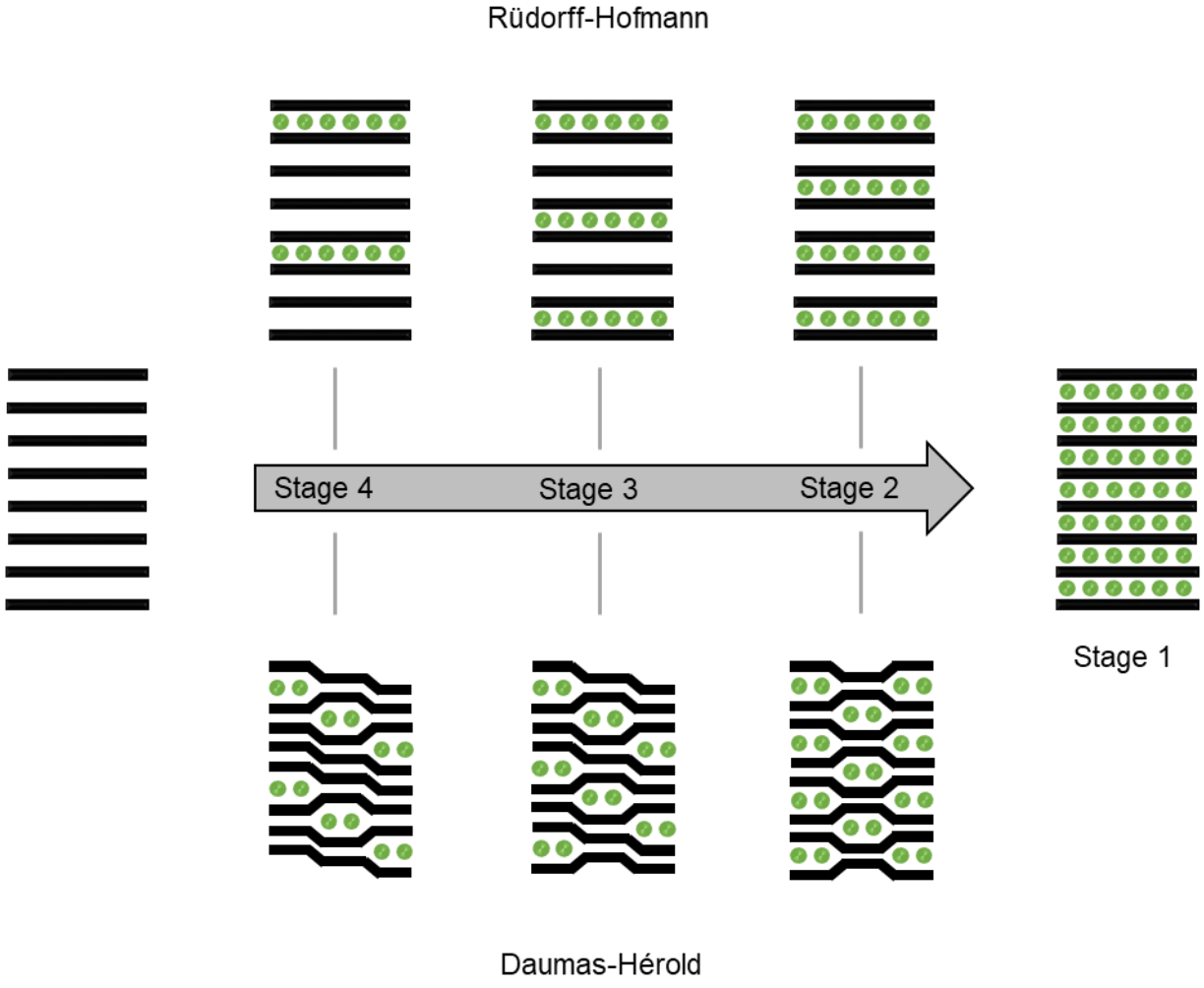

Figure 3. Schematic representation of the Rüdorff-Hofmann (upper part) and the Daumas-Hérold (lower part) model. Adapted and modified from [2].

However, those models do not consider the influence of defects in the graphitic structure, which play an important role as described by White *et al*.[24]

Plotting the potential against time or capacity visualises the stage transition (coexistence of two phases) as potential plateaus[2, 25], whereas differential capacity plots display them as peaks (Figure 4).

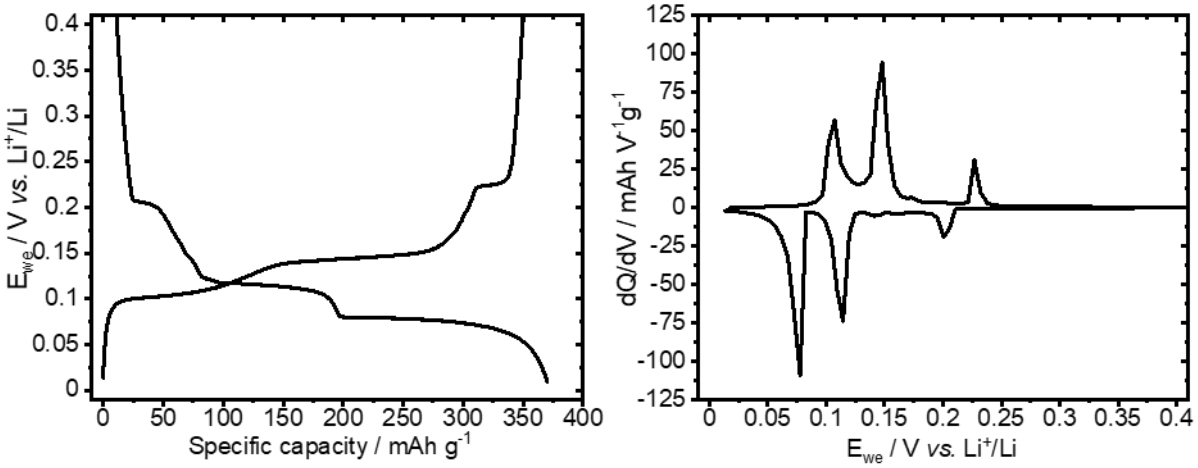

Figure 4. Voltage profile (a) and differential capacity plot (b) of the second cycle of a graphite electrode measured *vs.* lithium metal at C/10.

A theoretical capacity of 372 mAh g^{-1} can be calculated using Equation (4), which is higher than the capacity of the most common positive electrode materials.[2] Even though, conversion- or alloying-type negative electrode materials exhibit even higher capacities, disregarding lithium metal, graphite provides lower de-/lithiation potentials (0.25 – 0.01 V *vs.* Li^+/Li).[2] To achieve a high cell voltage, the negative and positive electrode should feature low and high de-/lithiation potentials, respectively.[26] A high battery capacity and cell voltage are again desired to yield in a high specific energy of the battery (Equation (7), E_s = specific energy, m_a = mass of active material, V_c = cell voltage, I = current, t = time)[10].

$$E_s = \frac{1}{3600 \cdot m_a} \int V_c \, I \, dt \tag{7}$$

$$\varepsilon_E = \frac{E_{discharge}}{E_{charge}} \tag{8}$$

In addition, conversion and alloying-type materials often suffer from extensive volume expansion during cycling[27] (*e.g.* +300 % for lithium-silicon alloys)[28]. Another quality of graphite as negative electrode material is the low voltage hysteresis.[2] This means that the difference between the voltage at which charging and the voltage at which discharging occurs is low (compared to conversion-type materials for example).[29] Equations (7) and (8) (ε_E = energy efficiency)[10] show that the lower the voltage hysteresis the better the energy efficiency of the battery (granted that the Coulombic efficiency is consistent).

2.1.4 Solid-electrolyte interphase

As already mentioned in Chapter 2.1.1, the electrolyte in LIBs is commonly a lithium salt in aliphatic and cyclic organic carbonates. The commercially available electrolyte used in this work consists of 1 M $LiPF_6$ in a 50:50 % v/v mixture of ethylene carbonate (EC) and dimethyl carbonate (DMC). The purpose of the electrolyte is to guarantee good lithium-ion conductivity between the electrodes. Therefore, the solvents should have low viscosity and a high dielectric constant to dissolve $LiPF_6$. EC fulfils these requirements but is solid at room temperature hence it is mixed with DMC.[30]

The downside of organic carbonates is their thermodynamic instability at low potentials *vs.* Li^+/Li.[2], [7] The electrochemical stability window of an electrolyte is determined by its reduction and oxidation potential. As soon as the electrochemical potential of the negative electrode is above the reduction potential of the electrolyte, the electrolyte will be reduced (Figure 5).[31] As mentioned earlier in Chapter 2.1.1 lithium-ion insertion occurs down to 0.01 V *vs.* Li^+/Li, which enables high cell voltages and hence high energy densities. However, organic carbonates are only stable above ~0.8 V *vs.* Li^+/Li and thus are reduced during the charging process.[2]

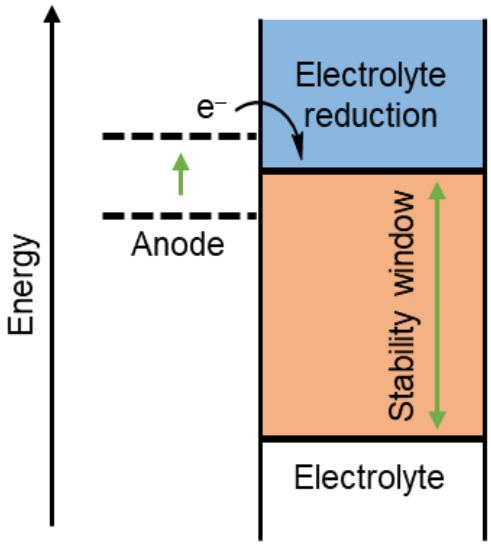

Figure 5. Electrochemical stability of the electrolyte. Adapted and modified from [31].

Decomposition products of electrolyte components lead to the formation of an interphase at the electrode-electrolyte interface.[2], [7], [32] This phase has properties of a solid electrolyte and was accordingly named solid-electrolyte interphase (SEI) by Peled.[32] The formation of the SEI leads to irreversible consumption of lithium-ions. The lithium-ion sources are not only lithium-ions extracted from the positive electrode during charging, but also the electrolyte salt.[33]

Close to the graphite surface, the inner SEI consist of inorganic compounds (like Li_2O, Li_2CO_3 and LiF)[2], [34], resulting from electrolyte salt decomposition, whereas the outer SEI consists of organic compounds (like semi carbonates and poylolefines)[2], [34], resulting from solvent decomposition (Figure 6).[2], [7] The outer organic layer of the SEI is often described as porous

and permeable for lithium-ions, electrolyte salt anions and solvent molecules. However, the inner inorganic layer is described as a dense electron-insulating layer only permeable for lithium-ions, which prevents electron tunnelling and hence further electrolyte decomposition.[35] The irreversible consumption of lithium-ions for SEI formation results in capacity loss and poor CE loss (see Equations (3) and (6)). About 10 % of the original capacity is consumed for SEI formation. Besides, the loss of lithium-ions from the electrolyte salt lowers the mass transport and increases the electrolyte resistance.[33]

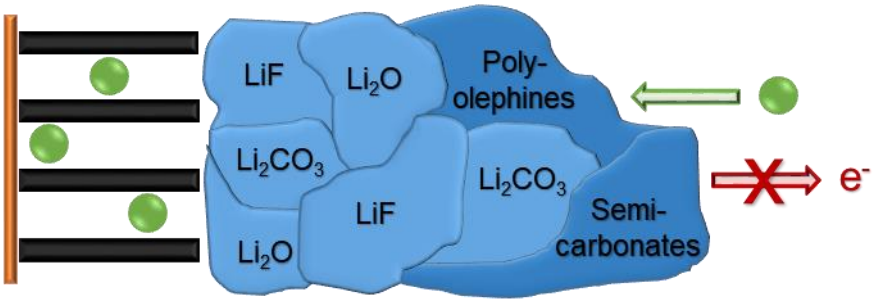

Figure 6. Schematic diagram of inorganic and organic components of the SEI on a graphite electrode. Adapted and modified from [34].

Nevertheless, it acts as a protective layer towards further electrolyte decomposition. In fact, EC is known to form a stable SEI layer on graphite enabling stable cycling of the battery.[2] Before this discovery, propylene carbonate (PC) was used in electrolytes. PC-based electrolytes led to solvent co-intercalation and exfoliation of graphite, as well as ongoing solvent decomposition.[2], [33], [36] This example shows that it is of vital importance that the lithium-ions strip off their solvation shell before they intercalate into graphite.[37]
An ideal SEI features the following properties:[33]

- high electrical resistance
- high lithium selectivity and permeability
- low thickness
- high strength and tolerance to expansion and contradiction
- insolubility in the electrolyte
- stability in a wide temperature and potential range

The natural SEI has a heterogeneous composition and the mechanisms and influencing factors of its formation are not fully understood yet. However, the edge and defect sites of graphite are highly reactive and although electrolyte decomposition also occurs on basal planes, the decomposition is favoured at the edge and defect sites.[33] Therefore, the composition of the graphite surface is a crucial factor, when it comes to SEI formation.

2.2 Surface modifications

Chapter 2.1.4 showed that the surface of graphite electrodes plays an important role, when they are cycled in carbonate-based electrolytes. Hence, several attempts have been made to tune the graphite surface and investigate the influence on the electrochemical behaviour in LIBs.

Ng *et al.*[38] for instance heat treated graphite under vacuum and found that the first irreversible capacity loss and voltage plateaus are very similar to the untreated graphite. The irreversible losses were 15 % and 14 %, respectively (Table 2). Temperature-programmed desorption analysis revealed that the heat-treated graphite still bears surface oxygen groups, which was assigned to interaction of the heat-treated sample with ambient air. When the heat-treatment was followed by a hydrogen-treatment, temperature-programmed desorption analysis showed a negligible amount of surface oxygen groups compared to the only heat-treated and untreated graphite. Looking at the first (de)lithiation cycle of the heat- and hydrogen-treated sample, they observed exfoliation of the graphite and an accompanying increased irreversible capacity loss of 24 %, proving that surface oxygen groups are of vital importance for the formation of an effective SEI.[38]

Table 2. Correlation of the presence of surface oxygen groups on graphite with irreversible capacity loss of the first cycle and exfoliation. Adapted and modified from [38].

Graphite	Surface oxygen groups	Irr. capacity loss (first cycle)	Exfoliation
Untreated	yes	14 %	no
Heat-treated	yes	15 %	no
Heat-treated + H_2	negligible	24 %	yes

Apart from thermal treatment, chemical treatment has been discussed in literature as well. Chemical reduction of graphite (e.g. with *n*-butyllithium) leads to less first cycle irreversible capacity loss, since the native surface groups of graphite cannot be further reduced upon cycling. The cycling stability however, is deteriorated because the SEI is less effective. In contrast, chemical oxidation of graphite (e.g. with $KMnO_4$) leads to higher first cycle irreversible capacity loss.[39] Wu *et al.*[40] reported enhanced cycling stability and first cycle efficiency for chemical (and thermal) treated graphite.

These treatments revealed valuable information about the relation of surface groups on graphite and SEI formation. Nevertheless, there is a variety of different native surface groups present on graphite, where thermal and chemical treatments cannot target precise surface composition. To obtain certain functionalities on the graphite surface, thermal and chemical treatment is therefore not ideal. Incorporation of certain functional groups can be better achieved by grafting of anchor molecules. In this context, aryl diazonium salts have proved to be useful. The grafting of *para*-substituted aryl diazonium salts results in covalent bonds

between the aryl and graphite, where the functional groups are orientated perpendicular to the basal planes of graphite. An alternative are pyrenes, where the interaction with graphite is of non-covalent nature and functional groups directly attached to the pyrene moiety are orientated in parallel to basal plane of graphite. However, the surface modification of graphite is not limited to the attachment of small anchor molecules bearing functional groups. The growth of structural networks is an option as well. For this purpose, metal-organic frameworks (MOFs) represent a suitable material class due to their adjustable composition and porosity. The following Subchapters 2.2.1 – 2.2.3 give an overview of the relevant basics of each material class.

2.2.1 Aryl diazonium salts

The general structure of diazonium salts is $R–N_2^+X^-$, where R is an aliphatic or aromatic moiety and X^- is an organic or inorganic anion. Aromatic diazonium salts are much more stable than aliphatic diazonium salts due to resonance stability and the lower stability of resulting phenyl cation when nitrogen is released. Hence, the use of aromatic aryl diazonium salts dominates the literature and therefore the focus will be on aromatic aryl diazonium salts in the following. A general overview of reactions with aryl diazonium salts can be found in [41], including Sandmeyer chemistry and synthesis of azo dyes for example. Diazotisation of aromatic amines in acidic media is the most common method to synthesise aryl diazonium salts.[42] Since numerous aromatic amines are commercially available, the synthesis of aryl diazonium salts is straightforward in most cases.[43] However, the isolation of aryl diazonium salts should be carried out with caution, since especially aryl diazonium chlorides tend to violently decompose. Aryl diazonium tetrafluoroborates on the other hand are more stable and some of them can even be purchased commercially.[44]

Great attention has been drawn to aryl diazonium salts as surface modifiers since Pinson *et al.*[45] investigated their electrochemical reduction on carbon surfaces in 1992. The purpose of their work was to provide an opportunity to modify carbon surfaces without having to oxidise them during the modification, which often results in poor control of surface groups and even corrosion of the substrate. They showed that reductive electrografting of aryl diazonium salts enables strong covalent bonds between the aryl and the carbon surface. Their work created a new possibility to introduce a large variety of functional groups.[45] Not only carbon surfaces but also semiconductors and metals have been modified with aryl diazonium salts ever since.[46]

Several methods are available to achieve the grafting of aryl diazonium salts. Those include electrochemical and non-electrochemical methods as well as the use of isolated aryl diazonium salts and *in situ* generated aryl diazonium salts.[47]–[52]

The mechanism of electrografting *via* a one-electron transfer is shown in Figure 7. An aryl radical is generated *via* homolytic dediazoniation by applying an external potential. The aryl radical reacts with the surface to form a covalent bond.[46], [53] Without a steric demanding

functional group the formation of multilayers is possible *via* three mechanisms displayed in Figure 7 (red, green and blue pathway).[50] The red pathway is again a radical mechanism, whereas the green and blue pathway underlie an electrophilic attack of a carbocation or an aryl diazonium ion, respectively.

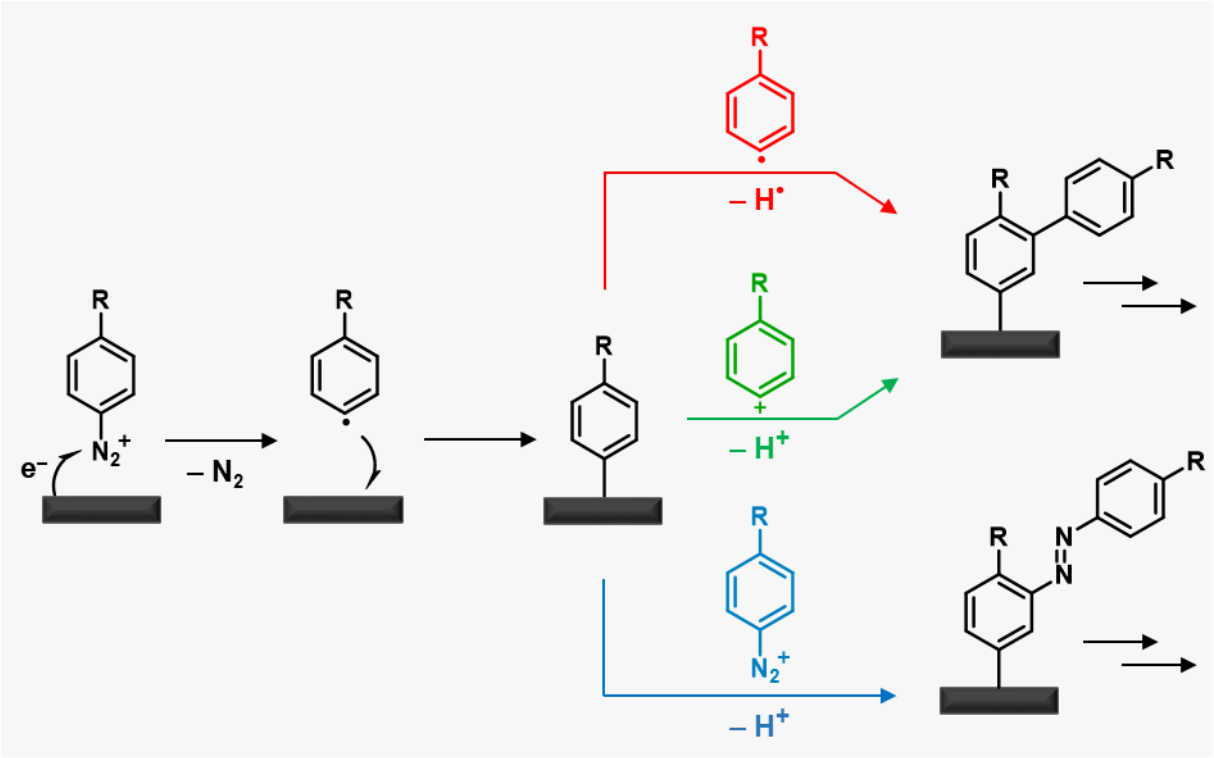

Figure 7. Grafting mechanism of aryl diazonium salts and mechanisms of multilayer formation. Adapted and modified from [53] and [50].

Dediazoniation without electrochemical initiation can be homolytic to form aryl radicals as well or heterolytic to form aryl cations. The occurring mechanism depends on the solvent and the functional group.[54]

Easy synthesis, a variety of modification methods and substituents and the formation of stable, covalent bonds between the aryl and the carbon surface, make aryl diazonium salts an excellent choice for modifying graphite surfaces.

2.2.2 Pyrenes

Pyrene is a representative of polycyclic aromatic hydrocarbons (PAHs) and consists of four condensed aromatic rings. As reported by Grimme[55] *π-π* interactions between PAHs become significant for molecules with 10–15 carbon atoms, making pyrene ($C_{16}H_{10}$) an excellent candidate for non-covalent modification of carbon surfaces. *π-π* interactions are possible in three different arrangements of aromatic rings to one another. Those are face-to-face (stacked), edge-to-face (T-shape) and offset (parallel displaced), whereas the face-to-face arrangement is the least favourable for non-substituted aromatic rings.[56] Figure 8 displays the different arrangements schematically.

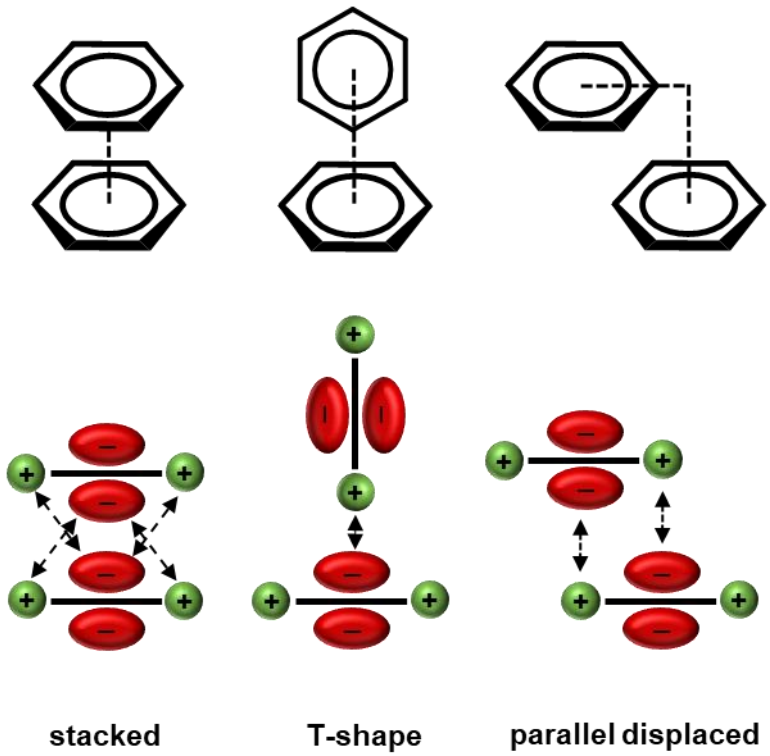

Figure 8. π-π-Stacking arrangements between PAHs. Adapted and modified from [56].

Four basic structural types are defined for PAHs, differing in the relationship of C–C and C–H interactions between the molecules: the herringbone, sandwich herringbone, *γ* and *β*-structure.[57] Figure 9 shows the structure types and a representative PAH for each. Pyrene is attributed to the sandwich herringbone structure.[57]

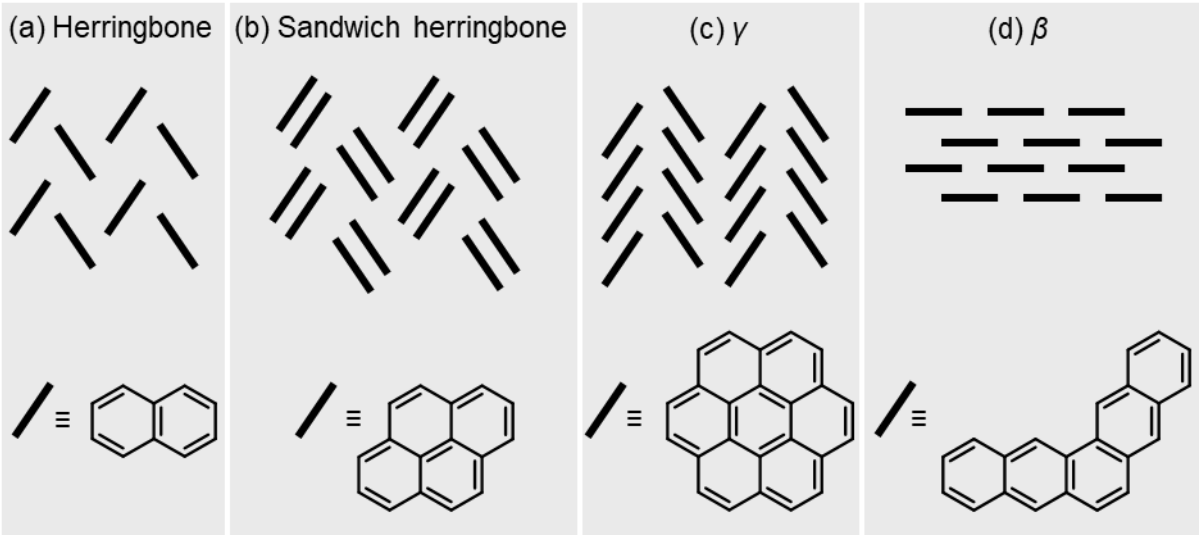

Figure 9. Structural types of PAHs. Adapted and modified from [58].

Upon adding polar functional groups such as carboxy or amino to the pyrene structure hydrogen bonding has to be taken into account as well.

2.2.3 Metal-organic frameworks

Together with metal-organic polyhedra (MOPs), covalent organic polyhedra (COPs) and covalent organic frameworks (COFs), metal-organic frameworks (MOFs) are representatives of reticular chemistry, where molecular building units are linked together to form discrete extended structures. In general, MOFs consist of inorganic secondary building units (SBUs) and organic linkers.[59] SBUs are typically polynuclear metal clusters, which are preferred over single metal-ions because of their rigidity and directionality. Organic linkers are mostly of anionic or neutral nature, whereas anionic linkers have the advantage of neutralising the positive charge of the SBU and formation of stronger bonds with the metals in SBUs. Carboxylates are a very prominent example for such anionic linkers.[60]

The number of carboxy groups defines the binding topicity of the ligand. Figure 10 shows an example for a ditopic (H_2BDC = benzene-1,4-dicarboxylic acid), tritopic (H_3BTC = benzene-1,3,5-tricarboxylic acid) and tetratopic ligand ([1,1'-biphenyl]-3,3',5,5'-tetracarboxylic acid), respectively.[60]

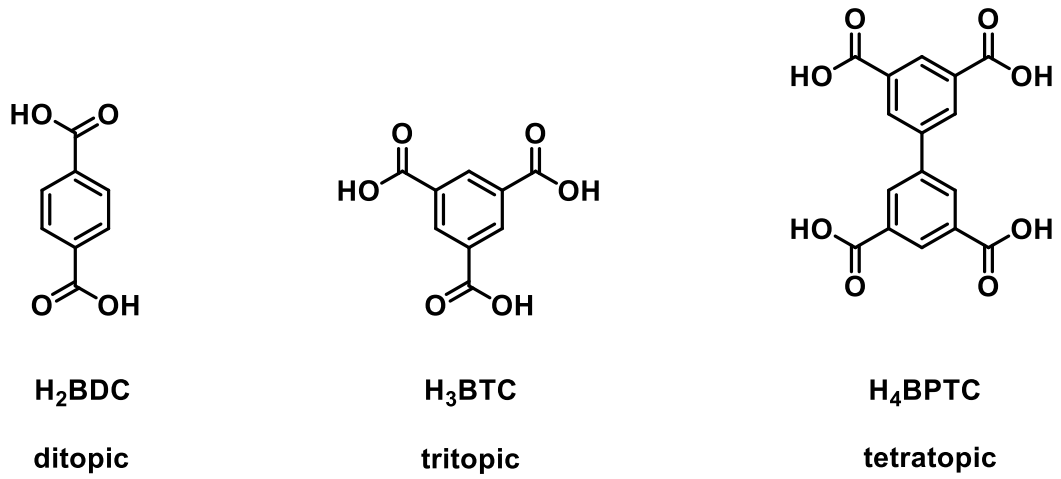

Figure 10. H_2BDC, H_3BTC and H_4BPTC as examples for di-, tri- and tetratopic carboxlate ligands. Adapted and modified from [60].

Organic linkers of different sizes, orientation and geometries are usually synthesised *via* coupling reactions followed by deprotections and consist of core units, extending units and binding groups. Structural examples of those units are shown in Figure 11.[60] In this work 1,3,5-trisubstituted phenyl and 2,4,6-trisubstituted-1,3,5 triazine are used as core units, 1,4-disubstituted phenyls and alkynes as extending units and carboxylates as binding groups.

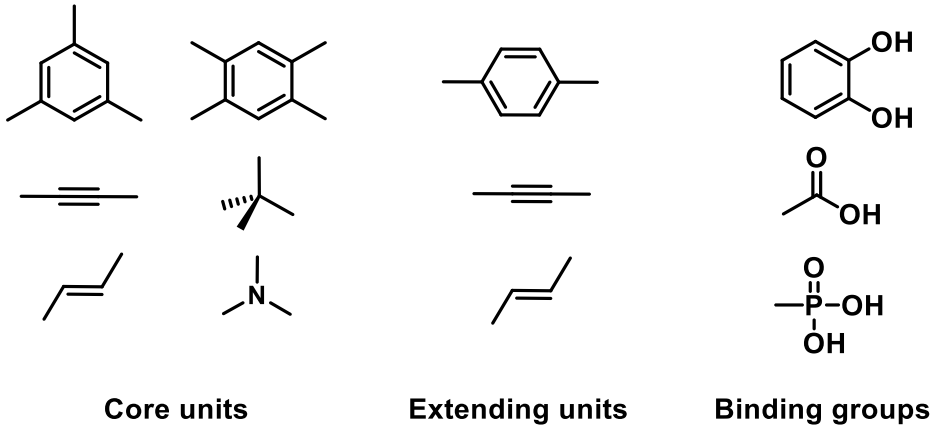

Figure 11. Examples for core units, extending units and binding groups for MOF ligands. Adapted and modified from [60].

The most common synthesis method for MOFs is solvothermal synthesis. Even though solvothermal implies reaction at high temperatures (10 – 1000 °C) and pressures (1 – 100 MPa),[61] in literature the term is also used for synthesis at elevated temperatures and atmospheric pressure.[62]–[66] Solvents are often dialkylformamides, like dimethylformamide (DMF). DMF slowly decomposes under formation of dimethylamine and formic acid upon heating (Figure 12). Dimethylamine deprotonates the carboxylic groups of the linker, which subsequently reacts with the metal ions to form the SBU and MOF. The decomposition of DMF and crystallisation of the MOF depends on concentrations and temperature and has to be adjusted for every MOF synthesis.[60], [67]

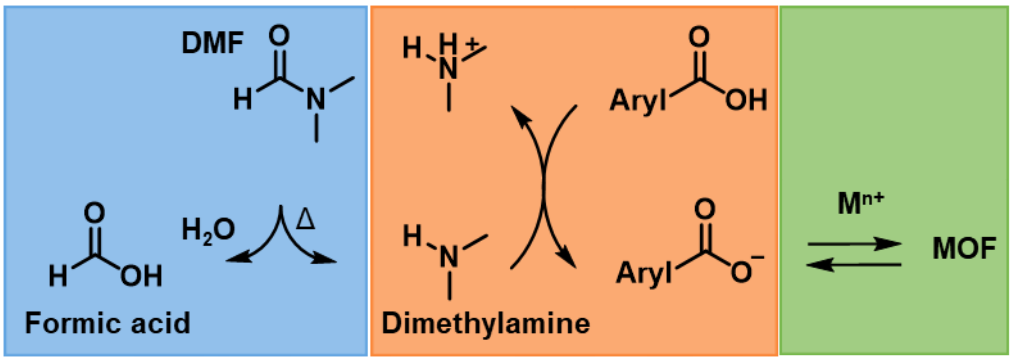

Figure 12. MOF crystallisation *via* solvothermal synthesis. Adapted and modified from [67].

An alternative method is electrodeposition of MOF layers on conductive substrates. Anodic electrodeposition would require the anode to be the metal-ion source.[67] Since this work focuses on graphite as substrate, only cathodic electrodeposition is applicable, where linker and metal-ions are present in the reaction solution. Hereby, the presence of water and especially nitrate have proven to be essential for ligand deprotonation and hence electrodeposition.[68] The cathode provides electrons for the reduction of nitrate ions. The resulting nitrite ions are able to reduce water in the solution, which generates hydroxide ions. Those hydroxide ions deprotonate the carboxylic ligand. Since metal-ions in solution are

attracted to the substrate by the negative potential, the MOF can subsequently deposit on the surface of the substrate (Figure 13).[67], [69]

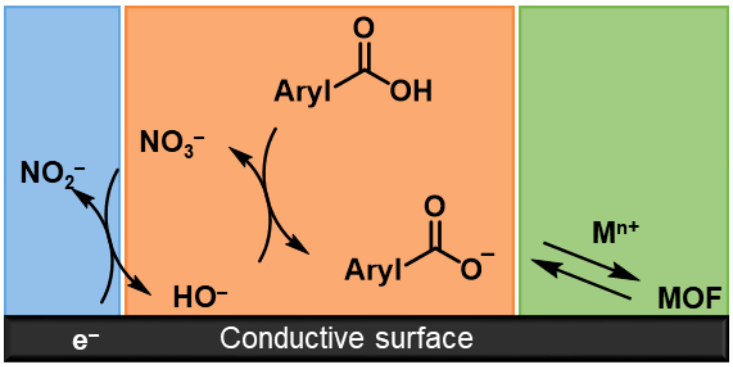

Figure 13. MOF crystallisation *via* cathodic electrodeposition. Adapted and modified from [67].

Due to their easy tuneable composition and porosity and the possibility of post-functionalisation, MOFs offer a large variety of applications. These include gas storage, catalysis, sensors and drug delivery.[70]–[73] Another advantageous feature of MOFs is their suitability to prepare porous carbon materials. Tailored porous carbon structures can be achieved and the flexibility in ligand design also allows *in situ* heteroatom doping.[74]

MOFs offer many possibilities to combine different metals and linkers. MOFs with carboxylic linkers could coordinate to the native surface oxygen groups of graphite for surface modification with MOFs.

3. Scope of this thesis

The rising demands on energy storage systems require continuous research and development. Even though graphite has proven to be the negative electrode material of choice in most LIBs since 1991, there are still drawbacks to overcome. This includes lithium-ion loss and capacity fading due to poor SEI formation. Some thermal and chemical treatments of graphite to face this challenge were shown in Chapter 2.2. However, the control over the surface composition is not ideal in these attempts. This thesis contributes to a deeper understanding of how different material classes and their attachment to graphite surfaces influences the behaviour of graphite electrodes in LIBs. With aryl diazonium salts (ADS), pyrenes and metal-organic frameworks (MOFs), three promising material classes for surface modification were introduced in Chapter 2.2, which will be investigated in the following chapters concerning their influence on and suitability to improve the electrochemical behaviour of graphite electrodes in LIBs. The relevant state-of-the-art literature is discussed in the following and is partly extracted from the scientific publication [75] and the submitted manuscript [76].

Chapter 5 focuses on the modification of graphite with ADS. The grafting of ADS to a variety of surfaces, including carbon-based materials has been extensively studied.[77]–[83] Leroux and Hapiot[84] reported that the grafting density of electrografted ethynyl diazonium salts on glassy carbon can be tuned by varying the size of the protecting group. Further, they found that a trimethylsilyl (TMS) protecting group is already bulky enough to prevent multilayer formation. Grafting of ADS has already been used to modify graphite electrodes in LIBs. In a previous work, Moock *et al.*[85] successfully electrografted and deprotected a TMS protected ethynyl ADS on a graphite electrode. They achieved enhanced capacity and cycling stability compared to a graphite-based reference system. Pan *et al.*[86] accomplished enhanced capacity and cycling stability for graphite electrodes in LIBs by grafting a nitro ADS to graphite powder. In another study by Verma and Novák[49], different grafting methods of a carboxy ADS were investigated. They found that aqueous *in situ* grafting leads to thinner surface layers compared to electrografting, which are advantageous to retain capacity and cycling stability in the battery. This study demonstrates that the grafting method must be considered to evaluate the influence of functional groups on the performance of the cell.

Although these findings have demonstrated successful modifications of graphite electrodes with ADS and partly enhanced the electrochemical performance in LIBs, the results must be adapted to application-oriented electrode systems in terms of the electrode composition. Comparing the impact of grafting methods and functional groups of ADS with the literature is difficult since different graphitic materials and binders were used in various cell types and setups. In the state-of-the-art literature, the electrodes consisted of 90 % w/w graphite as active material and 10 % w/w binder. Commercial electrodes additionally contain a conductive

carbon additive (usually <10 % w/w[87]) to achieve better particle-particle contact and guarantee sufficient electron conductive pathways in the electrode.[88]–[90] For example, Moock *et al*.[85] presented an electrode which lost 44 % of its initial capacity after only ten cycles at C/20, but commercial graphite electrodes can withstand more than 1000 cycles. Adding conductive additive could already lead to improved capacity and cycling stability of the used graphite electrodes. The influence of ADS modifications on realistic graphite electrode compositions remains to be evaluated. Furthermore, Pan *et al.*[86] and Verma and Novák[49] used a two-electrode graphite/lithium metal setup for electrochemical cycling. A three-electrode setup is more precise as the processes on the Li-metal are excluded and will not superimpose the effects originating from the grafted surface groups. Besides electrode composition and cell setup, the charge/discharge current densities for electrochemical measurements varies from C/20 to C/10. The performance at higher current densities has not been investigated at all.

However, Moock *et al.*[85], Pan *et al.*[86] and Verma and Novák[49] provide useful information about the relation of diazonium phenyl grafted graphite and their electrochemical performance in LIBs in their particular experiments. What these works do not reveal, is whether these findings are applicable to a uniform experimental setup and still show the same effects. For example, do hydrophilic groups perform better than hydrophobic? Is the choice of the grafting method crucial for groups other than carboxy as well? Or are reduced functional groups advantageous in general? In order to provide comparable values to these questions, electro- and *in situ* grafting of ethynyl (hydrophobic, reducible), amino (hydrophilic, not reducible), carboxy (hydrophilic reducible) and nitro groups (hydroneutral, reducible) were investigated to better understand the effects of grafted ADS on the electrochemical performance of graphite electrodes for LIBs. Ethynyl groups are protected with an alkyl silyl protecting group for the grafting step. To determine whether the distance between deprotected ethynyl groups is of importance, two different sized alkyl silyl protecting groups are under study for electrografting experiments.

Sinitskii *et al.*[91] reported a decrease in the conductivity of graphene nanoribbons (GNR) after grafting with ADS. This effect intensified when the grafting time was prolonged. The formation of new bonds with the aryls from the ADS causes a change in the hybridisation of the involved carbon atoms of the GNR from sp^2 to sp^3. The decrease of the conductivity is therefore attributed to the resulting disruption of the aromatic system of the GNR.[91] A reduction in the conductivity of graphite electrodes is not desirable. Thus, after looking at the covalent surface modification of graphite with ADS, Chapter 6 gives insight into a non-covalent alternative. Pyrenes are a prominent example for non-covalent carbon surface modification, since they allow strong π-π interactions with sp^2-hybridised carbons due to their aromatic character.[92] Complete preservation of the substrate's aromatic system and simple modification procedures

are reasons to choose pyrenes for surface modification. Various synthesis procedures have been described to attach diverse functional groups to the pyrene structure, but several functionalised pyrenes can be purchased commercially as well. The non-covalent attachment of pyrenes to carbon surfaces has already led to great success concerning the dispersion of nanotubes[93]–[95] and conductivity tuning of graphene[95], [96]. The use of pyrenes as electrolyte additive[97], stabiliser of carbon nanotubes components[98] or part of polymeric active materials[99]–[101] in energy storage systems has also been reported.

In this chapter, the focus is on the adsorption of pyrenes containing carboxy and amino moieties on graphite. The resulting powders were used to prepare functionalised graphite electrodes for LIBs. The surface morphology was studied by scanning electron microscopy (SEM) and the electrochemical cycling performance at low (C/10) and high (1C) current density tested in a three-electrode setup.

It is well-known that reducible surface groups can act as nucleation sites for the formation of the solid-electrolyte interphase (SEI).[38], [102] Therefore, it is expected that reducible carboxy groups in 1-pyrenecarboxylic acid show improved electrochemical behaviour compared to non-reducible amino groups in 1-aminopyrene. In contrast to aryl diazonium modification, the pyrene functional groups are orientated in parallel to the graphite surface. Additionally, 1-pyrenebutyric acid and 1-pyrenebutylamine were evaluated, where the functional groups are able to orientate either parallel to the basal plane or the edge site. It is expected that the functional groups in 1-pyrenebutyric acid and 1-pyrenebutylamine are easier accessible as nucleation sites for SEI formation compared to 1-pyrenecarboxylic acid and 1-aminopyrene. Hence, the electrochemical performance of butyl-containing pyrenes is expected to be superior to 1-pyrenecarboxylic and 1-aminopyrene. Pristine pyrene was used as well to distinguish the influence of the pyrene structure from the influence of the functional groups.

The orientation of the functional groups of 1-pyrenebutyric acid and 1-pyrenebutylamine on graphite does not only differ from 1-pyrenecarboxylic acid and 1-aminopyrene, but also from the corresponding carboxy and amino ADS derived aryls on graphite. The covalent grafting of ADS leads to a perpendicular orientation of the functional groups to the graphite surface. Even though the functional groups (carboxy and amino) are the same, the attachment and structure of the anchor molecule and the orientation of the functional group are different. Therefore, differences in the electrochemical behaviour are possible.

In Chapter 7 the previous use of small anchor molecules with one functional group is extended to surface modification with structural networks of MOFs. Research on MOFs and their derived materials for LIBs is broadly discussed in the literature and the growing interest for this material class for batteries is reflected in numerous recent review articles.[103]–[108]

MOFs enable a large variety of metal-ion centres. In this chapter, Zn was chosen as metal-ion centre, since ZnO has been extensively studied as negative electrode material in LIBs, due to

its high theoretical capacity (978 mAh g^{-1}), easy synthesis and chemical stability.[109], [110] Zn-based MOFs have been studied as negative electrode materials for LIBs as well.[111] The capacities derive from alloying reactions with the metal-ions, but also from interactions with the organic ligands (carboxy, benzene, amino, crown ether moieties). Capacities between ~140 mAh g^{-1} and ~380 mAh g^{-1} were achieved without a storage contribution from the metal centres.[112]–[114] Alloying mechanisms can provide reversible capacities of 105–560 mAh g^{-1} for 50 cycles[115], [116] Irrespective of the underlying mechanism, some MOFs are able to maintain their structure during electrochemical cycling,[112], [114], [116] while others do not.[113], [115] However, there is a high initial capacity loss in all cases, resulting in rather low first cycle efficiencies.[112]–[116] Even though, after further cycling some are able to reach Coulombic efficiencies of > 97 %,[112], [116] this is not achieved in every case.[114]

Not only MOFs itself but also MOF-derived materials have been investigated for LIBs.[103], [104], [111] For instance, metal oxides such as ZnO deliver high capacities due to their conversion- and alloying-type lithium-ion storage mechanism. However, large volume expansion, capacity fading and pulverisation over cycling are still a problem.[117] State-of-the-art literature reports carbonisation of Zn-containing MOFs to yield ZnO in a carbon matrix delivers higher capacities compared to commercial ZnO. No matter which exact MOF structure was used, the improved electrochemical performance is attributed to enhanced electronic conductivity and volume buffering due to hollow ZnO structures and the resulting carbon matrix. Nevertheless, the initial capacity loss is huge due to irreversible side reactions with the electrolyte.[118], [119] Additionally, the amount of inactive materials (conductive carbon and binder) is around 40 % w/w,[118], [119] which reduces the specific capacity and energy density of the electrode.

However, the approach in this work is to use MOFs as modification for graphite electrodes. There are some studies, where MOFs were synthesised as composites together with carbonaceous materials, such as carbon nanotubes (CNT)[120], [121] and graphene[122]. Recently, there have been some reports about MOFs as surface coating on active materials for LIBs.[123], [124] Cai *et al.*[123] *e.g.* synthesised a Cobalt-MOF modified graphite as negative electrode for LIBs and achieved a higher cycling stability for the modified graphite (with 15 % w/w MOF components and 85 % w/w graphite, with respect to the synthesis procedure, the MOF contained a carboxylate-based linker) compared with the pristine graphite. Han *et al.*[124] improved the capacity and cycling stability of a silicon negative electrode for LIBs using several MOFs, including carboxylate-containing MOFs. They outlined that the MOF coating can hold more electrolyte due to the large pore volume and high surface area of the MOF, which facilitates the lithium-ion transport.[124] These reports demonstrate the suitability of carboxylate-based MOFs for surface modification of active materials in LIBs.

Therefore, in cooperation with the group of Prof. Dr. Wolfgang Schmitt (Trinity College, Dublin), the modification of graphite with Zn-based MOFs featuring carboxylic linkers was investigated.

Specifically, the linkers 4,4’,4’’-(benzene-1,3,5-triyltris(ethyne-2,1-diyl)tribenzoic acid (BTEB) and 4,4',4''-(((1,3,5-triazine-2,4,6-triyl)tris(benzene-4,1-diyl))tris(ethyne-2,1-diyl))tribenzoic acid (TAP) were used. BTEB and TAP feature bigger ligand structures compared to the ones used in [123] and [124], which could enable even higher porosity and surface areas of resulting MOFs. In addition, the MOFs may even deliver additional capacity. The modification of graphite *via* electrodeposition and solvothermal synthesis is explored and the electrochemical behaviour of corresponding electrodes as negative electrodes in LIBs are studied. In addition, the graphite powders were carbonised after solvothermal synthesis and their behaviour as negative electrodes was investigated as well.

4. Experimental

4.1 Materials

Chemicals for synthesis and surface modifications were purchased from Sigma Aldrich and VWR and were used without further purification.

Mechano-cap 1P1 graphite was purchased from H. C. Carbon, Carbon black C-NERGY C65 from Imerys Graphite & Carbon, polyvinylidene fluoride (PVdF) from Merck, lithium metal chips from Gelon Energy Corp and battery electrolyte 1 M $LiPF_6$ in ethylene carbonate (EC):dimethyl carbonate (DMC) 50:50 % v/v from Sigma Aldrich.

4.2 Synthesis

General procedure for the synthesis of aniline derivatives[84]

4-Iodoaniline (1 eq.) was dissolved in a 4:1 mixture of tetrahydrofuran (THF) and diisopropylamine (DIPA) in a schlenk flask. After adding the corresponding trialkylsilylacetylene (1.1 eq.) the solution was degassed with argon for 30 min. Consequently, bis(triphenylphosphine)palladium(II)dichloride (0.05 eq.) and after 5 min copper(I)iodide (0.05 eq.) were added and the solution was stirred overnight under argon at room temperature. After filtering and washing with hexane the reaction mixture was washed with saturated ammonium chloride, saturated sodium chloride and water. The combined organic phase was dried with magnesium sulfate and further purified by column chromatography in dichloromethane (DCM) and hexane 1:1.

Synthesis of 4-((Triisopropyl)ethynyl)aniline (**1**)

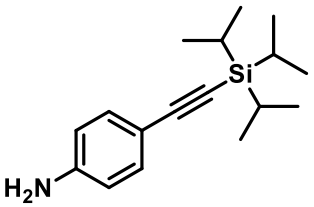

4-Iodoaniline (1.00 g, 4.57 mmol, 1 eq), triisopropylsilylacetylene (1.13 ml, 5.02 mmol, 1.1 eq.), bis(triphenylphosphine)-palladium(II)dichloride (160.24 mg, 0.23 mmol, 0.05 eq.) and copper(I)iodide (43.48 mg, 0.23 mmol, 0.05 eq.) in THF:DIPA (80 ml:20 ml) were used according to the general procedure. The reaction gave 0.80 g (2.94 mmol, 64 %) of **1** as a brownish oil.

^{1}H-NMR ($CDCl_3$, δ in ppm): 1.11 (m, 21H, C_9H_{21}), 3.78 (s, 2H, NH_2), 6.58 (d, 2H, C_6H_4), 7.28 (d, 2H, C_6H_4). ^{13}C-NMR ($CDCl_3$, δ in ppm): 11.5 (CH), 18.85 (CH_3), 87.64 (C≡C), 108.01 (C≡C), 113.30 ($C_{aromatic}$), 114.69 ($CH_{aromatic}$), 133.55 ($CH_{aromatic}$), 146.73 ($C_{aromatic}$). IR (ATR, $\tilde{\nu}$ in cm^{-1}): 3482 (m), 3386 (m), 3209 (w), 3040 (w), 2956 (m), 2939 (s), 2890 (m), 2861 (s), 2139 (s), 1886 (w), 1617 (s), 1600 (m), 1512 (s), 1460 (m), 1382 (w), 1364 (w), 1294 (s), 1251 (w), 1230(w), 1179 (m), 1129 (w), 1074 (m), 1014 (m), 993 (m), 917 (w), 878 (m), 847 (m), 827 (m), 787 (m), 677 (m), 652 (m), 594 (m), 535 (m), 487 (m).

General Procedure for the Synthesis of Aryldiazonium Tetrafluoroborates (on basis of [125])
The corresponding aniline derivative (1 eq.) was dissolved in acetone before tetrafluoroboronic acid (50 %, 3 eq.) was added dropwise to the solution. After cooling the mixture in an ice bath for 30 min sodium nitrite (1.1 eq.) was added and the mixture was stirred overnight at room temperature. Cold deionised water or ether was used to precipitate the product which was then filtered and washed with cold deionised water before it was dried under vacuum overnight.

Synthesis of 4-((Trimethylsilyl)ethynyl)benzenediazonium tetrafluoroborate (**2**)

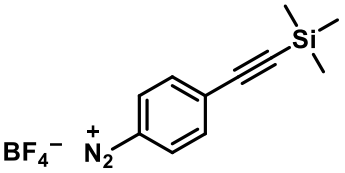

4-((Trimethylsilyl)ethynyl)aniline (189,33 mg, 1.00 mmol, 1 eq.) dissolved in 3 ml acetone, tetrafluoroboronic acid (50 %, 0.38 ml, 3 eq.) in 7.5 ml acetone, sodium nitrite (75.89 mg, 1.10 mmol, 3 eq.) and water gave 250 mg (0,87 mmol, 87 %) of **2** as a yellow solid.

^{1}H-NMR (DMSO-d6, δ in ppm): 0.29 (s, 9H, CH_3), 8.02 (d, 2H, C_6H_4), 8.65 (s, 2H, C_6H_4). ^{13}C-NMR (DMSO-d6, δ in ppm): 0.63 (CH_3), 102.20 (C≡C), 106.43 (C≡C), 115.20 ($C_{aromatic}$), 132.98 ($CH_{aromatic}$), 133.71 ($CH_{aromatic}$), 133.79 ($C_{aromatic}$). IR (ATR, $\tilde{\nu}$ in cm^{-1}): 3373 (w), 3112 (w), 2960 (w), 2652 (w), 2600 (w), 2287 (s), 2117 (w), 1794 (w), 1668 (w), 1580 (s), 1473 (w), 1412 (m), 1311(m), 1288 (m), 1252 (m), 1230 (m), 1182 (m), 1124(m), 1099 (m), 1036 (s), 975 (m), 842 (s), 763 (m), 704 (m), 627 (m), 536 (s), 523 (m), 489 (m).

Synthesis of 4-((Triisopropylsilyl)ethynyl)benzenediazonium tetrafluoroborate (**3**)

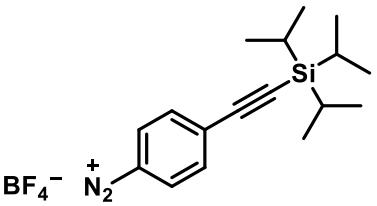

1 (0.28 g, 1.00 mmol, 1 eq.) dissolved in 3 ml acetone, tetrafluoroboronic acid (50 %, 0.38 ml, 3 eq.) in 7.5 ml acetone, sodium nitrite (75.89 mg, 1.10 mmol, 1.1 eq.) and water gave 344 mg (0,92 mmol, 92 %) of **3** as a redish solid.

^{1}H-NMR (DMSO-d6, δ in ppm): 1.12 (m, 21H, C_9H_{21}), 8.04 (d, 2H, C_6H_4), 8.66 (d, 2H, C_6H_4). ^{13}C-NMR (DMSO-d6, δ in ppm): 10.56 (CH), 18.41 (CH_3), 102.90 (C≡C), 104.40 (C≡C), 115.09 ($C_{aromatic}$), 133.10 ($CH_{aromatic}$), 133.71 ($CH_{aromatic}$), 133.93 ($C_{aromatic}$). IR (ATR, $\tilde{\nu}$ in cm^{-1}): 3373 (w), 3110 (m), 2954 (s), 2887 (m), 2864 (s), 2285 (s), 1780 (w), 1767 (w), 1578 (s), 1462 (s), 1411 (m), 1382 (m), 1288 (s), 1226 (s), 1188 (s), 1120 (s), 1064 (s), 1027 (s), 993 (s), 918 (m), 883 (m), 848 (s), 831 (s), 789 (m), 770 (m), 723 (s), 677 (s), 665 (s), 654 (s), 592 (s), 570 (s), 552 (m), 536 (s), 521 (s), 496 (s), 473 (s), 455 (s), 405 (m).

Synthesis of 4-Carboxybenzenediazonium tetrafluoroborate (**4**)

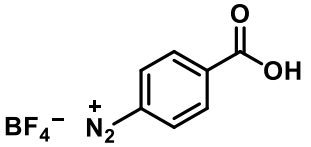

4-Aminobenzoic acid (137.14 g, 1.00 mmol, 1 eq.) dissolved in 3 ml acetone, tetrafluoroboronic acid (50 %, 0.38 ml, 3 eq.) in 7.5 ml acetone, sodium nitrite (75.89 mg, 1.10 mmol, 1.1 eq.) and ether gave 166 mg (0,71 mmol, 71 %) of **4** as a white solid.

^{1}H-NMR (DMSO-d6, δ in ppm): 8.33 (d, 2H, C_6H_4), 8.69 (d, 2H, C_6H_4). ^{13}C-NMR (DMSO-d6, δ in ppm): 119.80 ($CH_{aromatic}$), 131.32 ($CH_{aromatic}$), 131.51 ($CH_{aromatic}$), 133.10 ($CH_{aromatic}$), 164.80 (COOH). IR (ATR, $\tilde{\nu}$ in cm^{-1}): 3286 (w), 3105 (w) 2972 (w), 2295 (w), 2163 (w), 1983 (), 1782 (w), 1770 (w), 1730 (m), 1458 (w), 1417 (w), 1387 (w), 1298 (s), 1219 (m), 1032 (s), 870 (m), 764 (s), 708 (s), 707 (s), 550 (s), 527 (s), 519 (), 494 (s), 480 (s), 467 (s), 449 (w), 434 (w).

Synthesis of 4-Aminobenzendiazonium tetrafluoroborate (**5**)

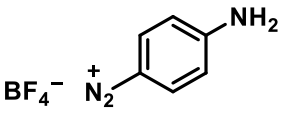

p-Phenylenediamine (18.14 mg, 1.00 mmol, 1 eq.) dissolved in 3 ml acetone, tetrafluoroboronic acid (50 %, 0.38 ml, 3 eq.) in 7.5 ml acetone, sodium nitrite (75.89 mg, 1.10 mmol, 1.1 eq.) and ether gave 141 mg (0.68 mmol, 68 %) of **5** as a brown solid.

^{1}H-NMR (DMSO-d6, δ in ppm): 6.81 (d, 2H, C_6H_4), 8.14 (d, 2H, C_6H_4), 8.32 (s, 1H, NH_2). ^{13}C-NMR (DMSO-d6, δ in ppm): 89.04 ($CH_{aromatic}$), 115.32 ($CH_{aromatic}$), 135.26 ($CH_{aromatic}$), 159.17 ($CH_{aromatic}$). IR (ATR, $\tilde{\nu}$ in cm^{-1}): 3458 (s), 3367 (s), 3259 (m), 3105 (w), 2744 (w), 2688 (w), 2183 (s), 1783 (w), 1768 (w), 1645 (s), 1587 (s), 1554 (s), 1504 (m), 1483 (m) 1367 (s), 1292 (m), 1128 (s), 1010 (s), 970 (s), 831 (s), 765 (m), 700 (m), 642 (w), 569 (m), 538 (s), 503 (s), 474 (s), 409 (s).

Synthesis of 4-Nitrobenzendiazonium tetrafluoroborate (**6**)

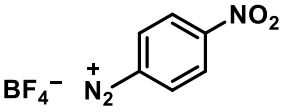

4-Nitroaniline (138.13 mg, 1.00 mmol, 1 eq.) dissolved in 3 ml acetone, tetrafluoroboronic acid (48 %, 0.38 ml, 3 eq.) in 7.5 ml acetone, sodium nitrite (75.89 mg, 1.10 mmol, 1.1 eq.) and water gave 196 mg (0.83 mmol, 83 %) of **6** as a brownish solid.

^{1}H-NMR (DMSO-d6, δ in ppm): 8.72 (d, 2H, C_6H_4), 8.93 (d, 2H, C_6H_4). ^{13}C-NMR (DMSO-d6, δ in ppm): 121.89 ($CH_{aromatic}$), 126.02 ($CH_{aromatic}$), 134.48 ($CH_{aromatic}$), 153.19 ($CH_{aromatic}$). IR (ATR, $\tilde{\nu}$ in cm^{-1}): 3382 (w), 3117 (m), 3107 (m), 3070 (w), 3024 (w), 2891 (w), 2306 (s), 1778 (w), 1770 (w), 1612 (m), 1575 (m), 1537 (s), 1467 (w), 1421 (w), 1353 (s), 1315 (s), 1297 (s), 1120 (s), 1039 (s), 1006 (s), 865 (s), 856 (s), 829 (m), 810 (m), 754 (s), 742 (s), 661 (s), 634 (m), 565 (m), 547 (m), 524 (s).

Synthesis of 2,4,6-Tris(4-bromophenyl)-1,3,5-triazine (**7**)

To a stirred solution of dimethylamine (2 M in THF, 4.64 ml, 9.28 mmol, 1.1 eq.) in dry Et_2O (120 ml), *n*-BuLi (1.6 M in hexane, 5.8 ml, 9.28 mmol, 1.1 eq.) was added dropwise under N_2-atmosphere. After 30 min 4-bromo-benzonitrile (1.54 g, 8.44 mmol, 1 eq.) was added and after a further 1 h more 4-bromo-benzonitrile (3.07g, 16.88 mmol, 2 eq.) was added. The solution was stirred for 24 h under N_2 and another 1 h in air before the precipitate was filtered and washed with Et_2O.

Yield: 4.16 g, 82 %. ^{1}H-NMR ($CDCl_3$, δ in ppm): 7.71 (d, 6H, CH), 8.61 (d, 6H, CH). ^{13}C-NMR ($CDCl_3$, δ in ppm): 128.00 (C), 130.65 (CH), 132.18 (CH), 134.95 (C), 171.27 (C). IR (ATR, $\tilde{\nu}$

in cm^{-1}): 1591 (w), 1580 (s), 1543(m), 1511 (s), 1486 (s), 1401 (s), 1370 (s), 1355 (s), 1292 (w), 1280 (w), 1237 (w), 1208 (w), 1173 (m), 1102 (w), 1092 (w), 1067 (m), 1010 (s), 970 (w), 936 (w), 860 (m), 843 (s), 829 (w), 804 (s), 740 (w), 706 (w), 629 (w), 600 (w), 511 (m), 495 (s), 476 (s), 418 (m).

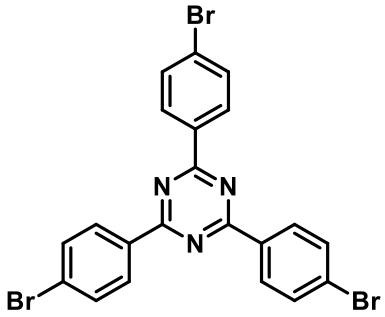

Synthesis of 2,4,6-Tris(4-((Trimethylsilyl)ethynyl)phenyl)-1,3,5-triazine (**8**)

Compound **7** (3.55 g, 6.50 mmol, 1 eq.), Pd(II)(PPh_3) (0.53 g, 0.75 mmol, 6 mol%), and Cu(I)I (0.0475 g, 0.25 mmol, 2 mol%) in DIPA (80 ml) were stirred for 5 min under Ar-atmosphere. Trimethylsilyl acetylene (3.60 ml, 25.9 mmol, 4.1 eq.) was added and the reaction mixture refluxed for 48 h. The product was purified by column chromatography in DCM and washed with Et_2O.

Yield: 2.71 g, 70 %. ^{1}H-NMR ($CDCl_3$, δ in ppm): 0.30 (s, 27H, CH_3), 7.65 (d, 6H, CH), 8.68 (d, 6H, CH). ^{13}C-NMR ($CDCl_3$, δ in ppm): 0.07 (CH_3), 97.67 (C≡C), 104.80 (C≡C), 127.56 (C), 128.89 (CH), 132.37 (CH), 135.91 (C), 171.19 (C).). IR (ATR, $\tilde{\nu}$ in cm^{-1}): 2959 (m), 2926 (w), 2901 (w), 2855(w), 2157 (m), 1603 (w), 1572 (s), 1507 (s), 1437 (w), 1406 (m), 1370 (s), 1359 (s), 1297 (w), 1248 (s), 1219 (m), 1176 (m), 1147 (m), 1094 (m), 1017 (s), 862 (s), 839 (s), 812 (s), 799 (s), 758 (s), 696 (m), 652 (s), 641 (m), 608 (m), 542 (s), 500 (m), 545 (m), 442 (w).

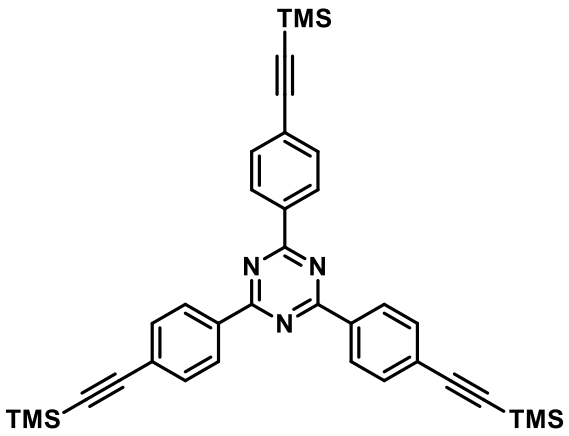

Synthesis of 2,4,6-Tris(4-ethynylphenyl)-1,3,5-triazine (**9**)

To a stirred solution of compound **8** (2.69 g, 4.50 mmol, 1 eq.) in DCM (200 ml), K_2CO_3 (1.80 g, 13.05 mmol) in CH_3OH (30 ml) was added and stirred at room temperature for 3 h. The reaction mixture was washed with water and brine and the organic phases combined before the solvents were removed under reduced pressure. The product was recrystallised from DCM:THF (3:1).

Yield: 1.47 g, 86 %. ^{1}H-NMR ($CDCl_3$, δ in ppm): 3.28 (s, 3H, CH), 7.69 (d, 6H, CH), 8.72 (d, 6H, CH). ^{13}C-NMR ($CDCl_3$, δ in ppm): 80.10 (C≡C), 83.45 (C≡C), 126.58 (C), 128.98 (CH), 132.59 (CH), 136.27 (C), 171.25 (C). IR (ATR, $\tilde{\nu}$ in cm^{-1}): 3291 (w), 3239 (w), 2924 (w), 2853 (w), 2160 (w), 1712 (m), 1607 (s), 1574 (s), 1506 (s), 1435 (m), 1408 (s), 1358 (s), 1267 (s), 1176 (s), 1146 (m), 1104 (s), 1016 (s), 969 (m), 868 (m), 851 (m), 814 (s), 768 (s), 749 (s), 643 (s), 645 (s), 610 (m), 539 (s), 529 (s).

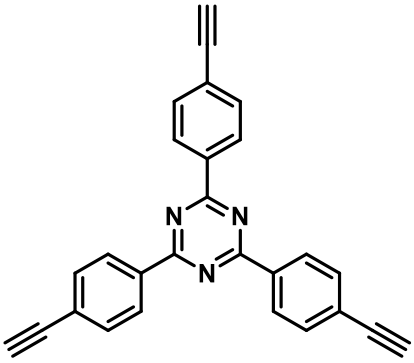

Synthesis of Trimethyl-4,4',4''-(((1,3,5-triazine-2,4,6-triyl)tris(benzene-4,1-diyl))tris(ethyne-2,1-diyl))tribenzoate (**10**)

Compound **9** (1.34 g, 3.50 mmol, 1.0 eq.), Pd(II)(PPh_3) (0.14 g, 0.21 mmol, 6 mol%), Cu(I)I (0.013 g, 0.07 mmol, 2 mol%) and methyl 4-iodobenzoate (3.58 g, 13.65 mmol, 3.9 eq.) in DIPA:THF (100 ml:30 ml) were refluxed for 48 under Ar-atmosphere. The product was purified by column chromatography in DCM and recrystallization from with DCM/CH3Cl).

Yield: 1.82 g, 66 %. ^{1}H-NMR ($CDCl_3$, δ in ppm): 3.95 (s, 3H, CH), 7.66 (d, 6H, CH), 7.75 (d, 6H, CH), 8.06 (d, 6H, CH), 8.79 (d, 6H, CH). ^{13}C-NMR ($CDCl_3$, δ in ppm): 52.45 (CH_3), 91.59 (C≡C), 92.14 (C≡C), 127.23 (C), 127.71 (C), 129.13 (CH), 129.76 (CH), 130.04 (C), 131.83 (CH), 132.18 (CH), 136.16 (C), 166.66 (COO), 171.25 (C).). IR (ATR, $\tilde{\nu}$ in cm^{-1}): 2950 (w), 2845 (w), 2569 (w), 2211 (w), 2161 (w), 2030 (w), 1717 (s), 1606 (s), 1570 (s), 1504 (s), 1435 (s), 1405 (s), 1361 (s), 1307 (m), 1268 (s), 1192 (m), 1174 (s), 1151 (m), 1102 (s), 1015 (s), 964 (m), 855 (s), 837 (m), 811 (s), 766 (s), 714 (m), 693 (s), 640 (m), 609 (m), 544 (m), 520 (s), 441 (m).

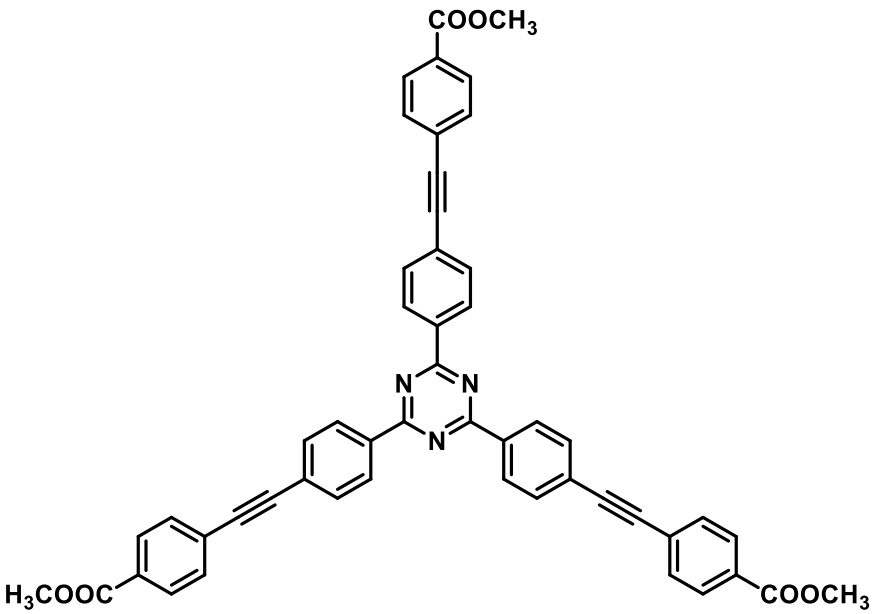

Synthesis of 4,4',4''-(((1,3,5-Triazine-2,4,6-triyl)tris(benzene-4,1-diyl))tris(ethyne-2,1-diyl))tribenzoic acid (**11**)

To a stirred solution of compound **10** (1.57 g, 2.00 mmol) in THF (40 ml) and CH_3OH (40 ml), KOH (20 ml, 5 M in water, 5.8 mmol, 2.9 eq.) was added and the reaction mixture was stirred under reflux overnight. The organic solvents were removed and hydrochloric acid (5 M) was added dropwise until pH 3 was reached to precipitate the product.

Yield: 1.28 g, 86 %. ^{1}H-NMR ($CDCl_3$, δ in ppm): 7.66 (d, 6H, CH), 7.73 (d, 6H, CH), 7.94 (d, 6H, CH), 8.59 (d, 6H, CH), 13.15 (s, 3H, COOH). ^{13}C-NMR ($CDCl_3$, δ in ppm): 91.39 (C≡C), 91.50 (C≡C), 126.13 (C), 126.24 (C), 128.75 (CH), 129.51 (CH), 130.84 (C), 131.65 (CH), 131.96 (CH), 135.22 (C), 166.59 (COO), 170.09 (C). IR (ATR, $\tilde{\nu}$ in cm^{-1}): 3073 (w), 2972 (w), 2657 (w), 2528 (w), 2211 (w), 1929 (w), 1781 (w), 1768 (w), 1688 (s), 1605 (s), 1569 (s), 1505 (s), 1405 (s), 1360 (s), 1291 (s), 1226 (m), 1174 (s), 1151 (m), 1092 (m), 1015 (m), 927 (w), 855 (m), 835 (w), 811 (s), 766 (s), 692 (m), 640 (w), 601 (m), 540 (m), 513 (m).

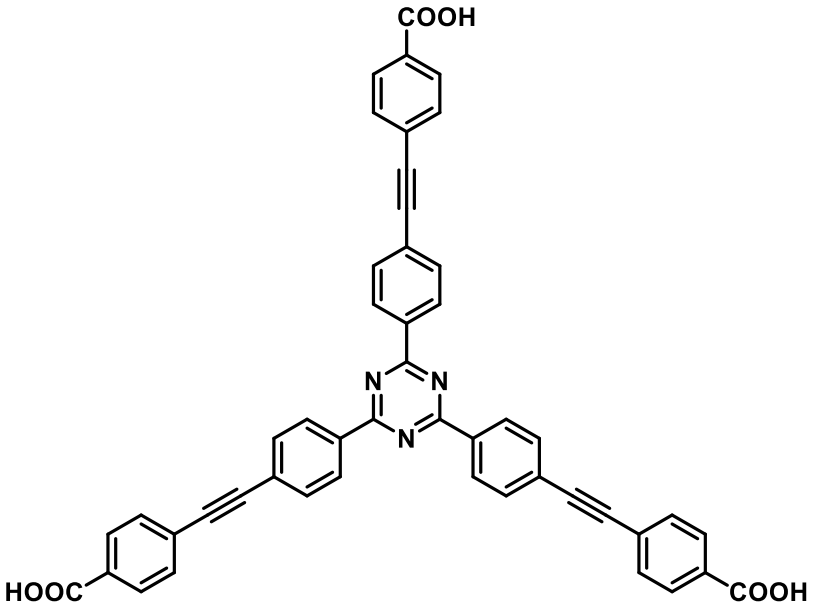

4.3 Electrode preparation

Graphite (90 % w/w) and conductive additive C65 (3 % w/w) were ground prior to dry mixing at 1000 rpm in a speedmixer (DAC150.1 FVZ Hauschild). Dimethyl sulfoxide (DMSO) was added portion wise and the dispersion was mixed at different speeds between 1500 and 3000 rpm before polyvinylidene fluoride binder (7 % w/w) dissolved in DMSO was added. Mixing the dispersion for 10 min at 800 rpm gave a viscous paste that was subsequently coated on copper foil with a doctor blade (wet thickness 200 µm, dry thickness 120 µm ± 5 µm). The coating was dried at room temperature overnight, at 120 °C for 8 h and finally at 120 °C in vacuum overnight.

4.4 Surface modifications

4.4.1 Procedures for Chapter 5

Electrografting (on basis of [50] and [85])

All experiments were performed in an Ar-filled glovebox. Electrografting of aryl diazonium salts was performed in glass cells with rectangular cut pieces (approximately 15 x 35 mm) of pristine graphite electrodes as working electrode, a platinum mesh as counter electrode and $AgNO_3$/Ag (0.1 M) in acetonitrile as reference electrode. A solution of 0.1 M tetrabutylammonium tetrafluoroborate (TBATFB, $(NBu_4)BF_4$) in acetonitrile was used as electrolyte. To calibrate the reference electrode platinum was used as working and counter electrode in a 1 mM solution of ferrocene. Cyclic voltammetry was performed for 5 cycles between –0.4 V and 0.4 V *vs.* $AgNO_3$/Ag at a 20 mV/s scan rate.

General procedure for reductive electrografting of aryl diazonium salts

The corresponding aryl diazonium salt was dissolved in the electrolyte to receive a 0.01 M solution. A constant potential of –0.6 V *vs*. $AgNO_3$/Ag was applied for 1 h to graft the aryl diazonium salt onto the graphite surface. After the grafting process, the working electrode was immersed in acetonitrile for 10 min and rinsed with acetonitrile to wash away any residues.

General procedure for *in situ* grafting of aryl diazonium salts (on basis of [48])

8.3 mmol of the corresponding aniline, 8.3 mmol sodium nitrite and subsequently 10 ml of concentrated hydrochloric acid were added to a dispersion of 1 g graphite in 50 ml water. After stirring overnight, the dispersion was filtered and washed thoroughly with water and acetone. For the deprotection of 4-[(Trimethylsilyl)ethynyl]benzenediazonium tetrafluoroborate the grafted powder was stirred in a solution of 0.1 M tetrabutylammonium fluoride (TBAF (NBu_4)F) in THF for 30 min before the deprotected powder was filtered and washed with THF. All powders were dried under vacuum and used for electrode preparation as described in Chapter 4.3.

General procedure for deprotection of grafted alkylsilyl protected ethynyl aryl diazonium salts

To deprotect the alkyne moiety of aryl diazonium salts, electrografted electrodes were immersed in a 0.1 M solution of TBAF in THF for 30 min with occasional swaying of the solution. Subsequently, the deprotected electrodes were immersed in THF for 10 min and rinsed with THF afterwards to wash away any residues. *In situ* grafted graphite powders were stirred in a solution of 0.1 M TBAF in THF for 30 min before the deprotected powder was filtered and washed with THF.

4.4.2 Procedures for Chapter 6

General procedure for adsorption of pyrenes

1 g graphite was added to a 5 mM solution of the corresponding pyrene in 50 ml DMSO. After stirring overnight, the dispersion was filtered and washed thoroughly with DMSO. All powders were dried under vacuum and used for electrode preparation as described in Chapter 4.3.

Cyclic voltammetry of pyrene-modified graphite powders

The modified graphite powders were dropcasted on a glassy carbon electrode. The glassy carbon electrode was used as working electrode, a graphite rod electrode as counter electrode and AgCl/Ag as reference electrode. The cyclic voltammetry was performed in H_2SO_4 with a scan rate of 100 mV s^{-1}.

4.4.3 Procedures for Chapter 7

Electrodeposition of Zn-BTEB (on basis of [69])

Electrodeposition of Zn-BTEB was performed in glass cells with rectangular cut pieces (approximately 15 x 35 mm) of pristine graphite electrodes as working, a platinum wire as

counter and a Ag(cryptand)$^+$/Ag (0.1 M) in tetrabutylammonium hexafluorophosphate (TBAHFP, $(NBu_4)PF_6$) as reference electrode. A solution of deaired 0.1 M TBAHFP in dimethyl formamide (DMF) and water (100:1, 10 ml) was used as electrolyte. BTEB (48.67 mg, $9.53 \cdot 10^{-2}$ mmol) ($Zn(NO_3)_2 \cdot 6H_2O$ (47.00 mg, $1.58 \cdot 10^{-1}$ mmol) and sodium nitrate (20 mg, $2.35 \cdot 10^{-1}$ mmol) were added to the electrolyte and a constant potential of –1.4 V *vs.* Ag(cryptand)$^+$/Ag was applied for 10 min to achieve coatings of M-BTEB. After the deposition process, the working electrode was immersed in DMF for 10 min and rinsed with DMF to wash away any residues.

Synthesis of Zn-BTEB (based on [69])
BTEB (3.4 mg, $6.7 \cdot 10^{-3}$ mmol, 1 eq) and $Zn(NO_3)_2 \cdot 6H_2O$ (3.9 mg, $1.3 \cdot 10^{-2}$ mmol, 2 eq.) were dissolved in DMF (1 ml). The mixture was heated to 90 °C for 48 h, before the crystals were washed with DMF.

Synthesis of Zn-TAP (based on a procedure of O'Doherty (not published))
TAP (5.0 mg, $6.7 \cdot 10^{-3}$ mmol, 1 eq) and $Zn(NO_3)_2 \cdot 6H_2O$ (3.9 mg, $1.3 \cdot 10^{-2}$ mmol, 2 eq.) were dissolved in DMF (1 ml). The mixture was heated to 70 °C for 48 h, before the crystals were washed with DMF.

Synthesis of Zn-BTEB on graphite
Graphite (0.5 g) was added to a stirring solution of BTEB (34 mg, $6.7 \cdot 10^{-2}$ mmol, 1 eq) and $Zn(NO_3)_2 \cdot 6H_2O$ (39 mg, $1.3 \cdot 10^{-1}$ mmol, 2 eq.) in DMF (10 ml). The mixture was heated to 90 °C for 48 h, before the graphite powder was filtered off and washed with DMF.

Synthesis of Zn-TAP on graphite
Graphite (0.5 g) was added to a stirring solution of TAP (50 mg, $6.7 \cdot 10^{-2}$ mmol, 1 eq) and $Zn(NO_3)_2 \cdot 6H_2O$ (39 mg, $1.3 \cdot 10^{-1}$ mmol, 2 eq.) in DMF (10 ml). The mixture was heated to 70 °C for 48 h, before the graphite powder was filtered off and washed with DMF.

Carbonisation of Zn-BTEB on graphite and Zn-TAP on graphite
Graphite-Zn-BTEB and graphite-Zn-TAP powders were carbonised at 500 °C with a heating rate of 3 °C/min for 4 h under nitrogen. The carbonised powders were used to prepare graphite electrodes for electrochemical characterisation.

4.5 Material and electrode characterisation

4.5.1 Nuclear magnetic resonance spectroscopy

^1H and ^{13}C spectra were recorded on a Bruker Avance 400 NMR or a Bruker DPX 400 spectrometer operating at 400 MHz for ^1H-NMR and 100 MHz for ^{13}C-NMR. Chemical shifts δ are presented in parts per million (ppm) relative to the resonance signal at 7.26 ppm (^1H, $CDCl_3$) and 77.16 ppm (^{13}C, $CDCl_3$) or 2.50 ppm (^1H, DMSO-d6) and 39.52 ppm (^{13}C, DMSO-

d6). The spin multiplicity and corresponding signal patterns are abbreviated as follows: s = singlet, d = doublet, t = triplet, q = quartet and m = multiplet.

4.5.2 Infrared spectroscopy

Infrared spectra (IR) were recorded on a Bruker Alpha-p or PerkinElmer One instrument applying attenuated total reflection (ATR) technology in a frequency range of 4000 – 400 cm^{-1}. The signal intensities are abbreviated as follows: s = strong, m = medium, w = weak.

4.5.3 Scanning electron microscopy

Scanning electron microscopy (SEM) measurements were conducted by a thermal field emission scanning electron microscope (FESEM, Carl Zeiss SMT AG) at an acceleration voltage of 5 kV. The samples were fixed on a steel sample holder by using sticky tape.

4.5.4 Optical microscopy

Optical microscope images were recorded with a Leica M205 instrument.

4.5.5 X-ray photoelectron spectroscopy

X-ray photoemission measurements were performed using a K-alpha XPS spectrometer from Thermo Fisher Scientific (East Grinstead). The samples were illuminated with monochromatic Al-Kα X-rays with a spot size of about 400 µm. The photoelectrons were detected with a hemispherical 180 dual focus analyzer with 128 channel detectors. To prevent any localized charge buildup, the K-Alpha charge compensation system was employed during analysis, using electrons of 8 eV energy and low-energy argon ions. The Thermo Avantage software was used for data acquisition and processing.[126] The spectra were fitted with one or more Voigt profiles (binding energy uncertainty: ±0.2 eV). All spectra were referenced to the C 1s peak of hydrocarbon at 285.0 eV binding energy controlled by means of the well-known photoelectron peaks of metallic Cu, Ag, and Au.

4.5.6 X-ray diffraction

Structural characterization was carried out using the powder X-ray diffraction (PXRD) on a STOE Stadi P powder diffractometer with monochromatic Cu-$K\alpha_1$ radiation (λ = 1.54056 Å) in transmission geometry. The XRD measurements were performed at room temperature with a 0.015° 2θ step between 5 and 70 degrees of 2θ. The Kapton film's presence visibly adds amorphous-like background in the XRD patterns at 10° < 2θ < 17°.

4.6 Cell assembly

Electrochemical measurements were performed in three electrode setups in custom-built polyether ether ketone (PEEK) cells with spring loaded titanium pistons as described in [127]. Cell assembly was performed in a glovebox (MBraun, H_2O and O_2 content <0.1 ppm). Working electrodes were punched to 12 mm discs and were separated from the 12 mm lithium metal

counter electrode discs by a 13 mm glassfiber separator (GF/D, Whatman). Lithium metal was used as reference electrode. The cells were filled with 1 M $LiPF_6$ in a 50:50 % v/v mixture of ethylene carbonate (EC) and dimethyl carbonate (DMC) electrolyte (LP30, BASF).

4.7 Electrochemical measurements

Electrochemical characterisation was carried out in climate chambers at 25 °C using a VMP3 multi-channel potentiostat (Biologic). Galvanostatic cycling with potential limitation (GCPL) measurements were performed between 0.01 V and 1.80 V vs. Li^+/Li with C/10 for 5 cycles followed by 45 cycles with 1C. The presented data in all cycling stability and Coulombic efficiency *vs.* cycle number plots are average values of two electrodes of each sample including error bars.

5. Modification with aryl diazonium salts

Aryl diazonium salts are often used to modify carbon surfaces due to their easy synthesis and variety of possible modification methods, which lead to covalent bonds between the aryl and the carbon surface (see Chapter 2.2.1). In this Chapter, advantage is taken of the easy synthesis to produce aryl layers on graphite, which feature selected functional groups. The functional groups under study are (deprotected) ethynyl, amino, carboxy and nitro moieties (see Chapter 3). The surface composition and morphology of electro- and *in situ* grafted graphite electrodes were studied using X-ray photoelectron spectroscopy (XPS) and scanning electron microscopy (SEM). The electrochemical performance was evaluated using a three-electrode setup with realistic electrode composition. The influence of the grafting method and the corresponding influence of each functional group are addressed. Unlike in state-of-the-art literature, the uniform electrode preparation and cell setup in this work allows a direct comparison of effects of grafting method and functional groups on electrochemical properties. The Subchapters 5.1 – 5.4 are extracted from the scientific publication "Functionalisation of graphite electrodes with aryl diazonium salts for lithium-ion batteries".[75]

5.1 Electrografting of alkyl silyl protected ethynyl aryl diazonium salts

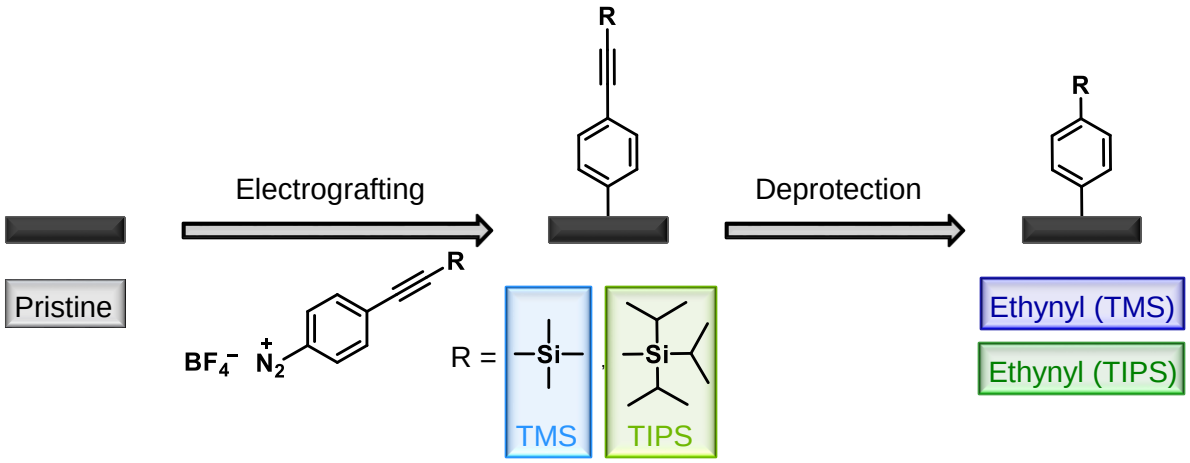

Scheme 1. Electrografting of alkyl silyl protected ethynyl aryl diazonium salts to graphite electrodes.

Graphite electrodes were used as substrates for electrografting experiments according to a method displayed in Scheme 1. The electrografted electrodes are referred to as TMS and TIPS, whereas the deprotected electrodes are labelled as ethynyl. To distinguish the ethynyl groups from each other, the protecting group from which they derived is added in brackets, giving ethynyl (TMS) and ethynyl (TIPS). Silicon in alkyl silyl protecting groups works as a marker to confirm successful electrografting *via* XPS (Figure 14a). The appearance of Si 2p

peaks at a binding energy of 100.5 eV (Si $2p_{3/2}$) in TMS and TIPS corresponding to silicon linked to carbon suggests that the electrografting of the protected ethynyl moiety was performed successfully.[85] The silicon content for TMS (3.2 at%) is higher than for TIPS (1.4 at%), which is attributed to the higher distance between the molecules caused by the more steric demanding TIPS group. As expected, Si 2p peaks in ethynyl (TMS) and ethynyl (TIPS) disappeared after the deprotection of the ethynyl moiety. The SEM images of the reference and all modified electrodes (Figure 14b) show conductive additive particles and a fibrous structure on the graphite surface of the pristine, TMS and TIPS samples, which is assigned to the PVdF binder.[128] However, in the images of ethynyl (TMS) and ethynyl (TIPS) additional spots are visible on the electrode surface, whereas ethynyl (TMS) shows visibly more spots than ethynyl (TIPS). The spots most probably evolve during the deprotection process. To investigate the electrochemical performance of ethynyl (TMS) and ethynyl (TIPS) compared to the pristine electrode, a three-electrode setup was used. The electrochemical cycling performance and Coulombic efficiencies are presented in Figures 14c and d, respectively. The delithiation capacities decrease for the modified samples at low rate, whereas constant capacity values are observed for the pristine graphite electrode (Figure 14c). A massive drop in capacity from 335 mAh g^{-1} to 97 mAh g^{-1} appears for the modified samples when applying a higher current. This drop (71 %) is much higher than for the pristine (28 %), which gives reason to assume slower intercalation kinetics due to blocked intercalation channels for the modified electrodes. Moreover, the ethynyl (TIPS) values at 1C fluctuate, indicating inhomogeneous SEI formation, which may be attributed to the creation of “pinholes” on the surface as described in [84]. In addition, efficiencies in the first cycle of both samples noticeable dropped by 10 % compared to pristine, indicating more irreversible side reactions during the first lithiation (Figure 14d). Although, the difference in efficiencies at C/10 compared to the pristine is not as drastic as in the first cycle, the consumption of lithium-ions due to side reactions is more distinct for the modified samples (Figure 14d, inset). It is assumed that the formed SEI is not stable, as side reactions proceed even after 5 cycles. However, after two cycles at 1C the efficiencies are comparable to the pristine electrode.

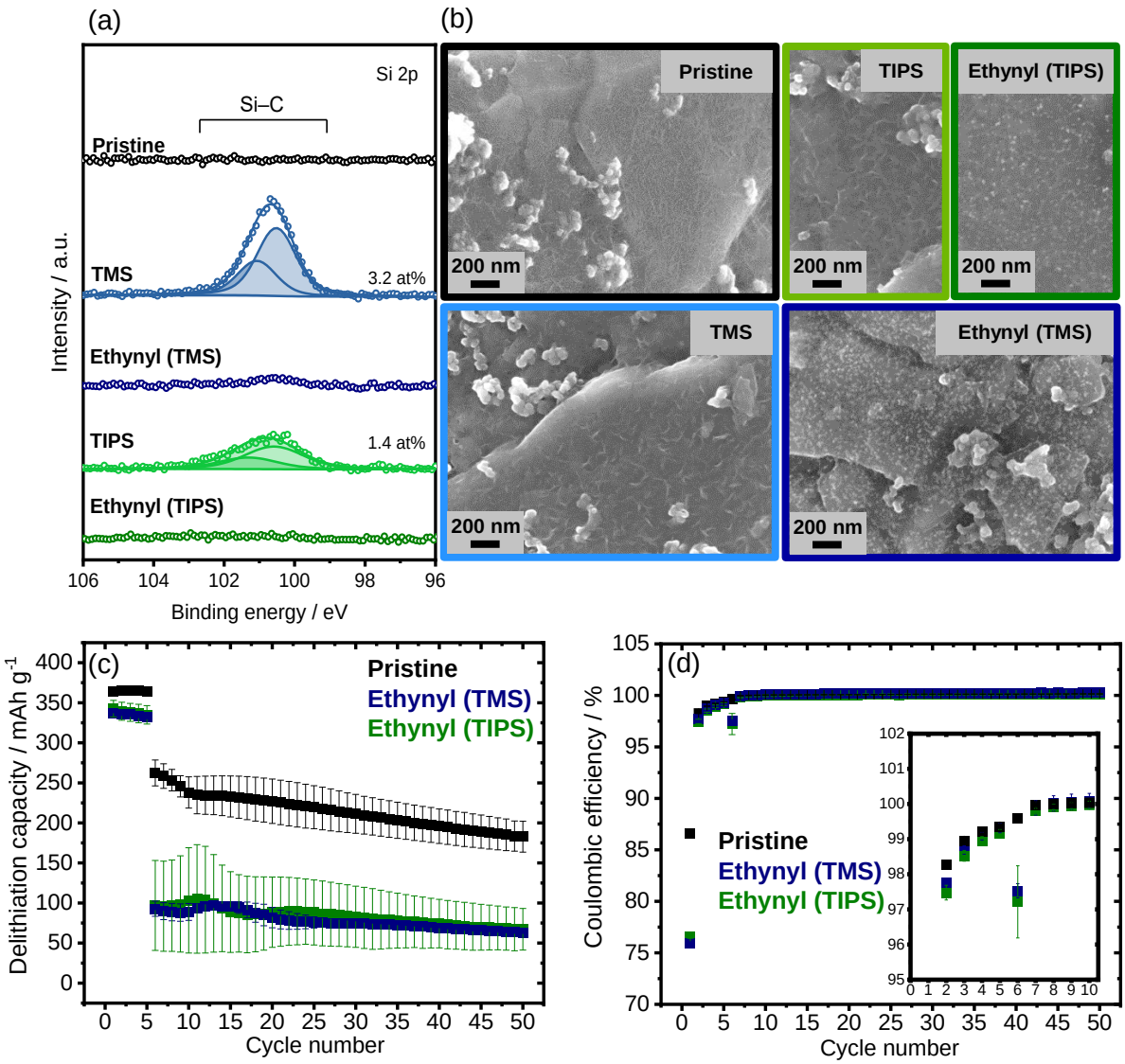

Figure 14. (a) Si 2p spectra and (b) SEM images of pristine, electrografted and deprotected electrodes, (c) electrochemical cycling stability at C/10 for 5 cycles and 1C for 45 cycles and (d) corresponding Coulombic efficiencies of the pristine and deprotected electrodes.

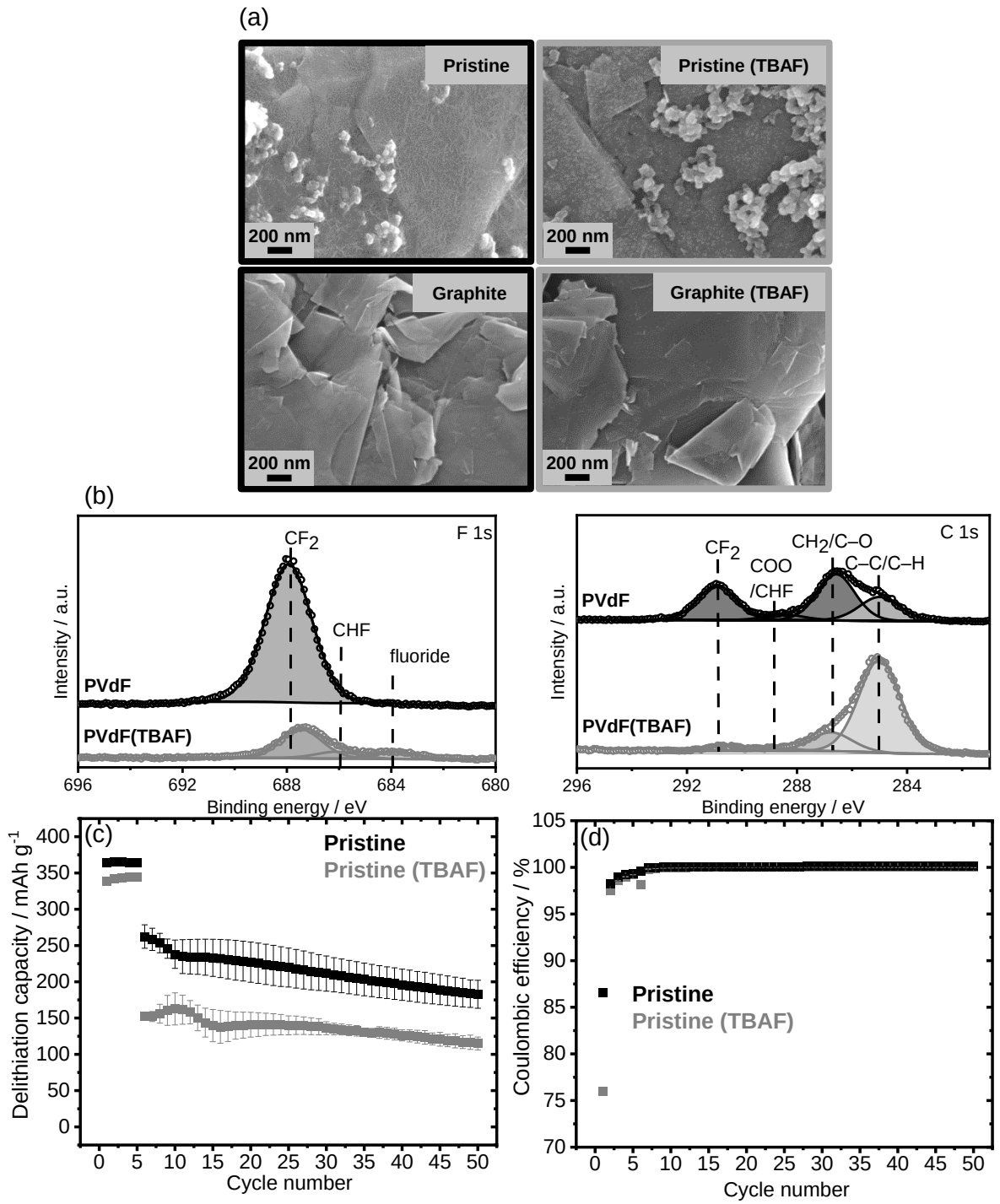

Figure 15. (a) SEM images of pristine and with TBAF treated graphite electrode and graphite powder, (b) C 1s and F 1s spectra of pristine and with TBAF treated PVdF binder, (c) electrochemical cycling stability at C/10 for 5 cycles and 1C for 45 cycles and (d) corresponding Coulombic efficiencies of pristine and with TBAF treated graphite reference electrode.

We investigated whether the spots appearing on the surfaces of ethynyl (TMS) and ethynyl (TIPS) could also contribute to the poor performance. Therefore, a pristine electrode and bare graphite powder were treated with the deprotection agent (TBAF 0.1 M in THF) and characterised by SEM (Figure 15a). Since the surface of treated graphite powder is free from

spots but the treated electrode is not (*Figure 15*a), the spots originate from a decomposition of the PVdF binder. To further investigate this phenomenon, XPS measurements of pristine PVdF powder and PVdF treated with deprotection agent were conducted. Figure 15b shows the C 1s and F 1s XPS spectra of the two corresponding powders. The C 1s regions were deconvoluted into four peaks: C–C/C–H at 285.0 eV, CH_2/C–O at 286.6 eV, COO/CHF at 288.5 eV and CF_2 at 290.9 eV.[129] CH_2 and CF_2 refer to the bonds in PVdF, of which the intensities drastically decrease after treatment with TBAF. The peak in the F 1s region at around 687.9 eV represents CF_2 in PVdF, which decreased after deprotection. Moreover, two additional peaks at 683.8 eV for fluoride and 686.1 eV for CHF can be observed for the deprotected sample. C 1s and F 1s spectra of the corresponding electrodes can be found in Figure S1. It is notable that during the preparation of the PVdF (TBAF) sample, it was observed that the originally white PVdF powder immediately turns to black when immersed in the deprotection agent (Figure S2). This observation and the XPS results confirm the assumption that side reactions occurred when the PVdF containing electrode was treated with deprotection agent. This is in line with the electrochemical results demonstrated in Figure 15c–d. The graphite electrode, which was solely treated with TBAF exposes a decrease of delithiation capacity and efficiency in the first cycle in comparison to the pristine electrode. These observations point out that a treatment with TBAF causes a visible change of the electrode surface and decomposition of the binder, resulting in poor electrochemical performance. The effect of binder decomposition could likely affect the impact of the grafted surface groups. To avoid side reactions with PVdF, all experiments were repeated using CMC/SBR instead PVdF. However, SEM and XPS reveal decomposition of CMC binder most likely due to deacylation after treatment with deprotection agent,[130] which negatively influences the electrochemical performance of the electrodes as well (Figure S3 and Figure S4). Since the role of the binder is to ensure good particle-particle cohesion and particle-current collector adhesion to enable stable cycling, it is not surprising that binder decomposition results in poor electrochemical performance. Nonetheless, capacities of ethynyl (TMS) and ethynyl (TIPS) are even lower compared to the TBAF treated pristine electrode, which proposes an additional influence of the electrografting process and/or the ethynyl functionality. Therefore, additional functional groups were investigated.

5.2 Electro- and *in situ* grafting of functionalised aryl diazonium salts

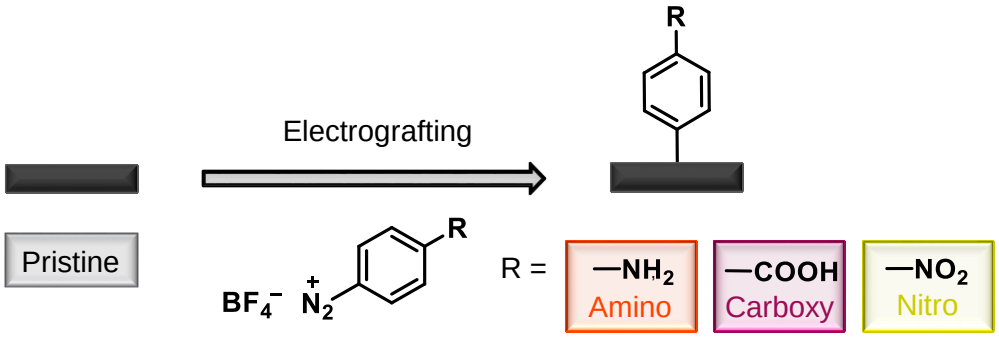

Scheme 2. Electrografting of amino, carboxy and nitro aryl diazonium salts to graphite electrodes.

To avoid binder decomposition by a deprotecting agent, ADS with amino, carboxy and nitro moieties were electrografted to graphite electrodes (Scheme 2). The electrografted samples are referred to as amino, carboxy and nitro. In this case, no secondary deprotection step is needed after grafting. Surface analyses *via* XPS and SEM are displayed in Figure S5. The characteristic N 1s peaks for amino and nitro groups as well as O 1s peaks for carboxy groups confirm successful grafting of the salts. Looking at the influence of these groups on the electrochemical behaviour, it can be seen that all electrografted samples show reduced delithiation capacities, especially at a higher current density (Figure 16a). Even though the electrodes were not treated with an additional deprotecting agent, the capacities are not improved compared to Ethynyl (TMS) and Ethynyl (TIPS). A reasonable explanation for this behaviour is the radical mechanism of electrografting.[50] Due to the absence of a protecting group, the formation of dense multilayers is more likely, which may block the graphite surface and hinders lithium-ion intercalation. The thick layer could also inhibit electrolyte penetration and change the porosity of the electrode and therefore lead to lower capacities.[131] The initial capacity loss for carboxy and amino are close to the pristine electrode, whereas it increases for nitro (Figure 16b). The efficiencies of amino in the following cycles are similar to the pristine and nitro. Especially carboxy shows reduced efficiencies at C/10. After the current change, amino and nitro show efficiencies similar to the pristine, whereas for carboxy the efficiencies are still below the pristine after 10 cycles. The addition of functional groups *via* electrografting is expected to lead to a more reactive surface, which would promote more side reactions upon cycling, especially for reducible functional groups.[49]

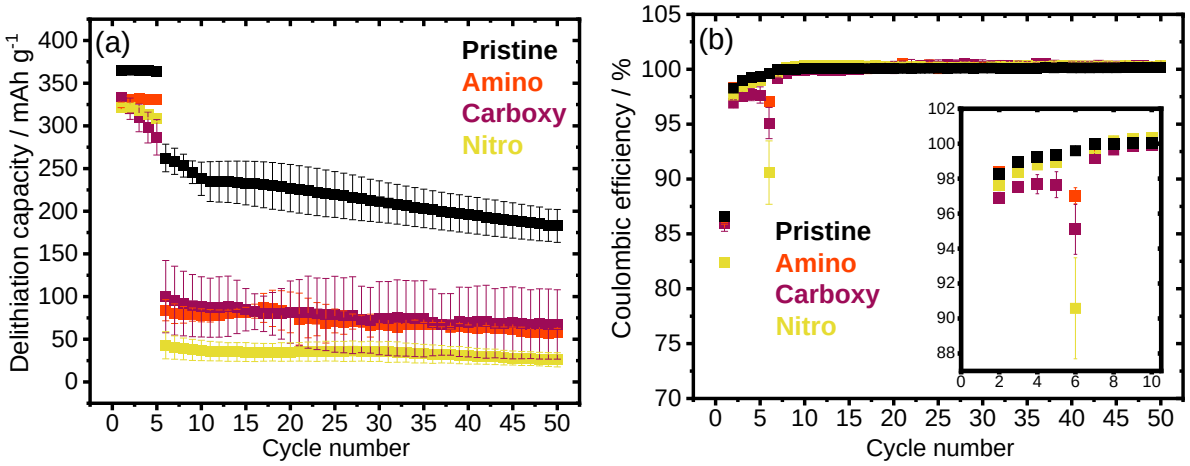

Figure 16. (a) Electrochemical cycling stability at C/10 for 5 cycles and 1C for 45 cycles and (b) corresponding Coulombic efficiencies of pristine and electrografted amino, carboxy and nitro electrodes.

To preserve free intercalation channels, another modification method was tested. Functionalised aryl anilines were mixed with diazotisation reagent and graphite powder in an acidic aqueous solution. Since the corresponding ADS are *in situ* formed and grafted to the graphite powder, this method is referred to as *in situ* grafting (Scheme 3).[48] Since for *in situ* grafting the graphite powder is modified before the preparation of the electrode, deprotection of TMS can be done without decomposition of the binder. The resulting electrodes are referred to as TMS, ethynyl (TMS), amino, carboxy and nitro. Again, the appearance of a Si 2p peak for TMS and subsequent disappearance after deprotection confirms successful grafting *via* the *in situ* method (Figure 17a). For the amino and nitro groups, nitrogen works as marker molecule. The N 1s peak of amino which is observed after *in situ* grafting was fitted with two components of –N< at 399.3 eV[132] and N= at 400.7 eV[132]. For the Nitro sample, an additional N 1s peak at 405.7 eV[133] corresponding to $–NO_2$ appears as expected. For Carboxy, both O 1s spectra were deconvoluted by a peak of COO at lower binding energy and a peak of C–O at higher binding energy. Despite the shift in binding energy due to the charging effect, the

intensity of COO and C–O peaks increased after *in situ* grafting, indicating that the electrode was successfully modified.

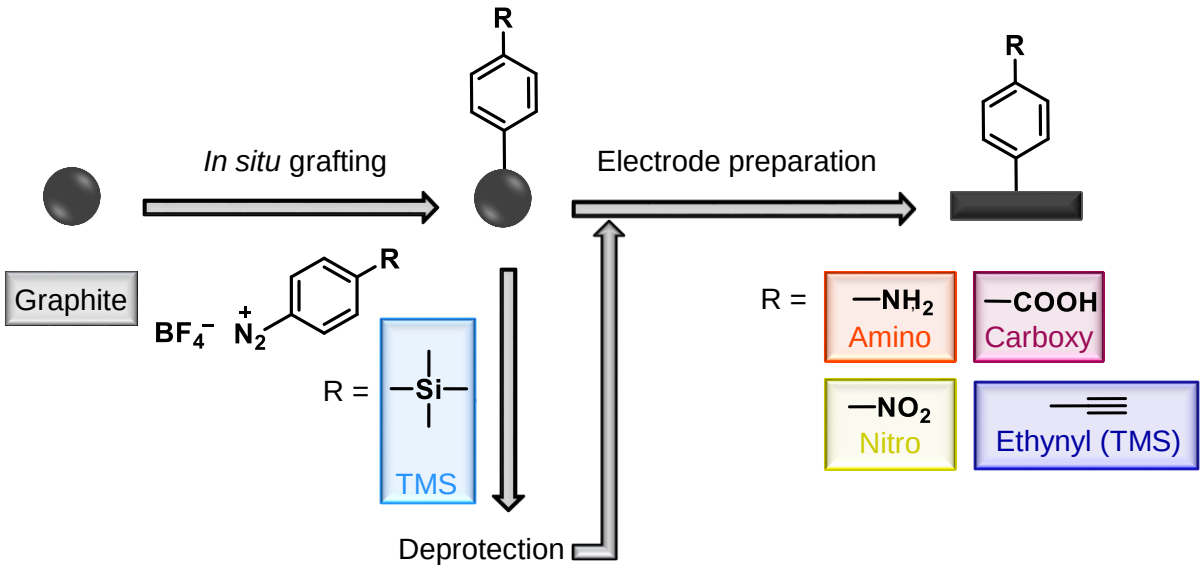

Scheme 3. *In situ* grafting of amino, carboxy and nitro aryl diazonium salts to graphite electrodes.

None of the *in situ* grafted samples shows the fibre-like structure of PVdF in the SEM images (Figure 17b). Carboxy shows a morphology similar to the pristine, whereas ethynyl (TMS), nitro and amino look like they are covered by a film, which supports that multilayer formation also occurs by using this method (Figure 17b). However, the spots observed for electrografted ethynyl (TMS) do not appear for *in situ* grafted ethynyl (TMS), which confirms the side reactions of TBAF with PVdF.

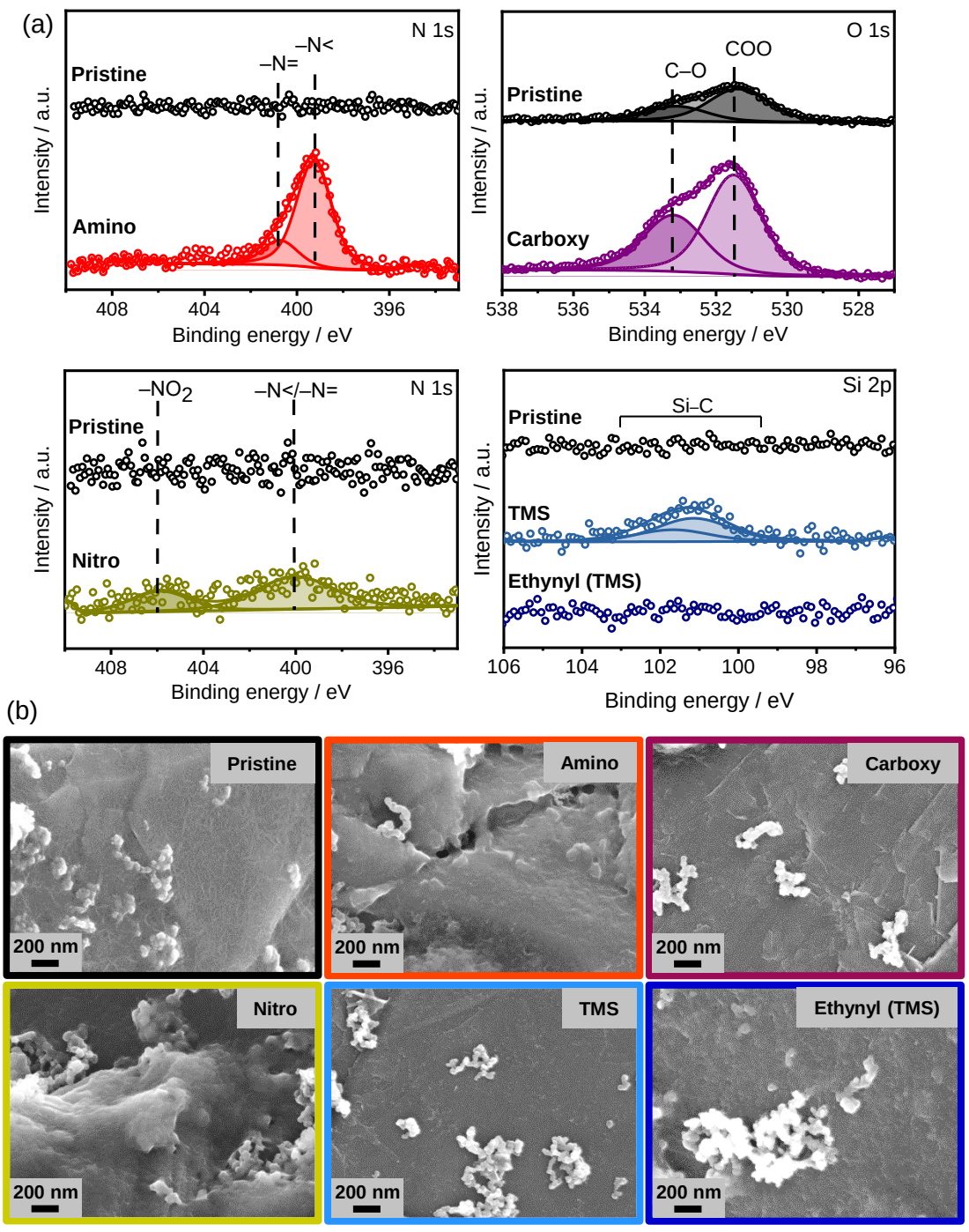

Figure 17. (a) N 1s, O 1s and Si 2p spectra and (b) SEM images of pristine, *in situ* grafted (and deprotected) electrodes.

Compared to the electrografted samples, *in situ* grafted samples, except amino, show higher delithiation capacities, (Figure 18a). Amino shows a drastic capacity decrease and delivers almost no capacity at higher current densities, hence, the Coulombic efficiency of >100 % is not meaningful, as the material is not electrochemically active anymore and the charge transfer cannot be attributed to electrochemical storage processes. The very low capacity (less than 13 mAh g^{-1}) stems from capacitive storage which in this case is not regular. Amino groups being activating substituents may cause different grafting behaviour and different

electrochemical performance. The capacities of the carboxy sample are comparable to the pristine sample. Ethynyl (TMS) has still a higher capacity (245 mAh g^{-1}) and cycling stability than the pristine (238 mAh g^{-1}) after ten cycles. This trend is preserved up to 45 cycles with a capacity retention of 84 % for ethynyl (TMS) compared to 70 % for the pristine. This means that fewer lithium-ions are consumed for SEI formation and are therefore further available for (de)intercalation. However, at C/10 the capacities drop after the first cycle, due to an increase of side reactions. Even though the efficiencies in the first cycle are higher than for the pristine, this trend changes in the following cycles at low current densities (Figure 18b). This was also noted for electrografted samples and attributed to increased reactivity of the surface due to an incorporation of functional groups.

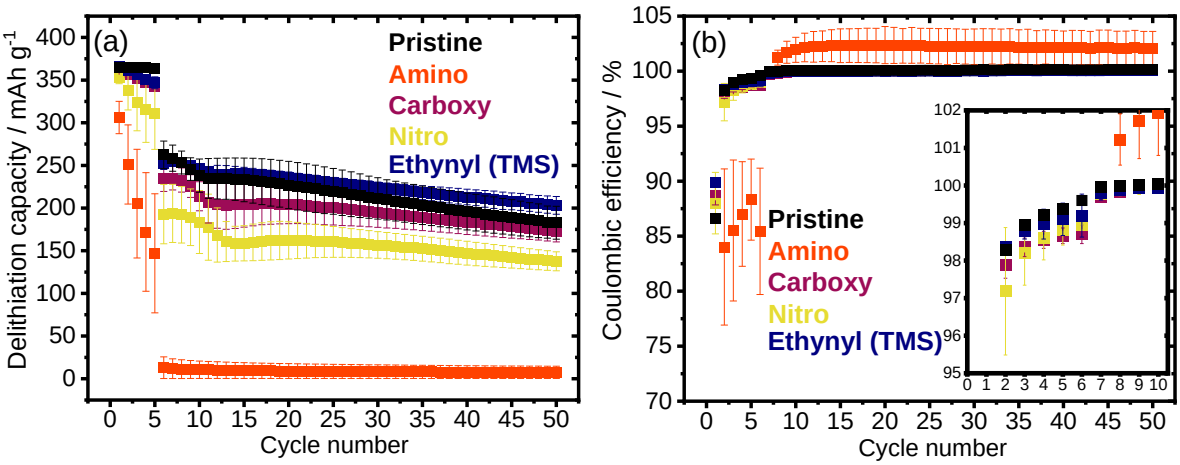

Figure 18. (a) Electrochemical cycling stability at C/10 for 5 cycles and 1C for 45 cycles and (b) corresponding Coulombic efficiencies of pristine and *in situ* grafted (deprotected) electrodes.

5.3 Differential capacity analysis

SEI formation includes the reduction of electrolyte components and subsequent precipitation of decomposition products on the electrode's surface.[33] *In situ* grafted samples show the presence of the ethylene carbonate (EC) reduction peak at ~0.8 V[134] (except amino), whereas this peak is suppressed or even absent for electrografted samples (Figure 19a,c,d, insets). Despite the consumption of lithium-ions during EC reduction, the *in situ* grafting increased the initial Coulombic efficiency for nitro (88 %), carboxy (89 %) and ethynyl (TMS) (90 %) compared to electrografted analogues (82 %, 86 % and 76 %, respectively). It is well known that additives like vinylene carbonate (VC) stabilise the SEI due to polymerisation effects.[135] It is likely that triple bonds polymerize as well and therefore influence the properties of the SEI, which can be observed for ethynyl (TMS). It is expected that the polymerisation is not finalised during the low rate cycling, but already sufficiently developed to enhance the performance at

high rates. No enhanced rate capability was observed for the electrografting process as the groups are probably arranged too dense and therefore inhibit the insertion of lithium-ions.

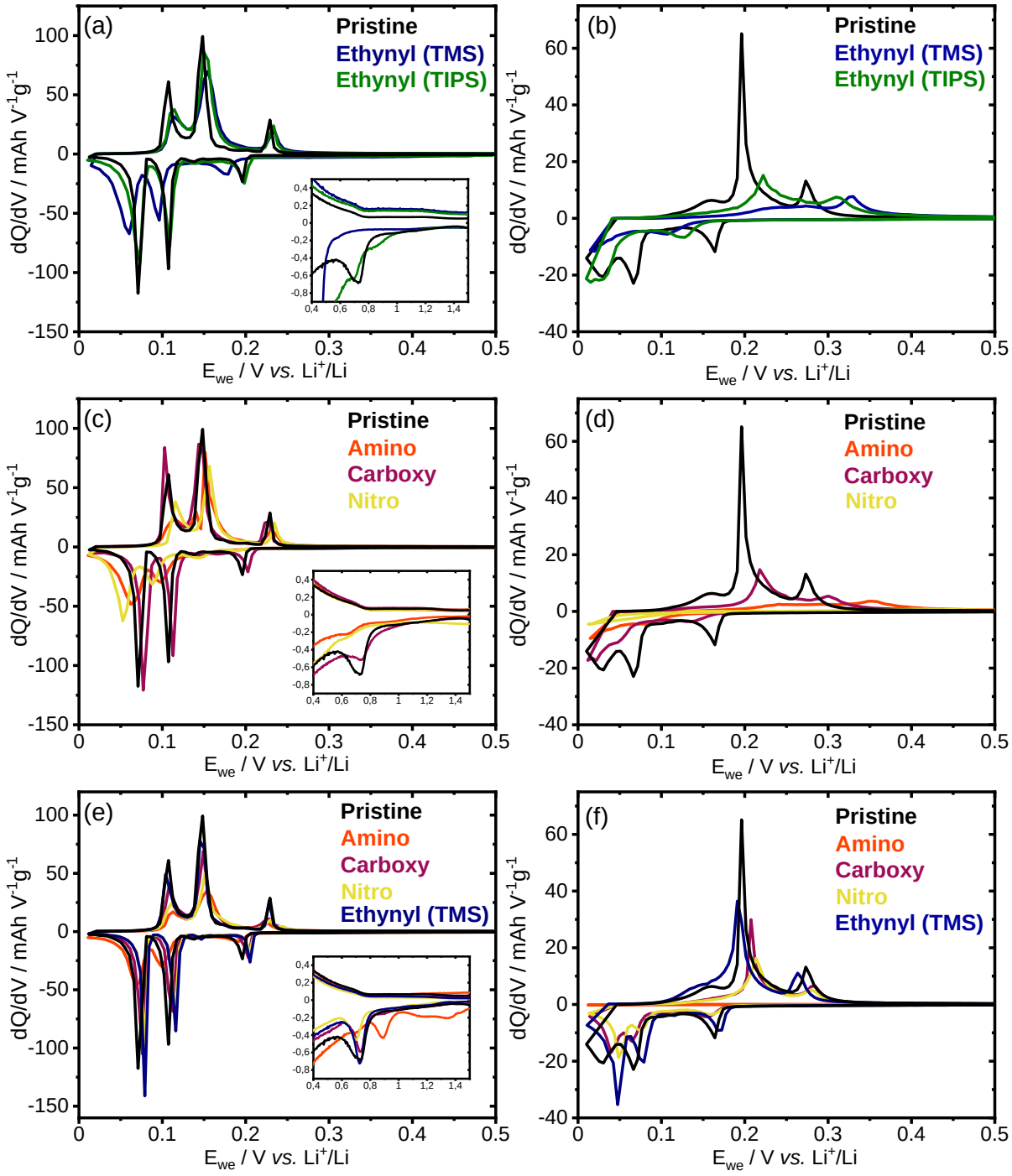

Figure 19. dQ/dV plots of the first and 10th cycle of pristine and (a),(b) electrografted ethynyl (TMS) and ethynyl (TIPS); (c),(d) electrografted electrodes amino, carboxy, nitro and (e),(f) *in situ* grafted amino, carboxy, nitro and ethynyl (TMS).

Differential capacity plots of the first cycle (Figure 19a) additionally show that the lithium-ion transport is much more affected by ethynyl (TMS) than ethynyl (TIPS), given that the reduction peaks are broadened and shifted to lower potentials. After removing the protecting group, there is no difference in the chemical structure of ethynyl (TMS) and ethynyl (TIPS), but the amount

of ethynyl groups on the surface is higher for ethynyl (TMS). The rigidity of the dense grafted ethynyl groups and the resulting network during reduction seems to alter the lithium-ion transport. This effect is attenuated if the ethynyl groups are grafted less dense as in ethynyl (TIPS). However, the transport during oxidation is also affected by ethynyl (TIPS) in a similar manner as by ethynyl (TMS), which means the ethynyl group and the resulting decomposition products affect lithium-ion transport in general for samples prepared by the described synthesis route. Differential capacity plots of the 10th cycle confirm this (Figure 19b).

Broadened and to lower potential shifted reduction peaks in the first cycle are also observed for nitrogen-containing amino and nitro groups (Figure 19c) what also intensifies in the 10th cycle (Figure 19d). However, for carboxy groups, the reduction peaks are slightly shifted to higher potentials and still very sharp. Even though those peaks deteriorate in the 10th cycle (Figure 19d), they are more pronounced than those of amino and nitro electrodes. Due to multilayer formation, a high number of functional groups is available on the electrode surface, also it is very likely that the grafted layer is thicker than for the ethynyl groups. The resulting SEI film alters the lithium-ion transport, which intensifies over cycling (Figure 19d). Therefore, the results from Figure 19a–d affirm the assumptions made earlier for the capacity and efficiency decrease in Figure 14c–d and Figure 16a–b.

For *in situ* grafted samples, all reduction peaks in the first cycle are sharp and shifted to higher potentials, except amino (Figure 19e). The reduction peaks of amino are broadened and shifted to lower potentials in the first cycle, whereas in the 10th cycle just a flat line is observed, since amino does not deliver any capacity at this point anymore (Figure 19f). For the other samples even at the 10th cycle, the reduction peaks are preserved unlike for electrografted samples. Lithium-ion transport is even enhanced for ethynyl (TMS), given the sharp peaks which are shifted to lower/higher potentials during reduction/oxidation, respectively. Although, *in situ* grafting does not prevent multilayer formation, the grafted layer is not as dense and thick as it is for electrografted samples, which seems to have a positive impact on lithium-ion transport. However, the performance of carboxy and nitro electrodes still is inferior to the pristine at low and high current densities. Additional surface analysis is needed for a deeper understanding of the effect originating from the *in situ* grafted functional groups. However, Figure 19 reveals that the more the EC reduction peak is suppressed, the more the lithium-ion transport is negatively affected at low and high rate. This concerns especially the electrografted samples, whereas the *in situ* grafted samples show defined EC reduction peaks and better lithium-ion transport at low and high rate. These findings correlate with the observed capacity values of all samples.

These results reveal that the grafting process highly influences the electrochemical performance of the functionalised electrodes. A main difference between the two grafting methods is that during *in situ* grafting solely the active material graphite is modified, whereas

during electrografting the conductive additive and even the binder are impaired. The observation of binder degradation caused by side reactions with the deprotection agent reinforces this assumption. The combination of possible grafting on inactive materials (conductive additive and binder) and dense multilayer formation (as discussed earlier) seem to have a bad impact on the electrode-electrolyte interface and result in poorer performance. As stated by Shodiev *et al.*[131], the porosity and pore network organisation has a great impact on the penetration of the electrode with electrolyte. By covering graphite and conductive additive with a thick functionalised layer, the penetration with electrolyte could be impaired and influence the SEI formation. Adhesion properties of the binder to the current collector and graphite could also be affected. However, additional analytic characterisation is needed to investigate the resulting SEI properties.

5.4 Conclusive aspects

Various functionalised aryl diazonium salts were used to successfully modify graphite electrodes *via* electro- and *in situ* grafting. In the case of alkyl silyl protected ethynyl aryl diazonium salts, the deprotection agent TBAF caused side reactions with PVdF as well as CMC/SBR binder. The resulting decomposition negatively affected the electrochemical performance of the modified electrodes for their application in LIBs. However, other functional groups such as amino, carboxy and nitro, for which no deprotection step is needed, show poor electrochemical performances as well. This was associated with multilayer formation during electrografting. Therefore, *in situ* grafting was studied as an alternative technique. The *in situ* modified graphites show better electrochemical cycling performance, increased Coulombic efficiency in the first cycle and faster lithium-ion intercalation kinetics. Ethynyl (TMS) even increased the capacity to 238 mAh $g^{-}1$ at 1C and shows capacity retention of 84 % after 45 charge-discharge cycles, meaning more lithium-ions are available for (de)intercalation. This work demonstrates that not only the functional group itself but also the method of formation must be considered to reveal the impact of functional groups at graphite electrodes for lithium-ion batteries. Concerning the introductory questions, it can be concluded that the hydrophilicity of the functional group does not determine the performance and a non-reducible group such as amino does not guarantee superior efficiencies. The preparation method, on the other hand, is of crucial importance. Especially for the design of a covalent artificial SEI, the selection of eligible terminal groups and how several building blocks are included in the artificial network are of great significance. Insight was provided into the design of suitable anchor groups *via* diazonium chemistry and the challenges of surface modification methods. Ethynyl groups offer good possibilities for post-functionalisation *via* alkyne Click chemistry.[82], [136], [137] The layered surface could be customised in terms of pore size and polarity to further improve SEI formation and lithium-ion (de)intercalation and help to reduce irreversible capacity loss.

6. Modification with pyrenes

The previous Chapter 5 gave insight into covalent modification of graphite and graphite electrodes. In contrast, the following Chapter examines a non-covalent modification method by using functional pyrenes. Unlike aryl diazonium salts, modification with pyrenes does not disrupt the aromatic system of graphite. Here, the influence of carboxy and amino moieties is investigated and it is examined whether interaction of pyrenes with graphite are of importance. The Subchapters 6.1–6.4 are extracted from the submitted manuscript “Crucial interactions of pyrene-functionalised graphite for lithium-ion batteries”[76]

6.1 Adsorption of functional pyrenes to graphite

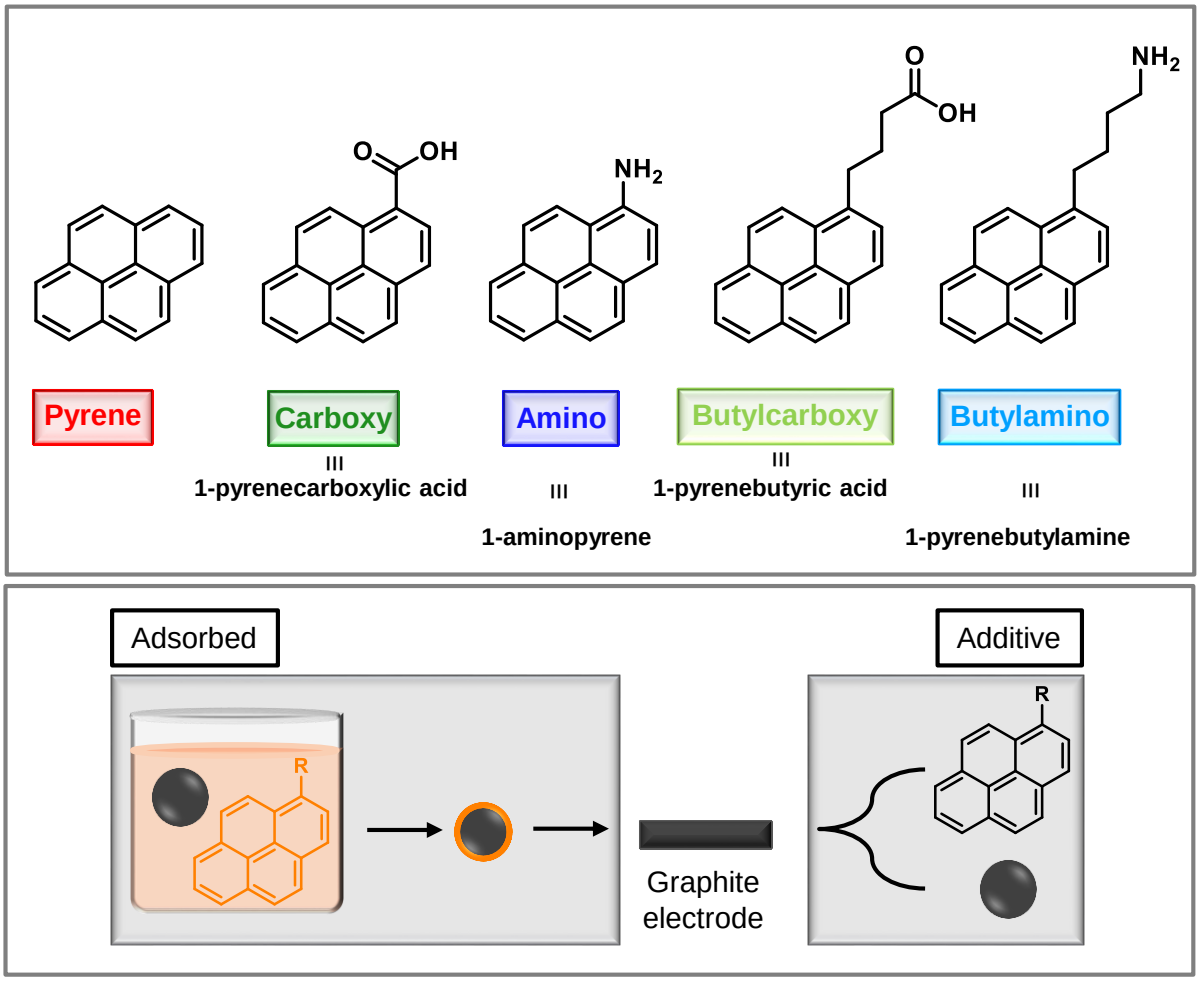

Figure 20. Chemical structures of the pyrenes and methods used in this chapter.

For the sake of clarity, the functionalised pyrenes will be labelled as carboxy, amino, butylcarboxy and butylamine (see Figure 20). Graphite was stirred in a solution of the corresponding pyrene in DMSO and used for electrode preparation.

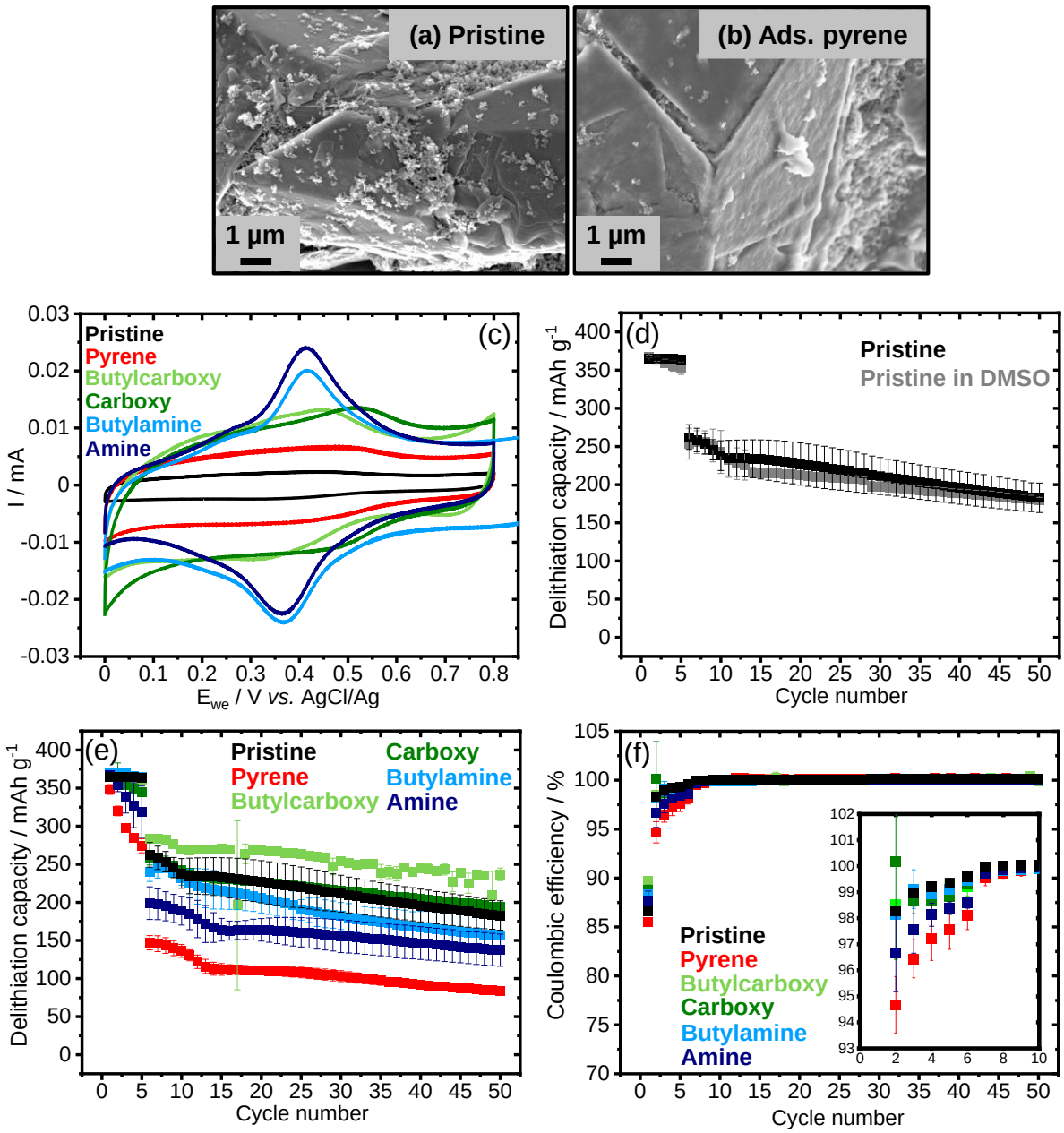

Figure 21. SEM images of (a) pristine, (b) ads. pyrene electrode, (c) CV of adsorbed pyrene graphite powders, (d) electrochemical cycling stability of pristine and with DMSO treated electrodes, (e) electrochemical cycling stability at C/10 for 5 cycles and 1C for 45 cycles and (f) corresponding Coulombic efficiencies of pristine and adsorbed pyrene electrodes.

Figure 21a displays a pristine graphite electrode with carbon black particles as conductive additive decorated on top and in between graphite particles. The morphology of the graphite particles in the modified electrodes appears roughened in comparison to the pristine graphite electrode, which reveals a rather smooth appearance (Figure 21b). In cyclic voltammetry, pyrene-modified powders exhibit higher currents compared to pristine graphite powder (Figure 21c). This is in accordance with the literature, where enhanced double-layer capacitance is attributed to pyrenes used in supercapacitors.[101], [138], [139] The functionalised pyrenes reveal higher currents compared to the pristine pyrene and both amino-functionalised pyrenes show distinct redox peaks at 0.41 and 0.37 V *vs.* AgCl/Ag. This peak was described

as pseudo capacitive behaviour of aminopyrene-functionalised reduced graphene oxide[140]. Additionally, graphite was stirred in pure DMSO overnight prior to electrode preparation to investigate if the method itself has an impact on the electrochemical performance. The delithiation capacity of the pristine and with DMSO treated electrode are shown in Figure 21d. The difference in the first cycle capacity is less than 5 mAh g^{-1} with a retention of 99.8 % and 96.8 % for pristine and the DMSO sample, respectively. The capacity difference at 1C is less than 10 mAh g^{-1} with a retention of 70 % and 71 % for pristine and the DMSO sample, respectively. These values are within the standard deviation of the pristine electrode (see error bars), proofing that the solvent does not influence the electrochemical properties of the electrodes.

Figure 21e displays the capacity values of pyrene-containing electrodes. It is clearly visible that the capacities are affected by the addition of pyrenes when compared to Figure 21d. Pyrenes, which carry functional groups, can indeed enhance the performance of graphite as it is observed in the case of butylcarboxy (Figure 21e). The following key information can be derived from Figure 21e: (1) pristine pyrene performs worst at low and high current densities, (2) carboxy groups perform better than amino groups, especially at high current densities, (3) butylcarboxy and butylamine perform better than carboxy and amine, respectively, (4) butylcarboxy performs equal to the pristine electrode at low current densities and even enhanced the capacity by 20 mAh g^{-1} at high current and the capacity retention by 14 % compared to pristine. The trends (1)–(3) observed for capacities are also valid for initial efficiencies, where pyrene performs worst, carboxy groups reveal higher efficiencies than amino groups and functional groups with butyl groups perform better than without (Figure 21f). Except for pyrene, for all modifications the Coulombic efficiency of the first cycle slightly increased. Compared to 87 % for pristine graphite butylcarboxy shows an enhanced initial efficiency of 90 %. For pyrene and amine, the capacity and efficiency at C/10 drops compared to the pristine sample. Due to the lack of functional groups, pristine pyrene offers less active sites for SEI formation, which could lead to a less effective surface passivation.[38], [102] Pristine pyrene may even cover native surface oxygen groups of graphite rendering them inaccessible as anchor points during SEI formation. In contrast, the amino group offers an anchor group for SEI formation. Even though the amino group is not reducible, it is a nucleophilic substituent and changes the reactivity of the pyrene molecule. These aspects seem to positively influence the SEI formation and could explain the better performance compared to pristine pyrene. The butylamine sample shows even higher capacities and efficiencies than the amine. A possible explanation could be that the addition of a butyl moiety indeed increases the accessibility of the amino group and hence positively influences the SEI formation. Further, the lone-pair of nitrogen in the amine sample is conjugated to the aromatic ring system of pyrene (+M-effect), which is not the case for the butylamine sample. Additionally, the electron density of nitrogen

is affected by the inductive effect (+I-effect) of the butyl moiety. These effects make the butylamine sample more nucleophilic than the amine sample, which could lead to a better formation and anchoring of the SEI layer.

The efficiencies of butylcarboxy are within the error range of the pristine electrode, whereas carboxy shows slightly decreased efficiencies. The capacity of the carboxy sample is comparable to the pristine graphite electrode, whereas the butylcarboxy sample clearly shows enhanced capacity compared to the pristine. This is in line with the literature, where reducible surface oxygen groups are described to function as nucleation sites for the formation of a stable SEI,[38], [102] which could also explain the superior performance of reducible carboxy groups compared to non-reducible amino groups. The positive effect of the additional butyl group could also stem from the better steric accessibility of the carboxy group in the butylcarboxy sample.

6.2 Functional pyrenes as additive in graphite electrodes

It is assumed that the pyrenes do not just act as additives providing certain functional groups and being consumed during the SEI formation, but that it is essential that they are adsorbed to the graphite surface to provide a beneficial contribution to the formation and stability of the SEI layer. To investigate this assumption, 1 % w/w pyrene and amino, butylamino, carboxy and butylcarboxy pyrenes were added as additive to a graphite electrode.

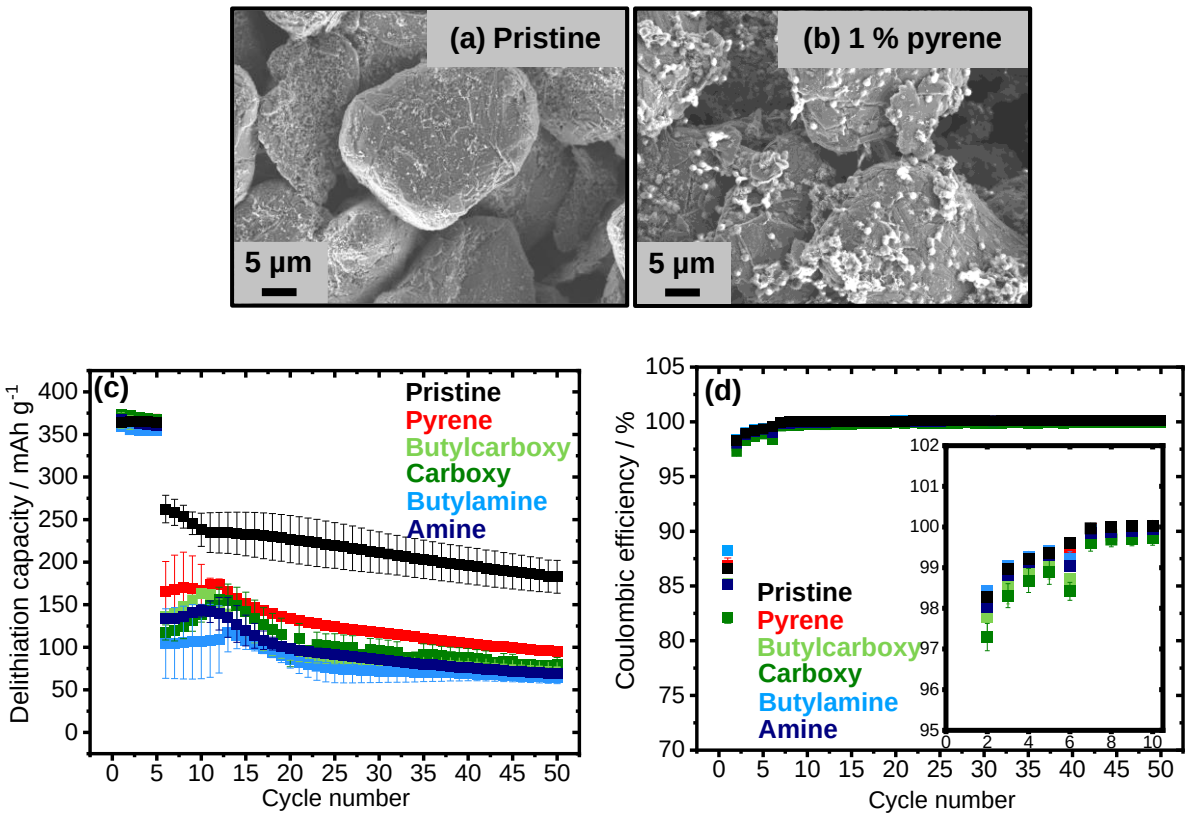

Figure 22. SEM images of (a) pristine, (b) 1 % w/w pyrene electrode, (c) electrochemical cycling stability at C/10 for 5 cycles and 1C for 45 cycles and (d) corresponding Coulombic efficiencies of pristine and pyrene electrodes.

The SEM image of an electrode with 1 % w/w pyrene shows an equal distribution of spherical pyrene particles, which are attached to graphite and conductive carbon (Figure 22b). Pyrene particles are also attached to each other forming a network around graphite. The electrochemical cycling performance and Coulombic efficiencies are displayed in Figure 22c–d. The capacity values of pyrene-containing electrodes at a cycling rate of C/10 are comparable to the pristine graphite electrode, whereas their capacity visibly drops at 1C. Pure pyrene performs best at 1C among all pyrene-containing electrodes, exhibiting delithiation capacities of 166–95 mAh g^{-1} at 1C. The lowest capacities of 104–64 mAh g^{-1} were obtained using butylamine at 1C. The presence of pyrene particles does not seem to notably influence the capacity of the electrode at C/10 in contrast to 1C where the capacity drops by at least 37 % compared to the pristine. The Coulombic efficiency in the first cycle of the pyrene-containing is equal to the pristine electrode (87 %). For butylamine the efficiency of the first cycle is enhanced by 1 %, while amine and butylcarboxy show efficiencies reduced by about 2 %. The efficiency of carboxy samples is even further reduced by about 5 %. In the following cycles especially the carboxy samples show decreased efficiencies compared to the pristine electrode. It is notable that the efficiency of butylamine is superior to amine and butylcarboxy is superior to carboxy.

Regardless of the functional group, the cycling performances of the electrodes with pyrene as additive are deteriorated at high current densities, but do not seem to influence the performance at low current densities. The presence of aggregated pyrene particles on the graphite surface (see Figure 22b) seems to have a significant contribution to the inner resistance at high current densities. However, this contribution appears to be neglectable at low current densities, because under these conditions graphite offers sufficient electronic pathways due to its higher conductivity compared to pyrene[141]–[144]. Another explanation could be that the pyrene agglomerates act as local nucleation sites, leading to a SEI with inferior properties compared to the pristine graphite. Therefore, pyrenes as additive seem not to support anchoring of SEI components to the graphite surface during growth. In addition, the pyrenes are at least partly soluble in the electrolyte so that they could dissolve and directly interfere with the SEI formation process again resulting in an inferior SEI.

6.3 Differential capacity analysis

The differential capacity was calculated and plotted *versus* voltage to further investigate the electrochemical behaviour of all electrodes in the first and 10th cycle (Figure 23a–d). The reduction peak at ~0.7 V in the first cycle is ascribed to the reduction of ethylene carbonate (EC)[134] and is visible for all samples (Figure 23a,c, insets). As additive, butylcarboxy, butylamine and amine show an additional reduction peak at 0.9 V and carboxy at 1.2 V (Figure 23c, inset). The two reduction peaks are most pronounced for carboxy, which is in correlation with the low first cycle efficiency. Pyrene does not show an additional peak in this area, which makes it plausible that those peaks are linked to reactions with the functional groups. However, except for butylamine those peaks are not visible for adsorbed pyrenes (Figure 23a, inset). The EC reduction peak of the adsorbed pyrenes did neither shift nor change their height, except for butylamine, where the height increased. A possible explanation for this observation could be the different amounts of pyrenes in the electrode due to different modification methods, assuming there is a smaller amount of adsorbed pyrenes and hence the absence of the additional peaks. However, those peaks in the insets of Figure 23c seem to arise from additional irreversible reactions with the pyrenes itself and may not be connected to the electrolyte reduction reactions.

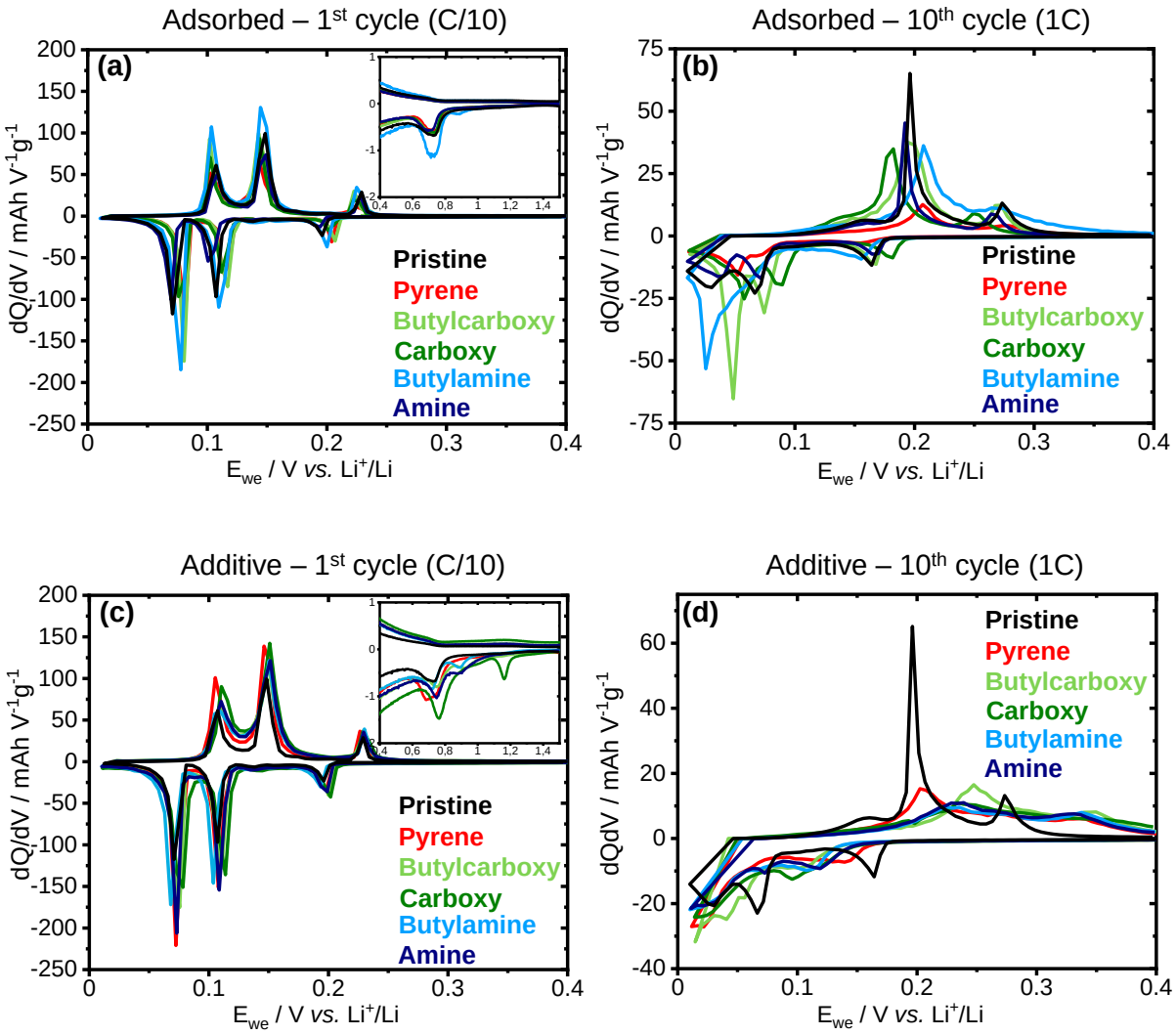

Figure 23. dQ/dV plots of the first (C/10) (a) and 10th (1C) cycle (b) of pristine and pyrenes as additive electrodes and first (C/10) (c) and 10th (1C) cycle (d) of pristine and adsorbed pyrenes electrodes.

In the first cycle (C/10), the reduction peaks of all electrodes containing adsorbed pyrenes are shifted to higher potentials, indicating enhanced lithium-ion transport (Figure 23a). In the 10th cycle (1C), it is noticeable that for the adsorbed variant (Figure 23b) butylcarboxy and butylamino the reduction peaks between 0.01 and 0.1 V *vs.* Li^+/Li have a much higher height compared to the carboxy, amino, pyrene and the pristine electrodes. The reduction peaks of carboxy samples are shifted to higher potentials compared to the pristine and amino electrodes, indicating enhanced lithium-ion transport. Especially butylcarboxy shows sharp and intense peaks in the 10th cycle. Figure 23b reassures the positive influence of the additional butyl group in the functionalised pyrene samples.

The reduction peaks of the first cycle at C/10 for pyrene additives are slightly shifted to higher potentials for all samples except butylamine (Figure 23c). However, at 1C the lithium-ion transport is deteriorated for all samples, indicated by the peak shift to lower/higher potentials and decreased peak heights during reduction/oxidation (Figure 23d). This affirms that the

influence of aggregated pyrenes on the inner resistance only becomes significant at high current densities.

It is assumed that the lithium-ion transport is facilitated for adsorbed pyrenes, due to the formation of an improved SEI, which is anchored to the graphite surface by adsorbed pyrenes. This becomes most visible for the butylcarboxy sample and would also explain the superior cycling performance.

6.4 Conclusive aspects

In summary, pyrenes with carboxy and amino moieties were studied for graphite electrodes in LIBs. When the pyrenes are adsorbed to the graphite surface, different influences of the functional groups are visible. The assumptions that carboxy groups are superior to amino groups and that butylcarboxy/butylamine are superior to carboxy/amine were confirmed. The additional butyl moieties change the reactivity and steric accessibility of the pyrenes and functional groups, which seems to have a positive impact on the SEI formation. Butylcarboxy even showed an improved cycling performance and better lithium-ion transport compared to a pristine graphite electrode. Such improving effect did not appear for the application of pyrenes as additive, proving that it is crucial to have surface adsorbed pyrenes.

It is noticeable, that the cycling stability of adsorbed carboxy/butylcarboxy and amine/butylamine pyrenes is superior to electro- and *in situ* grafted carboxy and amine aryl diazonium salts (ADS) from Chapter 5, which is especially visible at high current densities. Since the covalent modification with ADS affects the aromaticity of the graphite, the conductivity of the ADS modified graphite electrodes could be impaired. The corresponding pyrenes do not interfere with the aromaticity of graphite, which could be a possible explanation for their better cyclability.

7. Metal-organic frameworks

Various reviews on MOFs and MOF-derived materials for electrochemical energy storage demonstrate their suitability as active material in LIBs (see Chapter 3). In this chapter, it is attempted to synthesise Zn-MOFs on graphite *via* electrodeposition and solvothermal synthesis using BTEB (4,4',4''-(Benzene-1,3,5-triyltris(ethyne-2,1-diyl)tribenzoic acid) and TAP (4,4',4''-(((1,3,5-triazine-2,4,6-triyl)tris(benzene-4,1-diyl))tris(ethyne-2,1-diyl))tribenzoic acid) as ligands. In a second step, the modified graphite powders from solvothermal synthesis were carbonised to achieve ZnO in a carbon matrix. The modified graphite powder structures were studied using powder X-ray diffraction (PXRD) and the morphology of the electrodes using scanning electron microscopy (SEM). The electrochemical performance was evaluated using a three-electrode setup.

7.1 Zn-BTEB and carbonised Zn-BTEB

7.1.1 Synthesis and characterisation of Zn-BTEB

Based on a procedure of Byrne[69], $Zn(NO_3)_2$ and BTEB ligand were heated in a 2:1 molar ratio in DMF at 90 °C for 2 days. The powder x-ray diffraction (PXRD) pattern of the obtained material corresponds to the monoclinic structure of $(Me_2NH_2)[Zn_5(BTEB)_3(\mu_3\text{-}OH)_2(DMF)_2]$ which crystallises in the space group *C*2/*c* (Figure 24a). The SBU consists of pentanuclear Zn(II), which is stabilised by nine carboxy moieties of BTEB. The characteristic Raman peaks of BTEB for CH_2 rocking vibration at 993 cm^{-1}, C-C single bond vibrations at 1109, 1124 and 1167 cm^{-1}, aromatic C=C vibration at 1607 cm^{-1} and C≡C alkyne vibration at 2213 cm^{-1} are displayed in Figure 24b. The corresponding peaks in ZnBTEB are found at 992 cm^{-1}, 1122, 1141 and 1168 cm^{-1}, 1606 cm^{-1} and 2212 cm^{-1}, respectively. Optical microscopy shows needles (some of them star-shaped) of Zn-BTEB (Figure 24c). PXRD and optical microscopy demonstrate the successful growth of Zn-BTEB crystals, therefore, this procedure was used to modify graphite powder in Chapter 7.1.3.

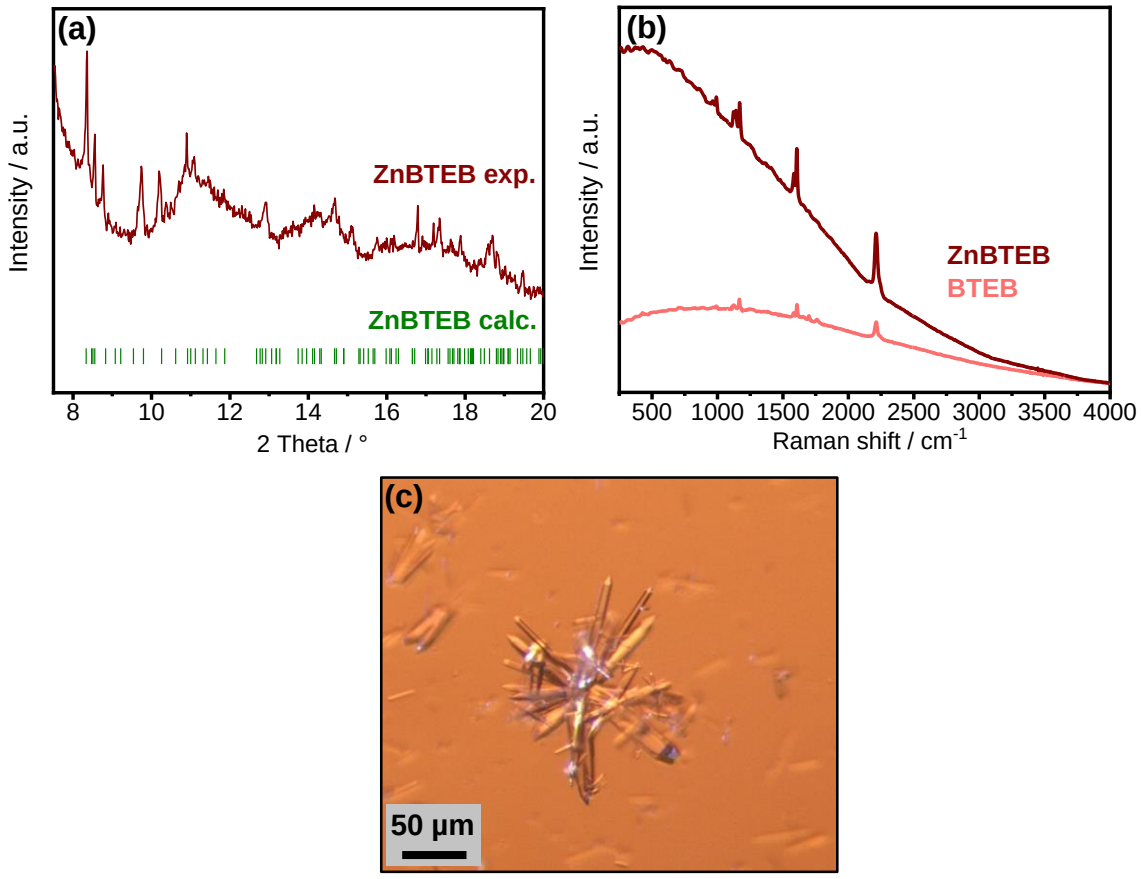

Figure 24. (a) PXRD pattern of the synthesised ZnBTEB material (λ = 1.54056 Å; Bragg reflections positions (green) are calculated based on the data of single crystal XRD analysis from [66]; amorphous-like background at 10 ° < 2θ < 17 ° arises from Kapton film), (b) Raman spectra of BTEB ligand and synthesised ZnBTEB crystals and (c) optical microscope image of synthesised ZnBTEB crystals.

7.1.2 Electrodeposition of Zn-BTEB

Electrodeposition of BTEB-containing MOFs on fluorine doped tin oxide (FTO) has been described by Byrne.[69] On basis of this procedure, graphite electrodes were used as substrate to electrodeposit ZnBTEB at –1.4 V *vs.* Ag(cryptand)$^+$/Ag. XRD did not give distinct information about a successful deposition of ZnBTEB on the graphite electrode. However, Raman spectroscopy gives additional information about the modified sample. Thus, the CH_2 rocking vibration at 990 cm^{-1}, C-C single bond vibration at 1131 and 1169 cm^{-1} and C≡C alkyne vibration at 2210 cm^{-1}, which were observed for BTEB and ZnBTEB, can be seen clearly in the Raman spectrum of ZnBTEB_ED (Figure 25a). The aromatic C=C vibrations most likely overlap with the G-band of graphite at 1582 cm^{-1}. The SEM picture of the pristine electrode shows graphite particles covered with conductive additive, which are connected by the polymeric binder (see green circles in Figure 25b). After electrodeposition, the graphite particles appear to be partly covered by an additional component (see orange circles in Figure 25c), which is even more visible between the particles (see green circles in Figure 25c). It is supposed that the area in the green circles is binder, which was covered during

electrodeposition. It was conspicuous that the modified electrode sheet has a visible white stripe (Figure S6a). The SEM image of ZnBTEB_ED (Figure 25c) shows an area next to the white stripe. A SEM image of the area within the white stripe is shown in Figure 25d, revealing crystal-like structures of different sizes on the electrode surface. Raman spectroscopy showed the presence of BTEB ligand and SEM the presence of a surface coating on the graphite electrode. Even though no characteristic XRD Bragg reflections were found after deposition, SEM images prove the presence of an additional component. However, the growth of this component is not evenly distributed over the electrode surface as shown in Figure 25c–d and Figure S6b. Since XRD could not give any information about the structure of the sample, it is not clear if the surface covering derives from ZnBTEB crystals. However, for the sake of clarity the modified electrode is labelled as ZnBTEB_ED.

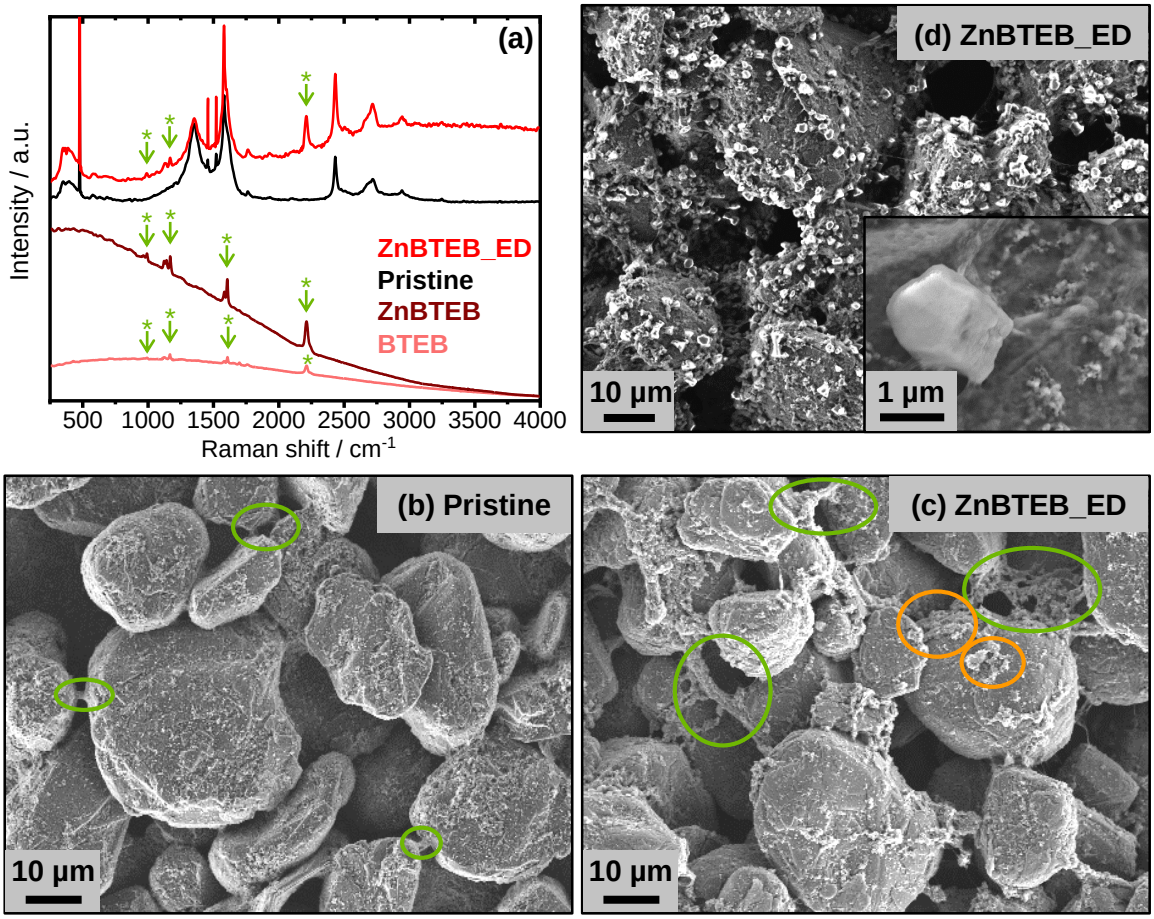

Figure 25. (a) Raman spectra of the pristine graphite electrode and ZnBTEB_ED compared to BTEB and ZnBTEB (green asterisks mark the vibrations of BTEB ligand) and SEM images of (b) the pristine graphite electrode, (c) ZnBTEB_ED measured next to the white stripe and (d) ZnBTEB_ED measured within the white stripe.

Electrochemical cycling experiments were carried out with the attained ZnBTEB_ED electrodes. Figure 26a shows a dramatic decrease of delithiation capacities at C/10. The capacity in the first cycle (351 mAh g^{-1}) is similar to the pristine graphite (365 mAh g^{-1}), but after four further cycles, 24 % of the initial capacity is lost. Even though, the cycling stability

improved at 1C, the delivered capacities are rather low (127 – 72 mAh g-1) compared to the pristine electrode (262 – 183 mAh g^{-1}). The Coulombic efficiency of the first cycle also decreased and even after four more cycles at C/10 the efficiency is visibly deteriorated compared to pristine electrode (Figure 26b). This suggests a significant increase of irreversible side reactions for the modified electrode. However, after three more cycles at 1C, the efficiency is similar to the pristine. The decrease in efficiency, especially at C/10, could be due to the decomposition of the BTEB ligand and/or reactions of ZnBTEB with the electrolyte. Additional information can be drawn from the differential capacity plots (Figure 26c–d). The first cycle of ZnBTEB_ED and the pristine electrode is very similar, but the peak height decreased and the peak width of ZnBTEB_ED increased (Figure 26c). This means that the lithium-ion transport for ZnBTEB_ED is already negatively affected in the first cycle. In the 10^{th} cycle, the peaks visibly shifted to lower/higher potentials during reduction/oxidation and have a very low intensity (Figure 26d), revealing even worse lithium-ion transport for ZnBTEB_ED compared to the pristine. It is assumed that the ZnBTEB layers are permeable for lithium-ions, but the resulting decomposition products deteriorate the lithium-ion transport, starting in the first cycle. Similar to the modification *via* electrografting in Chapter 5, electrodeposition can lead to very thick layers, with a high load of the modifier. This could explain the great amount of side reactions and the resulting low efficiencies in Figure 26b. The more decomposition products emerge upon cycling, the more lithium-ion transport and hence capacity deteriorate.

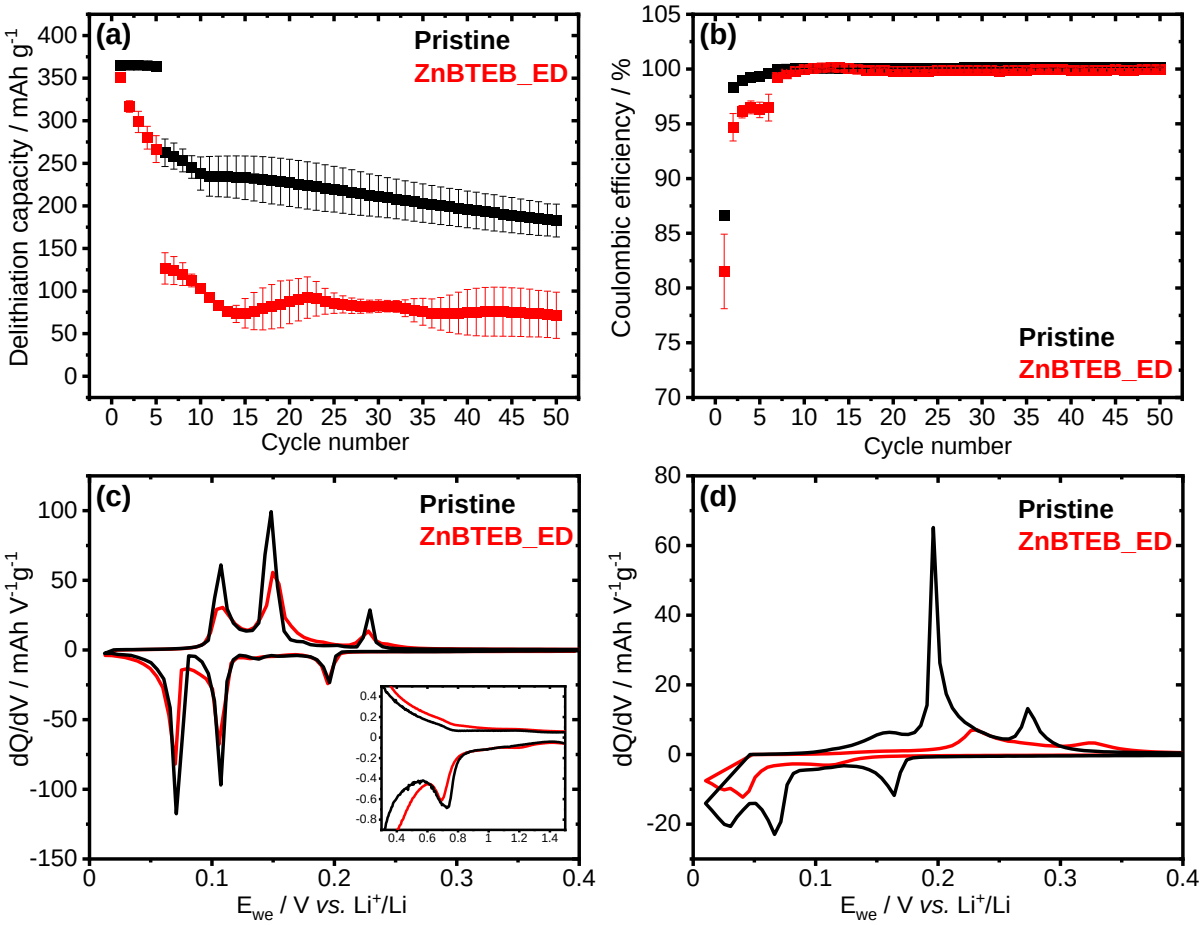

Figure 26. (a) electrochemical cycling stability at C/10 for 5 cycles and 1C for 45 cycles, (b) corresponding Coulombic efficiencies, dQ/dV plots of the first (c) and 10th cycle (d) of pristine and ZnBTEB_ED electrodes.

7.1.3 Synthesis of Zn-BTEB on graphite

Since the formation of ZnBTEB on the graphite electrode *via* electrodeposition could not be confirmed with certainty and the process led to a deterioration of the electrochemical performance of the electrode, an alternative method was investigated. Herein, graphite powder was modified in an upscaled procedure from Chapter 7.1.1 by adding graphite powder to the $Zn(NO_3)_2 \cdot 6H_2O$ and BTEB ligand solution. The most intensive Bragg reflections of ZnBTEB are present in the PXRD of the modified graphite powder (red asterisks in Figure 27a). As the amount of ZnBTEB in the graphite sample is relatively low compared to the amount of graphite, the reflections of ZnBTEB have very small intensities. The effect of the preferred orientation explains the poor visibility of some reflections of ZnBTEB in the graphite sample, which leads to a change in the relative intensities of peaks in the PXRD pattern. No ligand peaks were observed in the Raman spectrum of G-ZnBTEB (Figure S7a). The modified powder was used to prepare graphite electrodes, which were studied by SEM (Figure 27d–c). The pristine graphite electrode shows that the graphite particles are covered by conductive additive. The conductive additive is present in smaller and bigger porous agglomerates at the graphite surface. This is also observed for the ZnBTEB electrode. Unlike the pristine, the modified

electrode additionally shows spherical particles which also tend to agglomerate. Since these particles do not appear on the pristine, it is concluded they derive from the modification with ZnBTEB MOF.

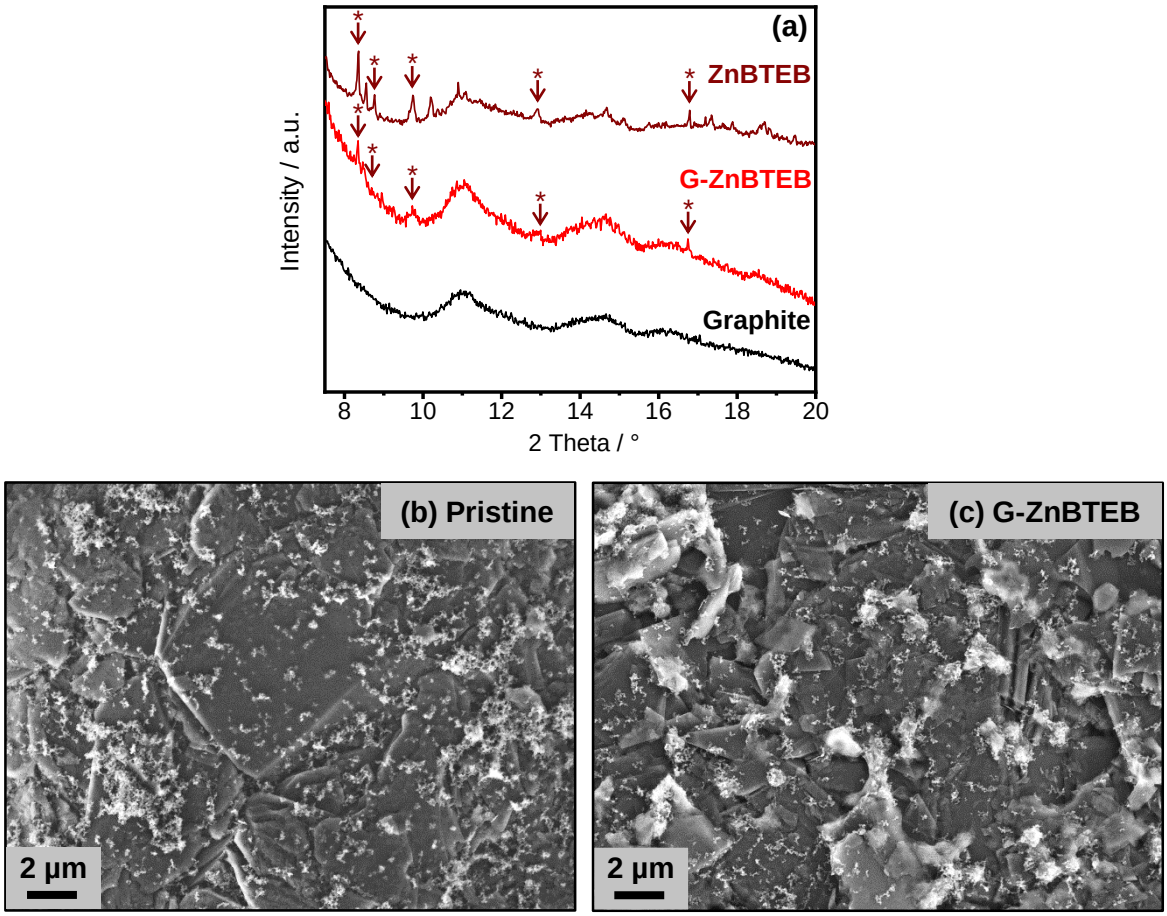

Figure 27. (a) PXRD of the G-ZnBTEB electrode compared to graphite and ZnBTEB ($\lambda = 1.54056$ Å; red asterisks mark the most intensive Bragg reflections of ZnBTEB; amorphous-like background at $10° < 2\theta < 17°$ arises from Kapton film) and SEM images of (b) the pristine graphite and (c) G-ZnBTEB electrode.

The electrochemical performance of the G-ZnBTEB electrode is shown in Figure 28. Although the capacity of G-ZnBTEB seems to slowly decrease at C/10, the capacities only differ by ~1 % from the pristine in the first 5 cycles. At 1C, G-ZnBTEB delivers a capacity of 279 mAh g^{-1} with a retention of 93 %, whereas the pristine only delivers a capacity of 262 mAh g^{-1} with a retention of 70 %. However, the Coulombic efficiency decreased for G-ZnBTEB compared to the pristine. It seems that ZnBTEB delivers no additional capacity at C/10. Since the difference in capacity between pristine and G-ZnBTEB in the first cycle at 1C (≡ 6th cycle) is not tremendous (17 mAh g^{-1}), the presence of the MOF may only enhance the electrode's stability but not its capacity. If no capacity effects derive from the MOF, it is possible that the presence of ZnBTEB leads to an improved SEI. On the other hand, the decreased efficiencies suggest that the SEI formation is not completed during the first 5 cycles at C/10. Even for the following 45 cycles at 1C the efficiencies are decreased compared to the pristine electrode. This indicates that the passivation of the electrode surface is less efficient, but the resulting SEI

components may favour lithium-ion transport. The decrease of the efficiencies of G-ZnBTEB could arise from irreversible decomposition of the ZnBTEB. For instance, Li *et al.*[115] used a Zn-MOF with a similar ligand (1,3,5-benzenetribenzoate, BTB) as active material and suggested irreversible MOF decomposition under formation of Li_2O. Although the electrodes were dried at elevated temperatures under vacuum prior to cell assembly, irreversible decomposition could also result from reactions with guest solvent molecules (here DMF, see formula in Chapter 7.1) as described in [115], [145].

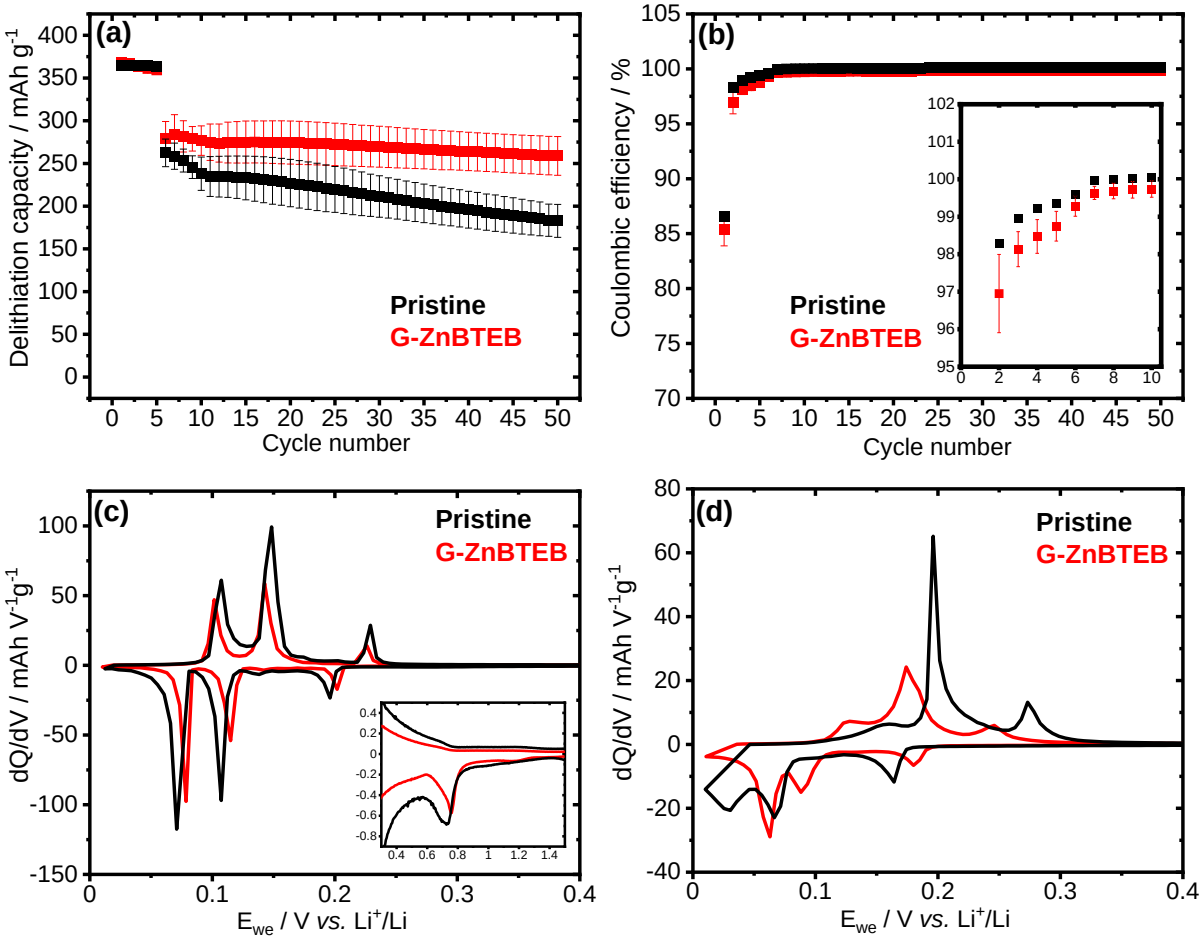

Figure 28. (a) electrochemical cycling stability at C/10 for 5 cycles and 1C for 45 cycles, (b) corresponding Coulombic efficiencies, dQ/dV plots of the first (c) and 10th cycle (d) of pristine and G-ZnBTEB electrodes.

The differential capacity plot of the first cycle shows the presence of the EC reduction peak at ~0.8 V *vs.* Li^+/Li for the pristine and the G-ZnBTEB electrode (Figure 28c inset). The peak of the G-ZnBTEB electrode is sharper and slightly shifted to higher potentials compared to the pristine, suggesting a favoured electrolyte reduction. The lithiation/delithiation peaks are shifted to higher/lower potentials, respectively, advocating better lithium-ion diffusion for G-ZnBTEB (Figure 28c). This effect is even more visible in the 10th cycle (Figure 28d). MOFs are described to create large electrode/electrolyte interfaces and short lithium-ion diffusion pathways, due to their large surface area and high porosity.[107] However, as discussed in Chapter 3, literature reports different behaviour for MOFs in batteries (for instance, the

possibility of retaining or decomposition of the MOF structure during cycling). Therefore, it is not clear if the enhanced lithium-ion transport results from advantageous properties ascribed to the MOF or advantageous decomposition products from SEI formation.

7.1.4 Carbonisation of Zn-BTEB on graphite

As a second step, the ZnBTEB graphite powder was carbonised at 500 °C for 4 h according to TGA experiments from Zhu *et al*.[66] The reflections derived from ZnBTEB MOF are no longer visible in the PXRD (Figure 29a–b). Instead, new reflections appear in the diffractogram, corresponding to hexagonal ZnO with wurtzite structure and the space group $P6_3mc$ (Figure 29a,c). The powder was used to prepare electrodes, which were studied by SEM (Figure 29d–e). The conductive additive is still visible on the graphite surface, but the spherical particles seem to have disappeared. Instead, the graphite surface appears to be coated by what is ascribed to be a carbon matrix derived by the carbonisation of the MOF. A closer look reveals another component being present on the electrode's surface (Figure 29e). It is assumed the small white particles to be ZnO, which is supported by an additional SEM image using an EsB detector (Figure S8). The EsB detector is able to distinguish between heavy and less heavy atoms, by displaying them lighter and darker, respectively. The white particles clearly correspond to a heavier atom (Zn) than the surrounding parts of the electrode (C). PXRD and SEM give reason to assume successful carbonisation of ZnBTEB MOF on the graphite electrode, resulting in a porous carbon matrix and ZnO particles on the electrode surface, which will be referred to as G-ZnBTEB_C in the following.

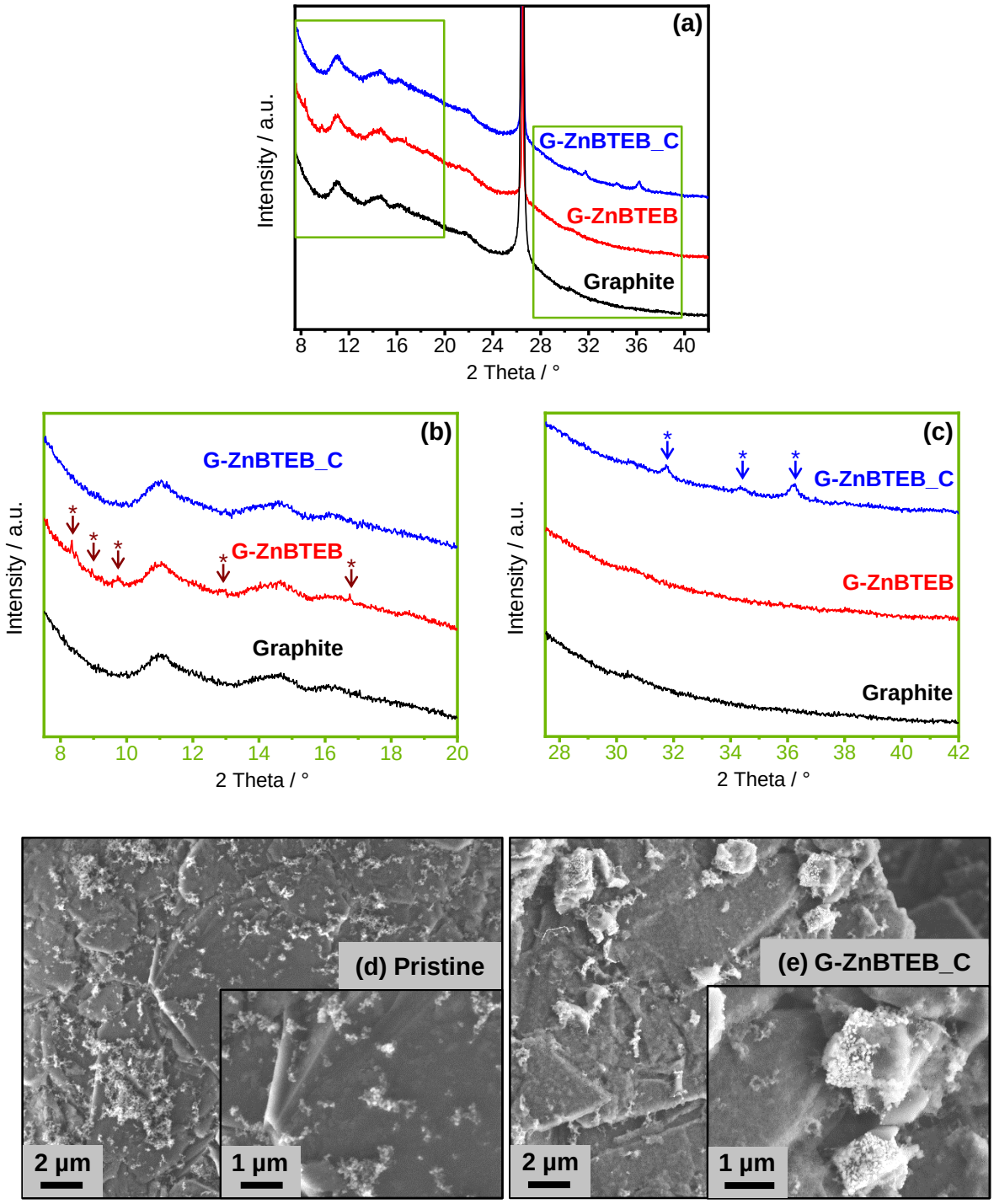

Figure 29. (a) PXRD (λ = 1.54056 Å) of the G-ZnBTEB_C electrode compared to graphite and G-ZnBTEB with zooms in the (b) 7.5 – 20 ° (red asterisks mark the most intensive Bragg reflections of ZnBTEB; amorphous-like background at 10 ° < 2θ < 17 ° arises from Kapton film) and (c) 27.5 – 40 ° (blue asterisks mark Bragg reflections of ZnO according to [146]) regions and SEM images of (d) the pristine graphite and (e) G-ZnBTEB_C electrode.

The electrochemical performance of the G-ZnBTEB_C electrodes is shown in Figure 30. The capacity of G-ZnBTEB_C seems to slowly decrease at C/10 as well, however, the values are slightly improved compared to the G-ZnBTEB and the pristine electrode (Figure 30a). At 1C,

G-ZnBTEB_C delivers a capacity of 271 mAh g^{-1} with a retention of 81 %. Although, the stability at 1C is enhanced compared to the pristine electrode, the stability decreased compared to G-ZnBTEB. The Coulombic efficiency at C/10 decreased for G-ZnBTEB_C as well, compared to the pristine electrode. Although, the efficiency from 7th to 50th cycle is enhanced compared to G-ZnBTEB, it is still decreased compared to the pristine, indicating more irreversible side reactions taking place. PXRD already showed that the ZnBTEB reflexes disappeared after carbonisation (Figure 29b). Furthermore, it can be assumed that after carbonisation no solvent guest molecules are left in G-ZnBTEB_C. Consequently, the low efficiency at C/10 cannot be ascribed to irreversible ZnBTEB decomposition nor solvent decomposition. This may be a reason why, G-ZnBTEB_C has higher efficiencies at 1C compared to G-ZnBTEB. Most literature on carbonised MOFs attributes high irreversible capacity losses simply to "SEI formation" and incomplete conversion reactions of ZnO.[118], [119], [147], [148]

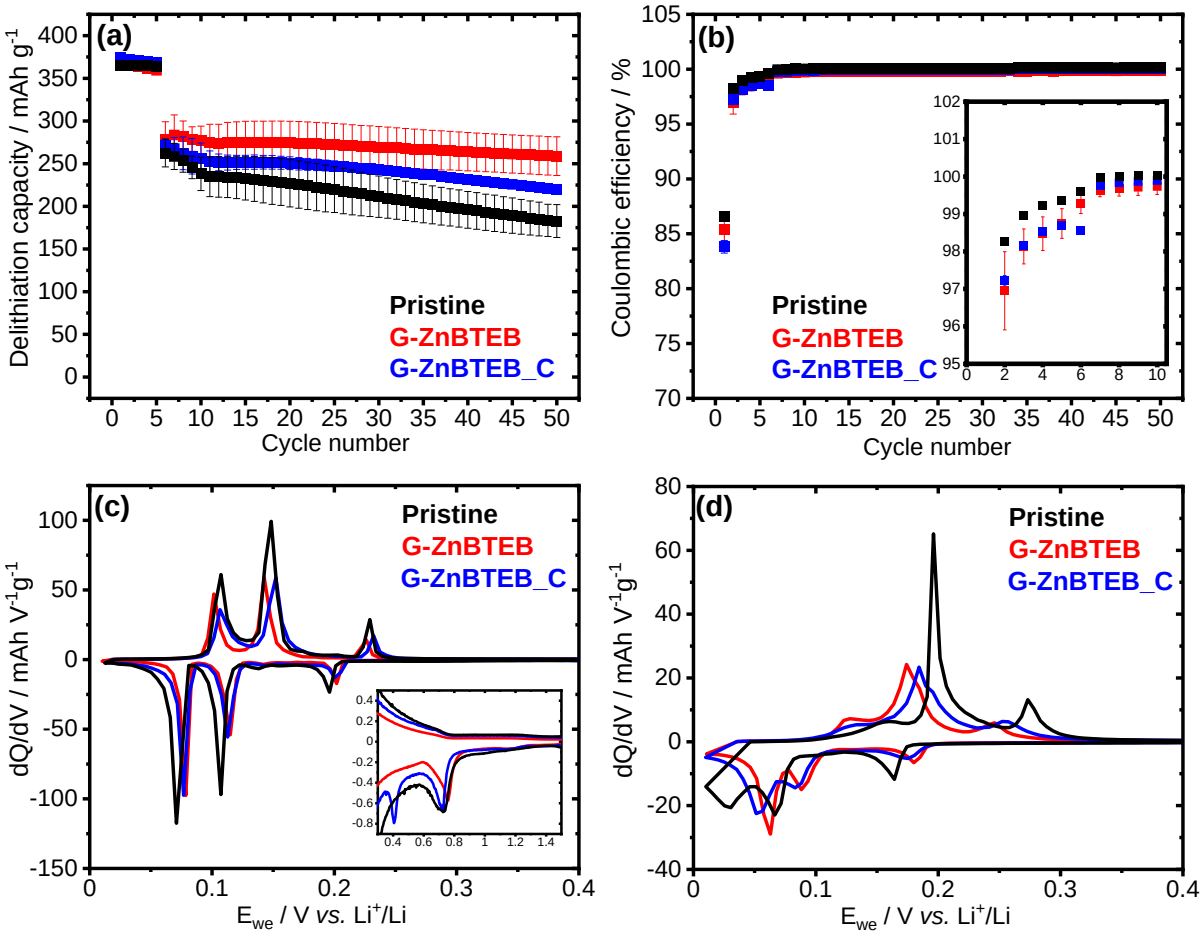

Figure 30. (a) electrochemical cycling stability at C/10 for 5 cycles and 1C for 45 cycles, (b) corresponding Coulombic efficiencies, dQ/dV plots of the first (c) and 10th cycle (d) of pristine, G-ZnBTEB and ZnBTEB_C electrodes.

The differential capacity plot of the first cycle shows that EC is reduced at the same potential as the pristine electrode (Figure 30c inset). It is noticeable, that an additional sharp peak at

~0.4 V *vs.* Li^+/Li is present for ZnBTEB_C during reduction, but no corresponding oxidation peak, indicating the peak derives from irreversible reduction reactions. Song *et al.*[118] and Fu *et al.*[119] report the irreversible reduction of ZnO at ~0.75 V *vs.* Li^+/Li in the first cycle. Huang *et al.*[149] found a strong reduction peak at 0.34 V *vs.* Li^+/Li in the first cycle, which is also attributed to the reduction of ZnO and additionally to the formation of the SEI and a Li-Zn alloy. The varying reported peak position may be ascribed to the different synthesis techniques to prepare ZnO materials. The synthesis procedure in this work also differs from the cited literature. The irreversible peak at ~0.4 V *vs.* Li^+/Li from Figure 30 lies within the literature reported range of 0.34 – 0.75 V *vs.* Li^+/Li and hence, may also be attributed to irreversible reduction of ZnO.

However, additional experiments would be necessary to determine the origin of the additional peak at ~0.4 V *vs.* Li^+/Li. The intercalation peaks in the first cycle are shifted to higher potentials compared to the pristine, similar to ZnBTEB. At the 10^{th} cycle intercalation/deintercalation peaks are shifted to higher/lower potentials, respectively, compared to the pristine electrode. However, they are shifted less compared to ZnBTEB, indicating the lithium-ion diffusion is enhanced compared to the pristine but decreased compared to ZnBTEB. It can be assumed that the surface composition of G-ZnBTEB differs from the one of G-ZnBTEB_C due to the carbonisation step, which is supported by PXRD and SEM (Figure 29). The results from Figure 30 show that the cycling stability at 1C and the lithium-ion transport are superior to the pristine electrode but worse than G-ZnBTEB. Whether the ZnO/C surface layer or resulting SEI components or both are responsible needs to be elucidated with additional experiments.

7.2 Zn-TAP and carbonised Zn-TAP

7.2.1 Synthesis of Zn-TAP

On basis of a procedure by O'Doherty (not published) $Zn(NO_3)_2$ and TAP ligand were heated in a 2:1 molar ratio in DMF at 70 °C for 2 days. The PXRD patterns of ZnTAP do not show sharp reflections, indicating poor crystallinity and only a short-range structural order (Figure 31a). However, Raman spectroscopy gives additional information about the modified sample. The characteristic Raman peaks of TAP for CH_2 rocking vibration at 988 cm^{-1}, triazine at 1018 cm^{-1} C-C single bond vibrations at 1125, 1143 and 1177 cm^{-1}, aromatic C=C vibration at 1610 cm^{-1} and C≡C alkyne vibration at 2220 cm^{-1} are displayed in Figure 31b. The corresponding peaks in ZnTAP are found at 988 cm^{-1}, 1016, 1131 and 1176 cm^{-1}, 1608 cm^{-1} and 2214 cm^{-1}, respectively. Optical microscopy shows needles of Zn-TAP (Figure 31c). It is not clear, which compound formed during the synthesis, nevertheless, the synthesis procedure is used for Chapter 7.2.3.

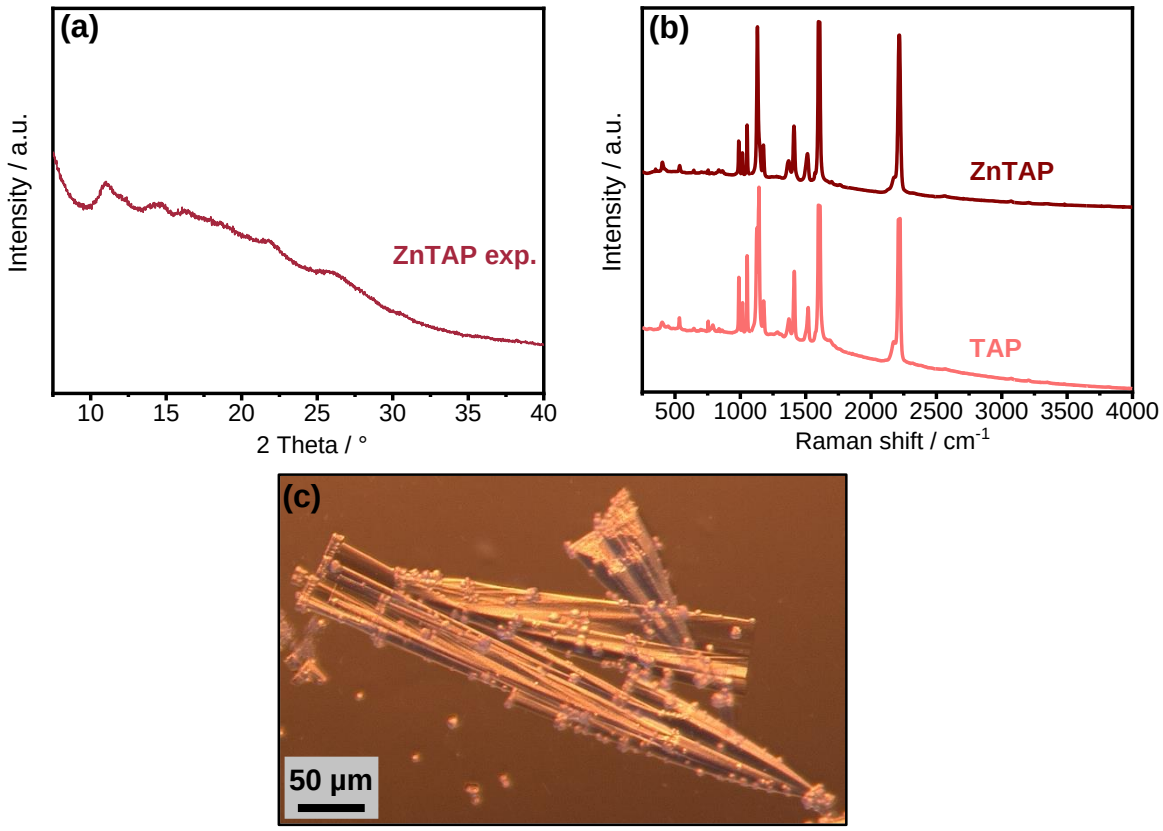

Figure 31. (a) PXRD pattern of ZnTAP synthesised crystals (λ = 1.54056 Å; amorphous-like background at 10 ° < 2θ < 17 ° arises from Kapton film), (b) Raman spectra of TAP ligand and synthesised ZnTAP crystals and (c) optical microscope image of synthesised ZnTAP crystals.

7.2.2 Electrodeposition of Zn-TAP

The experiments concerning the electrodeposition of ZnTAP were carried out analogue to Chapter 7.1.2. It was observed that the solvent mixture could not completely dissolve the TAP ligand. After one day, the already dissolved ligand precipitated from the solution, which was not observed for BTEB. Therefore, the TAP and Zn salt containing electrolyte was heated to 90 °C, but even after heating the TAP and $Zn(NO_3)_2$ containing electrolyte to 90 °C no homogeneous solution could be obtained. The remaining precipitate was filtered off the electrolyte solutions, which were used for electrodeposition experiments on FTO. No films were received at –1.4 V for 10 min. The potential was varied between –1.2 V and –1.5 V *vs.* Ag(cryptand)$^+$/Ag but no films resulted at these potentials. Due to limited time and availability of TAP, no further attempts could be made to electrodeposit Zn-TAP on FTO or graphite.

7.2.3 Synthesis of Zn-TAP on graphite

Analogue to Chapter 7.1.3, graphite powder was modified in an upscaled procedure from Chapter 7.2.1 by adding graphite powder to the $Zn(NO_3)_2 \cdot 6H_2O$ and TAP ligand solution. No reflections of G-ZnTAP were detected in the PXRD of modified graphite powder (Figure 32a). Since the TAP ligand is larger than the BTEB ligand, it is possible that its Bragg reflections are

even less intensive or superimposed by the graphite reflections. Another possibility is the formation of amorphous coordination networks, which would not be visible in PXRD.[150] Nevertheless, the C≡C alkyne vibration at 2211 cm^{-1} in the Raman spectrum of G-ZnTAP indicates the presence of TAP ligand on the modified sample (Figure S7b). Regardless, the modified powder was used to prepare graphite electrodes, which were studied by SEM (Figure 32b–c). Similar to the G-ZnBTEB electrode, spherical particles are observed on the surface of ZnTAP as well, indicating the presence of an additional component on the electrode surface. For the sake of clarity, the modified electrode is labelled as G-ZnTAP.

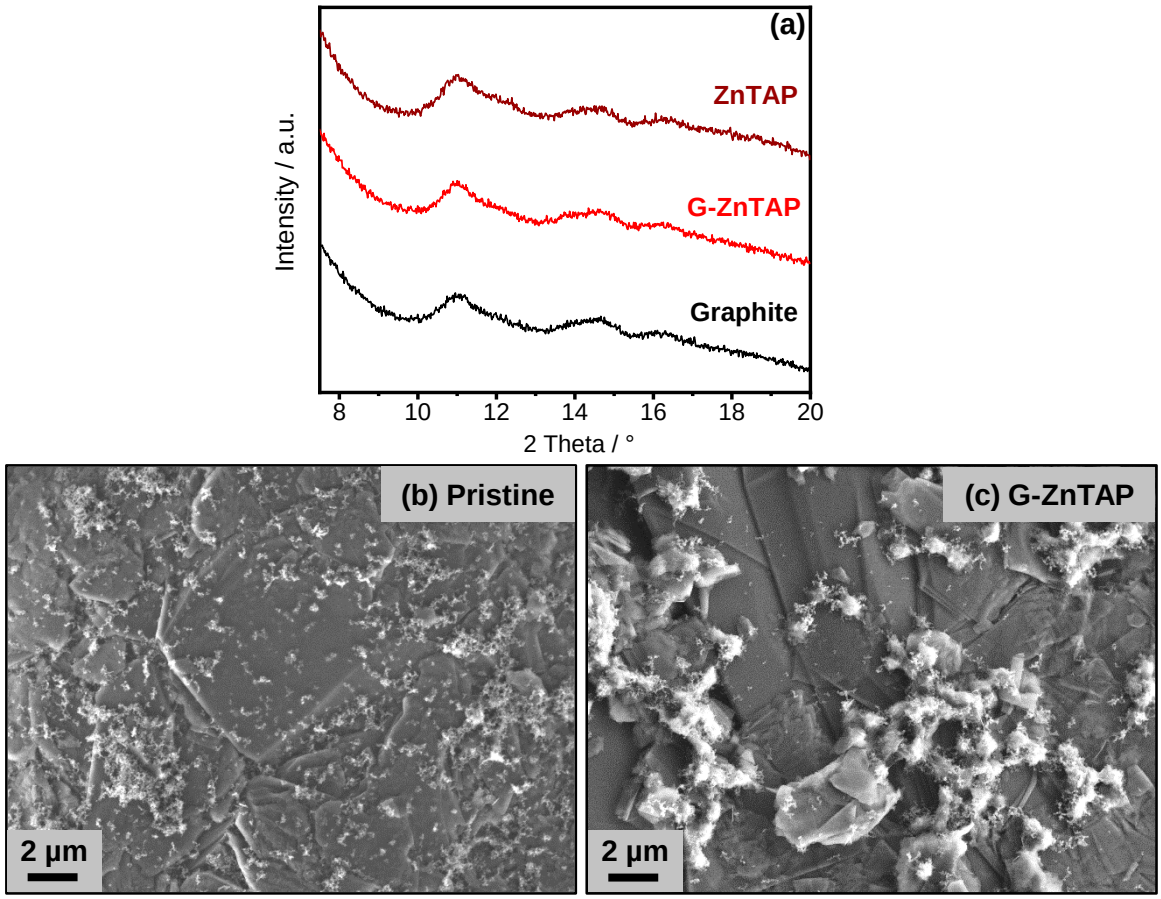

Figure 32. (a) PXRD of the G-ZnTAP electrode compared to graphite and ZnTAP (λ = 1.54056 Å; amorphous-like background at 10 ° < 2θ < 17 ° arises from Kapton film) and SEM images of (b) the pristine graphite and (c) G-ZnTAP electrodes.

The electrochemical performance of the G-ZnTAP electrode is shown in Figure 33. The capacity of G-ZnTAP at C/10 is very similar to the pristine electrode (+ 1–3 mAh g^{-1}). In the first cycle, G-ZnTAP delivers additional 5 mAh g^{-1} capacity. However, at 1C the capacity decreased to 237 mAh g^{-1} with a retention of 65 % compared to the reference with 262 mAh g^{-1} and a retention of 70 %. Even though the Coulombic efficiency slightly increased in the first cycle indicating less irreversible side reactions, it decreased for all following cycles at C/10 and 1C compared to the pristine, indicating more irreversible side reactions compared to the pristine. Nevertheless, the difference in Coulombic efficiencies between G-ZnTAP and the pristine is not tremendous. In Chapter 7.1.3 additional irreversible reactions with solvent guest

molecules are described. Assuming an amorphous compound, the amount of solvent could be much less compared to a crystalline MOF and hence not noticeably increases irreversible side reactions. The same is applicable to the MOF decomposition reactions assumed in Chapter 7.1.3. It is also possible that the amount of ZnTAP is too low to cause remarkable changes in cycling stability and efficiency.

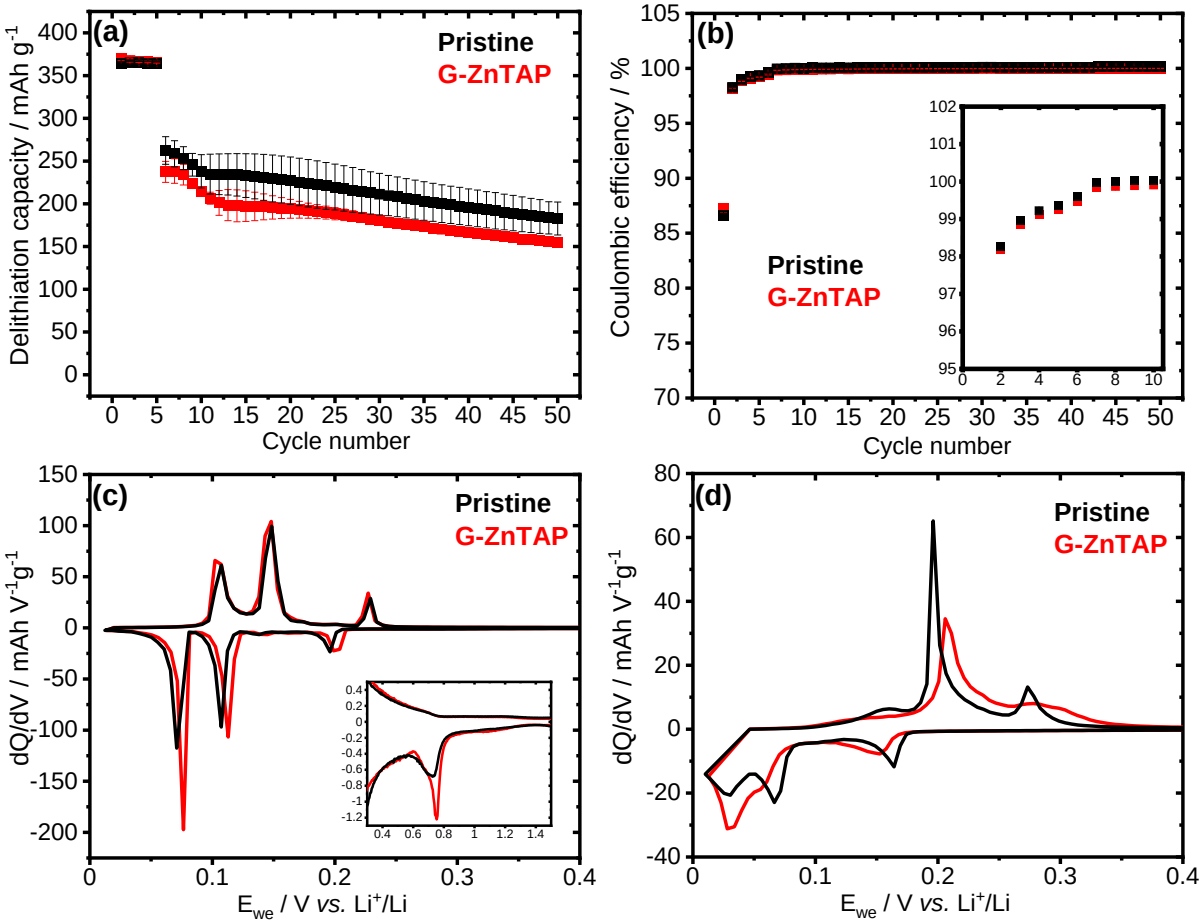

Figure 33. (a) electrochemical cycling stability at C/10 for 5 cycles and 1C for 45 cycles, (b) corresponding Coulombic efficiencies, dQ/dV plots of the first (c) and 10th cycle (d) of pristine and G-ZnTAP electrodes.

The differential capacity plot of G-ZnTAP in the first cycle shows that EC is reduced at the same potential as the pristine electrode. However, the peak is more intense and sharp, indicating favoured electrolyte reduction. The intercalation peaks of G-ZnTAP are slightly shifted to higher potentials, possibly due to better lithium-ion transport. However, in the 10th cycle the intercalation/deintercalation peaks are slightly shifted to lower/higher potentials compared to the pristine, assuming deteriorated lithium-ion transport. The uncertainty about the structure and composition of G-ZnTAP makes it difficult to explain the effects from Figure 33.

7.2.4 Carbonisation of Zn-TAP on graphite

Analogue to Chapter 7.1.4, the ZnTAP graphite powder was carbonised at 500 °C for 4h according to TGA experiments of O'Doherty (not published). The reflections in the PXRD of G-

ZnTAP corresponding to hexagonal ZnO with wurtzite structure and the space group $P6_3mc$ are present, albeit the intensity is lower compared to G-ZnBTEB (Figure 34c). The presence of ZnO on G-ZnTAP_C proves that it was not solely TAP ligand present on G-ZnTAP, but also Zn-containing species (Figure 34a–c). The powder was used to prepare electrodes, which were studied by SEM (Figure 34d–e). Similar to the corresponding G-ZnBTEB_C electrode, the coating ascribed to the carbon matrix is also visible in the G-ZnTAP_C electrode.

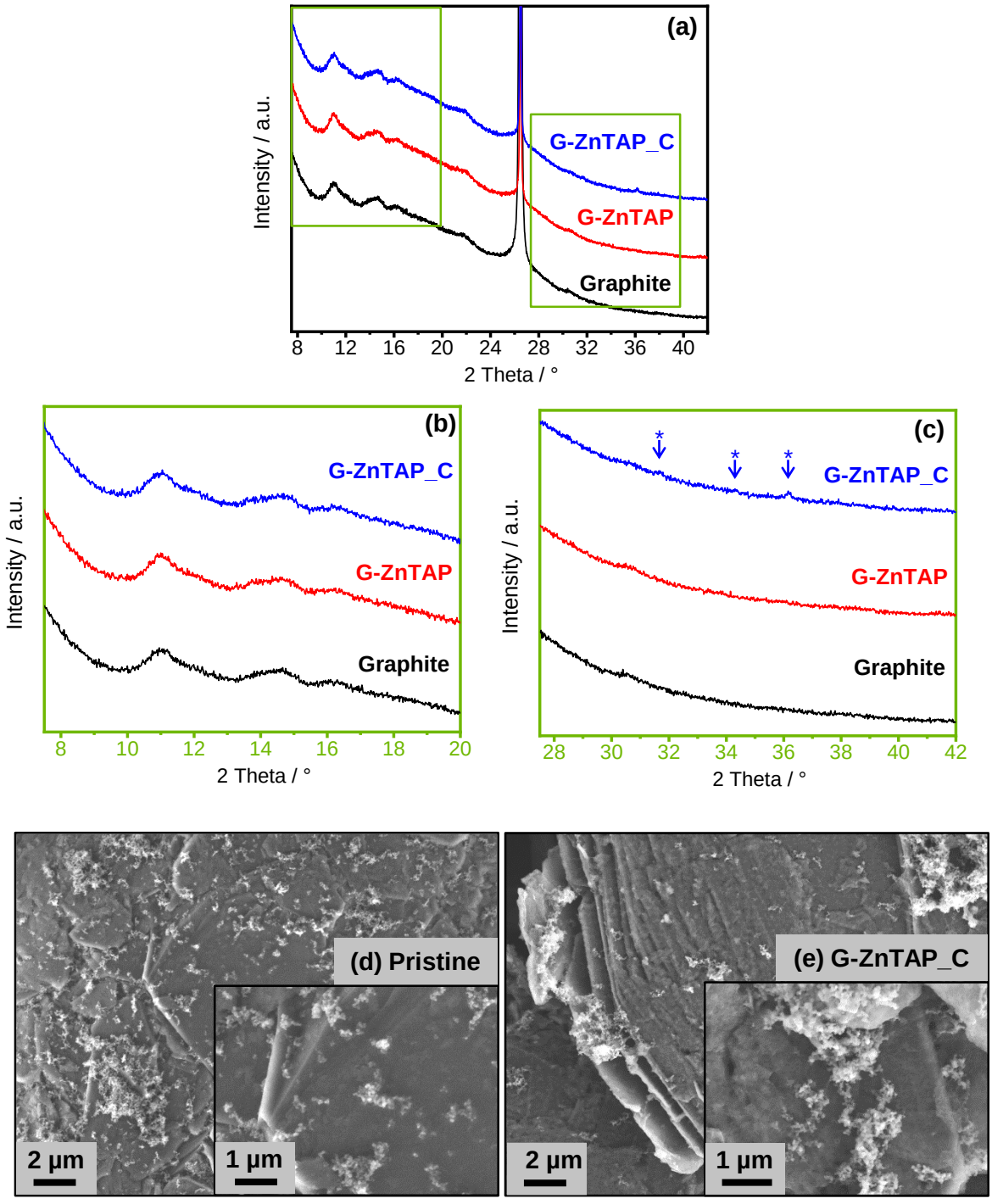

Figure 34. (a) PXRD (λ = 1.54056 Å) of the G-ZnTAP_C electrode compared to graphite and G-ZnTAP with zooms in the (b) 7.5 – 20 ° (amorphous-like background at 10 ° < 2θ < 17 ° arises from Kapton film) and (c) 27.5 – 40 ° (blue asterisks mark Bragg reflections of ZnO

according to [146]) regions and SEM images of (d) the pristine graphite and (e) G-ZnTAP_C electrode.

The electrochemical performance of G-ZnTAP_C is shown in Figure 35. The delithiation capacities at C/10 are similar to G-ZnTAP and the pristine electrode, but at 1C, the capacity is visibly higher compared to G-ZnTAP. Compared to the pristine with 262 mAh g^{-1} and a retention of 70 %, G-ZnTAP delivers 279 mAh g^{-1} with a retention of 87 %. However, the Coulombic efficiency dropped, indicating more side reactions for G-ZnTAP. As already mentioned in Chapter 7.1.4, the literature on carbonised MOFs attributes high irreversible capacity losses to SEI formation and incomplete conversion reactions of ZnO. [118], [119], [147], [148] Since PXRD proved the presence of ZnO, the incomplete conversion reactions as reason for decreased efficiency are also applicable for G-ZnTAP_C.

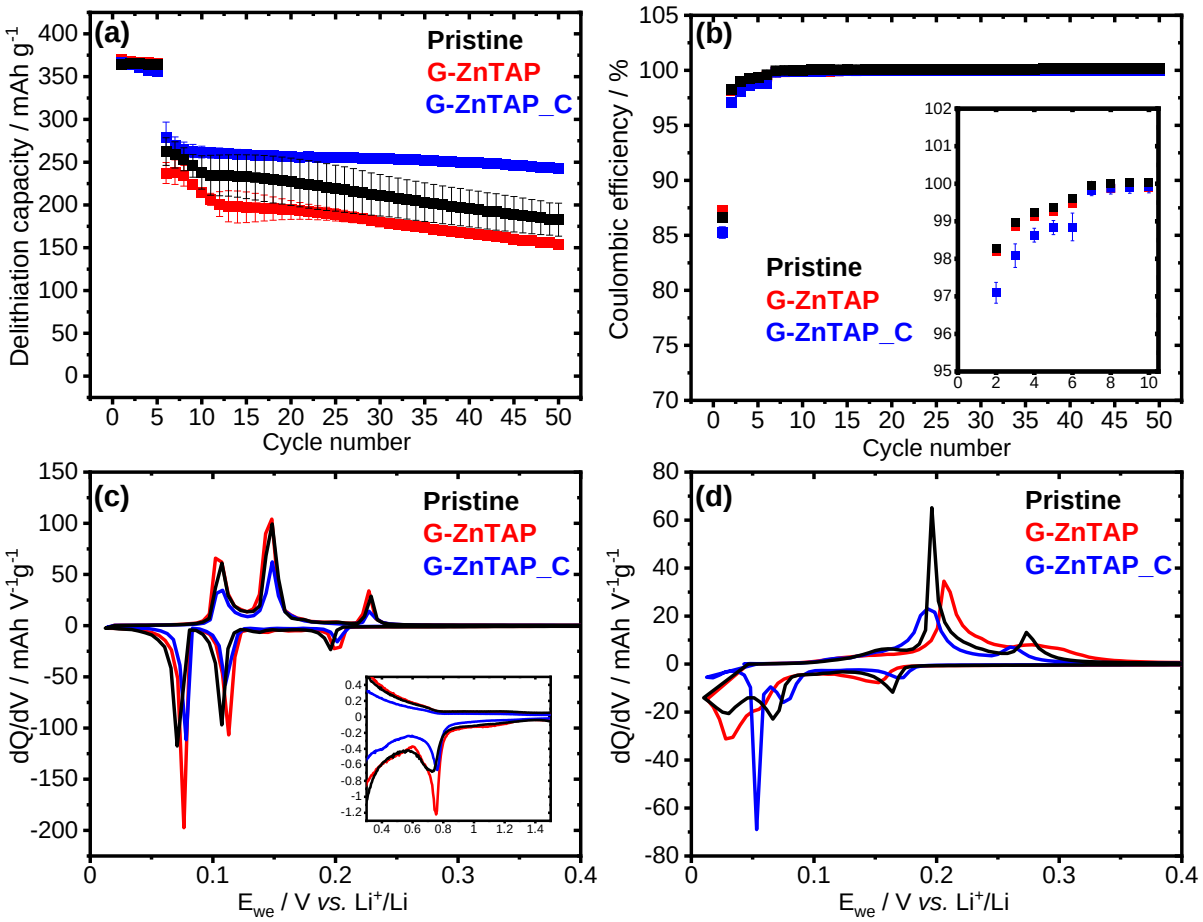

Figure 35. (a) electrochemical cycling stability at C/10 for 5 cycles and 1C for 45 cycles, (b) corresponding Coulombic efficiencies, dQ/dV plots of the first (c) and 10th cycle (d) of pristine, G-ZnTAP and G-ZnTAP_C electrodes.

Differential capacity plots show, that in the first cycle the peaks did not shift compared to G-ZnTAP. Unlike for G-ZnBTEB_C, no additional irreversible reduction peak is observed at 0.4 V *vs.* Li^+/Li. The reflections of ZnO in G-ZnTAP_C (Figure 34c) are not very intense and less distinct than in G-BTEB_C (Figure 29c), indicating that the amount of ZnO in G-ZnTAP_C

is too low to give a fingerprint in the dQ/dV plots. It is noticeable that in the 10th cycle the intercalation peak at ~0.05 V *vs.* Li^+/Li is very sharp and intense compared to G-ZnTAP and the pristine electrode, indicating enhanced lithium-ion transport for G-ZnTAP_C.

G-ZnTAP_C shows a better cycling stability compared to G-ZnBTEB_C. As already mentioned, this could be due to the lower amount of ZnO. However, since the information about the composition of G-ZnTAP is not sufficient, an explanation without further experiments is difficult. Another aspect that needs to be considered, is that the nitrogen-content of the TAP ligand could impact the chemical composition of the carbon matrix after carbonisation.

7.3 Conclusive aspects

Two different Zn-containing MOFs were investigated to modify graphite electrodes. The used ligands were commercially available BTEB and a new ligand (not published yet) with a triazine core (TAP). Electrodeposition of ZnBTEB and ZnTAP was studied. Although, the PXRD analysis did not prove the formation of ZnBTEB on the graphite electrode, Raman spectroscopy confirmed the presence of the ligand on the electrode and SEM images showed a network-like structure on the electrode's surface. However, the capacity and Coulombic efficiency were deteriorated by the modification process. It is assumed that the thick layers arising from the modification may lead to decomposition products that deteriorate the lithium-ion transport. This effect intensifies over cycling, especially at 1C. The electrodeposition of ZnTAP was not successful on the model substrate FTO, hence no films could be achieved on graphite electrodes using the TAP ligand *via* electrodeposition. The low solubility of the ligand in the electrolyte may play a role, but the final reason for the unsuccessful modification could not be evaluated yet.

In another approach solvothermal crystallisation of the MOFs was carried out in the presence of graphite powder. PXRD revealed the successful crystallisation of ZnBTEB in the G-ZnBTEB sample. Even though the Coulombic efficiency decreased for the resulting electrodes, the cycling stability was improved at 1C compared to the pristine electrode. The product of the solvothermal synthesis with TAP could not be identified and may be an amorphous coordination compound. The capacities and efficiencies are slightly lower for G-ZnTAP compared to the pristine electrode.

Additionally, the graphite powder with ZnBTEB was carbonised and used as electrode material as well. PXRD and SEM proved the disappearance of ZnBTEB MOF and the formation of ZnO. The electrochemical performance showed lower capacities compared to G-ZnBTEB but higher capacities compared to the pristine. The efficiencies are comparable to G-ZnBTEB. Due to its limitations, PXRD could not prove the presence of ZnTAP on graphite, however the formation of ZnO after carbonisation is clearly distinguishable. G-ZnTAP did not seem to have a significant impact on the electrochemical performance. However, after carbonisation the

ZnTAP_C electrode showed a remarkable increase of the cycling stability. Both carbonised samples (ZnBTEB_C and ZnTAP_C) suffered from a decrease in Coulombic efficiency, which could arise from SEI formation and incomplete conversion reactions with Zn.
For a deeper understanding of the underlying mechanism, additional experimental work is needed.

8. Conclusion

Graphite electrodes for lithium-ion batteries (LIBs) are a famous target for surface modification. The intention is to improve the electrode-electrolyte interface towards electrolyte decomposition and the formation of the solid-electrolyte interphase (SEI) on the graphite electrode. Hereby, it is advantageous to create surface coatings with defined functionalities. This work elaborated chemical and electrochemical surface modification of graphite using aryl diazonium salts (ADS), pyrenes and Zn-based metal-organic frameworks (MOFs).

ADS modification enabled covalent bonds with graphite and functional groups orientated perpendicular to the graphite surface. Electrografting of aryl diazonium salts on graphite electrodes showed that additional subsequent steps like deprotection of ethynyl moieties can affect the binder and deteriorate the electrochemical performance. Furthermore, electrografting can lead to dense multilayers and the resulting SEI hampers lithium-ion transport, especially at higher current densities. *In situ* grafting showed better electrochemical performances with ethynyl, carboxy and nitro moieties compared to the electrografted analogues. The ethynyl sample even showed a slightly improved cycling stability at higher current densities. However, the decrease of Coulombic efficiencies in both methods indicates increased irreversible decomposition reactions.

Pyrenes were used in a non-covalent alternative modification method, where they are adsorbed to the graphite surface. It was found that samples with carboxy groups show superior cycling performance compared to samples with amino groups. Furthermore, a butyl group between the functional group and the pyrene moiety has a positive influence on the cycling performance compared to analogues without butyl group. Pyrene with a butylcarboxy group could enhance the cycling stability compared to a pristine graphite electrode. Hereby, the interaction of pyrenes with the graphite surface is of vital importance to achieve enhanced performances, as pyrenes as electrode additive could not enhance the cycling stability at high current densities.

Finally, Zn-based MOFs were investigated as surface modification for graphite electrodes. Electrodeposition of ZnBTEB achieved a surface coating, but a direct proof of the presence of ZnBTEB *via* XRD was not possible. The cycling performance visibly deteriorated for the ZnBTEB_ED sample, also the Coulombic efficiencies at low current densities are reduced, which was attributed to thick layers arising from electrodeposition. In another attempt *via* solvothermal synthesis of Zn-MOFs in the presence of graphite, G-ZnBTEB could enhance the cycling stability compared to the pristine graphite electrode. The composition of G-ZnTAP remained unclear, although the presence of ligand and Zn species could be shown. However, it is assumed that the amount of ZnTAP is very low and there was no significant change in

cycling stability and Coulombic efficiency. Furthermore, both modified graphite powders were carbonised as a second step and tested as electrodes. G-ZnBTEB_C and G-ZnTAP_C both achieved enhanced cycling stability compared to the pristine graphite electrode, but also decreased Coulombic efficiencies. The underlying mechanisms are not clear, as additional experiments are needed for a deeper understanding.

In Chapter 5 and 6, carboxy and amino moieties were used as functional groups. In both chapters, the carboxy groups show superior cycling stability compared to amino groups. A possible explanation is that carboxy groups are reducible and could act as nucleation sites for SEI formation. Comparing the anchor molecules, carboxy groups on pyrene showed superior cycling performance to carboxy groups on aryl diazonium salts. This may be associated with the different anchoring to the graphite surface (covalent modification disrupts the aromatic system of graphite and may reduce conductivty) as well as the orientation of the functional group. As already mentioned, pyrene with a butylcarboxy group performs better than “only” a carboxy group, which may be due to a better accessibility for SEI formation. However, the best cycling performance of all modified electrodes was achieved with G-ZnBTEB, which also contains carboxy groups. The mechanistic influence of carboxy groups in G-ZnBTEB could not be extracted from the available data.

In summary, the modification of graphite electrodes with ADS, pyrenes and Zn-based MOFs can enhance the cycling performance of graphite electrodes. Hereby, the combination of suitable modification methods and functional groups is of importance. In general, electroless modification methods achieved better performances of the according electrodes. It is assumed, that this may be related to thicker resulting layers.

9. Outlook

The focus of this thesis was modification of graphite electrodes with different material classes and functionalities and their electrochemical behaviour as electrodes in LIBs. It is possible to describe trends between the different approaches and how cycling stability, Coulombic efficiency and lithium-ion transport is affected. However, detailed underlying mechanisms were not evaluated in this work. Additional measurements, for instance electrochemical impedance spectroscopy or XPS and SEM of cycled electrodes, could help to get a deeper understanding. A comparative study of all carboxy-containing samples with these techniques could enable an elaboration of the influence on the electrochemical behaviour of the different samples. In addition, the electrochemical behaviour of pristine ZnBTEB and ZnTAP was not investigated and analysed after cycling. This would help to distinguish between electrochemical reactions of MOF and graphite.

Furthermore, a combination of the presented methods could further improve the electrochemical behaviour of graphite electrodes. For example, a graphite electrode could be functionalised with butylcarboxy-containing pyrenes to improve (or enable) crystallisation of Zn-MOFs. Ethynyl anchor groups could be used for further layer growth with azides or *via* thiol-yne or amino-yne Click chemistry and be studied as artificial SEI.

The presented modification procedures are also applicable to other carbonaceous materials, *e.g.* graphene and carbon nanotubes (CNTs). Furthermore, post-lithium-ion battery research resort to carbon materials, where the electrode-electrolyte interface is of importance as well.[151], [152] Therefore, the methods of this work could be useful for other systems, like post-lithium-ion batteries.

References

[1] G. Crabtree, E. Kócs, and L. Trahey, *MRS Bull.* **2015**, *40*, 1067–1078.

[2] J. Asenbauer, T. Eisenmann, M. Kuenzel, A. Kazzazi, Z. Chen, and D. Bresser, *Sustain. Energy Fuels* **2020**, 5387–5416.

[3] P. V. Kamat, *ACS Energy Lett.* **2019**, *4*, 2757–2759.

[4] Y. Liang, C.-Z. Zhao, H. Yuan, Y. Chen, W. Zhang, J.-Q. Huang, D. Yu, Y. Liu, M.-M. Titirici, Y.-L. Chueh, H. Yu, and Q. Zhang, *InfoMat.* **2019**, *1*, 6–32.

[5] H. Zhang, Y. Yang, D. Ren, L. Wang, and X. He, *Energy Storage Mater.* **2021**, *36*, 147–170.

[6] W. Qi, J. G. Shapter, Q. Wu, T. Yin, G. Gao, and D. Cui, *J. Mater. Chem. A* **2017**, *5*, 19521–19540.

[7] P. Verma, P. Maire, and P. Novák, *Electrochim. Acta* **2010**, *55*, 6332–6341.

[8] K. Vuorilehto, in *Handbuch Lithium-Ionen Batterien*, R. Korthauer, Ed. Springer Verlag, Berlin Heidelberg, **2013**, 21–30.

[9] P. Bieker and M. Winter, *Chem. Unserer Zeit* **2016**, *50*, 26–33.

[10] J. Lee, P. Srimuk, S. Fleischmann, X. Su, T. A. Hatton, and V. Presser, *Prog. Mater. Sci.* **2019**, *101*, 46–89.

[11] K.-C. Möller, in *Handbuch Lithium-Ionen Batterien*, R. Korthauer, Ed. Springer Verlag, Berlin Heidelberg, **2013**, 3–12.

[12] K. Xu, *Chem. Rev.* **2004**, *104*, 4303–4417.

[13] D. Wieboldt, M. Hahn, and I. Ruff, *Spectroscopy Supplements* **2015**, *30*.

[14] C. Hanisch, J. Diekmann, A. Stieger, W. Haselrieder, and A. Kwade, in *Handbook of Clean Energy Systems, Vol. 5*, J. Yan, Ed. Wiley, UK, **2015**, 2865–2888.

[15] V. Etacheri, R. Marom, R. Elazari, G. Salitra, and D. Aurbach, *Energy Environ. Sci.* **2011**, *4*, 3243–3262.

[16] B. Scrosati, *J. Electrochem. Soc.* **1992**, *139*, 2776–2781.

[17] Y. Yuan, K. Amine, J. Lu, and R. Shahbazian-Yassar, *Nat. Commun.* **2017**, *8*, 15806.

[18] S. Fang, D. Bresser, and S. Passerini, *Adv. Energy Mater.* **2020**, *10*, 1902485.

[19] J. Xiao, Q. Li, Y. Bi, M. Cai, B. Dunn, T. Glossmann, J. Liu, T. Osaka, R. Sugiura, B. Wu, J. Yang, J.-G. Zhang, and M. S. Whittingham, *Nat. Energy* **2020**, *5*, 561–568.

[20] M. Winter, J. O. Besenhard, M. E. Spahr, and P. Novák, *Adv. Mater.* **1998**, *10*, 725–763.

[21] R. Liu, Y. Chi, L. Fang, Z. Tang, and X. Yi, *J. Nanosci. Nanotechnol.* **2014**, *14*, 1647–1657.

[22] U. Hofmann and W. Rüdorff, *Trans. Faraday Soc.* **1938**, *34*, 1017–1021.

[23] N. Daumas and A. Hérold, *Comptes Rendus Acad. Sci. Ser. C* **1969**, *268*, 373–375.

[24] E. R. White, J. J. Lodico, and B. C. Regan, *Nat. Commun.* **2017**, *8*, 1969.

[25] J. R. Dahn, *Phys. Rev. B* **1991**, *44*, 9170–9177.

[26] A. Manthiram, *ACS Cent. Sci.* **2017**, *3*, 1063–1069.

[27] J. Asenbauer, M. Kuenzel, T. Eisenmann, A. Birrozzi, J.-K. Chang, S. Passerini, and D. Bresser, *J. Phys. Chem. Lett.* **2020**, *11*, 8238–8245.

[28] H. Li, T. Yamaguchi, S. Matsumoto, H. Hoshikawa, T. Kumagai, N. L. Okamoto, and T. Ichitsubo, *Nat. Commun.* **2020**, *11*, 1584.

[29] D. Puthusseri, M. Wahid, and S. Ogale, *ACS Omega* **2018**, *3*, 4591–4601.

[30] M. Montanino, S. Passerini, and G. B. Appetecchi, in *Rechargeable Lithium Batteries*, A. A. Franco, Ed. Woodhead Publishing, UK, **2015**, 73–116.

[31] P. Peljo and H. H. Girault, *Energy Environ. Sci.* **2018**, *11*, 2306–2309.

[32] E. Peled, *J. Electrochem. Soc.* **1979**, *126*, 2047–2051.

[33] S. J. An, J. Li, C. Daniel, D. Mohanty, S. Nagpure, and D. L. Wood III., *Carbon* **2016**, *105*, 52–76.

[34] E. Peled, D. Golodnitsky, and G. Ardel, *J. Electrochem. Soc.* **1997**, *144*, L208–L210.

[35] A. Wang, S. Kadam, H. Li, S. Shi, and Y. Qi, *npj Comput. Mater.* **2018**, *4*, 15.

[36] S.-K. Jeong, M. Inaba, Y. Iriyama, T. Abe, and Z. Ogumi, *Electrochem. Solid-State Lett.* **2003**, *6*, A13–A15.

[37] B. Han, Y. Zou, G. Xu, S. Hu, Y. Kang, Y. Qian, J. Wu, X. Ma, J. Yao, T. Li, Z. Zhang, H. Meng, H. Wang, Y. Deng, J. Li, and M. Gu, *Energy Environ. Sci.* **2021**, *14*, 4882–4889.

[38] S. H. Ng, C. Vix-Guterl, P. Bernardo, N. Tran, J. Ufheil, H. Buqa, J. Dentzer, R. Gadiou, M. E. Spahr, D. Goers, and P. Novák, *Carbon* **2009**, *47*, 705–712.

[39] P. Verma, T. Sasaki, and P. Novák, *Electrochim. Acta* **2012**, *82*, 233–242.

[40] Y. P. Wu, C. Jiang, C. Wan, and R. Holze, *Solid state ionics* **2003**, *156*, 283–290.

[41] A. Roglans, A. Pla-Quintana, and M. Moreno-Mañas, *Chem. Rev.* **2006**, *106*, 4622–4643.

[42] P. O'Leary, in *Science of Synthesis, Compounds with Two Carbon-Heteroatom Bonds*, C. A. Ramsden, Ed. Georg Thieme Verlag KG, Stuttgart New York, **2007**, 1361–1400.

[43] D. Hetemi, V. Noël, and J. Pinson, *Biosensors* **2020**, *10*, 4.

[44] J. D. Firth and I. J. S. Fairlamb, *Org. Lett.* **2020**, *22*, 7057–7059.

[45] M. Delamar, R. Hitmi, J. Pinson, and J. M. Savéant, *J. Am. Chem. Soc.* **1992**, *114*, 5883–5884.

[46] J. Pinson and F. Podvorica, *Chem. Soc. Rev.* **2005**, *34*, 429–439.

[47] J. Lehr, B. E. Williamson, and A. J. Downard, *J. Phys. Chem. C* **2011**, *115*, 6629–6634.

[48] C. Martin, M. Alias, F. Christien, O. Crosnier, D. Bélanger, and T. Brousse, *Adv. Mater.* **2009**, *21*, 4735–4741.

[49] P. Verma and P. Novák, *Carbon* **2012**, *50*, 2599–2614.

[50] T. Menanteau, M. Dias, E. Levillain, A. J. Downard, and T. Breton, *J. Phys. Chem. C* **2016**, *120*, 4423–4429.

[51] C. Saby, B. Ortiz, G. Y. Champagne, and D. Bélanger, *Langmuir* **1997**, *13*, 6805–6813.

[52] A. Adenier, E. Cabet-Deliry, A. Chaussé, S. Griveau, F. Mercier, J. Pinson, and C. Vautrin-Ul, *Chem. Mater.* **2005**, *17*, 491–501.

[53] J. C. Lacroix, G. Trippe-Allard, J. Ghilane, and P. Martin, *Adv. Nat. Sci Nanosci. Nanotechnol.* **2014**, *5*, 015001.

[54] J. Pinson, in *Aryl Diazonium Salts: New Coupling Agents in Polymer and Surface Science*, M. M. Chehimi, Ed. Wiley VCH Verlag, Weinheim, **2012**, 1–35.

[55] S. Grimme, *Angew. Chem. Int. Ed.* **2008**, *47*, 3430–3434.

[56] R. P. Matthews, T. Welton, and P. A. Hunt, *Phys. Chem. Chem. Phys.* **2014**, *16*, 3238–3253.

[57] G. R. Desiraju and A. Gavezzotti, *Acta Cryst.* **1989**, *B45*, 473–482.

[58] J. E. Campbell, J. Yang, and G. M. Day, *J. Mater. Chem. C* **2017**, *5*, 7574–7584.

[59] O. M. Yaghi, M. J. Kalmutzki, and C. S. Diercks, *Introduction to Reticular Chemistry: Metal-Organic Frameworks and Covalent Organic Frameworks*, Wiley VCH Verlag, Weinheim, **2019**, xxiii-xxv.

[60] O. M. Yaghi, M. J. Kalmutzki, and C. S. Diercks, in *Introduction to Reticular Chemistry: Metal-Organic Frameworks and Covalent Organic Frameworks*, Wiley VCH Verlag, Weinheim, **2019**, 57–82.

[61] S. Feng and G. Li, in *Modern Inorganic Synthetic Chemistry*, R. Xu, W. Pang, and Q. Huo, Eds. Elsevier, UK, **2011**, 63–95.

[62] I. M. Hauptvogel, V. Bon, R. Grünker, I. A. Baburin, I. Senkovska, U. Mueller, and S. Kaskel, *Dalt. Trans.* **2012**, *41*, 4172–4179.

[63] D. Saha, R. Zacharia, L. Lafi, D. Cossement, and R. Chahine, *Chem. Eng. J.* **2011**, *171*, 517–525.

[64] M. Almáši, V. Zeleňák, R. Gyepes, A. Zukal, and J. Čejka, *Colloids Surfaces A Physicochem. Eng. Asp.* **2013**, *437*, 101–107.

[65] K. Byrne, M. Zubair, N. Zhu, X.-P. Zhou, D. S. Fox, H. Zhang, B. Twamley, M. J. Lennox, T. Düren, and W. Schmitt, *Nat. Commun.* **2017**, *8*, 15268.

[66] N. Zhu, G. Tobin, and W. Schmitt, *Chem. Commun.* **2012**, *48*, 3638–3640.

[67] M. Li and M. Dincă, *J. Am. Chem. Soc.* **2011**, *133*, 12926–12929.

[68] M. Li and M. Dincă, *Chem. Mater.* **2015**, *27*, 3203–3206.

[69] K. Byrne, Synthesis and Physicochemical Characterisation of Metal-Organic Frameworks and Metal-Organic Polyhedra Composed from Extended Organic Ligands, **2019**, Dissertation.

[70] R. Freund, O. Zaremba, G. Arnauts, R. Ameloot, G. Skorupskii, M. Dincă, A. Bavykina, J. Gascon, A. Ejsmont, J. Goscianska, M. Kalmutzki, U. Lächelt, E. Ploetz, C. S. Diercks, and S. Wuttke, *Angew. Chem. Int. Ed.* **2021**, *60*, 23975–24001.

[71] R. J. Kuppler, D. J. Timmons, Q.-R. Fang, J.-R. Li, T. A. Makal, M. D. Young, D. Yuan, D. Zhao, W. Zhuang, and H.-C. Zhou, *Coord. Chem. Rev.* **2009**, *253*, 3042–3066.

[72] G. Cai, P. Yan, L. Zhang, H.-C. Zhou, and H.-L. Jiang, *Chem. Rev.* **2021**, *121*, 12278–12326.

[73] P. P. Bag, G. P. Singh, S. Singha, and G. Roymahapatra, *Eng. Sci.* **2021**, *13*, 1–10.

[74] J. Ren, Y. Huang, H. Zhu, B. Zhang, H. Zhu, S. Shen, G. Tan, F. Wu, H. He, S. Lan, X. Xia, and Q. Liu, *Carbon Energy* **2020**, *2*, 176–202.

[75] M. Bauer, K. Pfeifer, X. Luo, H. Radinger, H. Ehrenberg, and F. Scheiba, *ChemElectroChem* **2022**, *9*, *e202101434*.

[76] M. Bauer, P. Konnerth, H. Radinger, K. Pfeifer, F. Bauer, H. Ehrenberg, and F. Scheiba, **2022**, submitted manuscript.

[77] G. Liu, J. Liu, T. Böcking, P. K. Eggers, and J. J. Gooding, *Chem. Phys.* **2005**, *319*, 136–146.

[78] M. Sandomierski and A. Voelkel, *J. Inorg. Organomet. Polym. Mater.* **2021**, *31*, 1–21.

[79] M. M. Chehimi, A. Lamouri, M. Picot, and J. Pinson, *J. Mater. Chem. C* **2014**, *2*, 356–363.

[80] A. A. Mohamed, Z. Salmi, S. A. Dahoumane, A. Mekki, B. Carbonnier, and M. M. Chehimi, *Adv. Colloid Interface Sci.* **2015**, *225*, 16–36.

[81] N. Delaporte, G. Lajoie, S. Collin-Martin, and K. Zaghib, *Sci. Rep.* **2020**, *10*, 3812.

[82] T. Wu, C. M. Fitchett, P. A. Brooksby, and A. J. Downard, *ACS Appl. Mater. Interfaces* **2021**, *13*, 11545–11570.

[83] H. Saneifar and D. Bélanger, *J. Solid State Electrochem.* **2021**, *25*, 149–158.

[84] Y. R. Leroux and P. Hapiot, *Chem. Mater.* **2013**, *25*, 489–495.

[85] D. S. Moock, S. O. Steinmüller, I. D. Wessely, A. Llevot, B. Bitterer, M. A. R. Meier, S. Bräse, H. Ehrenberg, and F. Scheiba, *ACS Appl. Mater. Interfaces* **2018**, *10*, 24172–24180.

[86] Q. Pan, H. Wang, and Y. Jiang, *J. Mater. Chem.* **2007**, *17*, 329–334.

[87] M. E. Spahr, in *Lithium-Ion Batteries*, 1st ed., M. Yoshio, R. J. Brodd, and A. Kozawa, Eds. Springer, New York, **2009**, 117–154.

[88] M. Widmaier, N. Jäckel, M. Zeiger, M. Abuzarli, C. Engel, L. Bommer, and V. Presser, *Electrochim. Acta* **2017**, *247*, 1006–1018.

[89] M. E. Spahr, D. Goers, A. Leone, S. Stallone, and E. Grivei, *J. Power Sources* **2011**, *196*, 3404–3413.

[90] K. Pfeifer, S. Arnold, Ö. Budak, X. Luo, V. Presser, H. Ehrenberg, and S. Dsoke, *J. Mater. Chem. A* **2020**, *8*, 6092–6104.

[91] A. Sinitskii, A. Dimiev, D. A. Corley, A. A. Fursina, D. V. Kosynkin, and J. M. Tour, *ACS Nano* **2010**, *4*, 1949–1954.

[92] Y. Zhang, C. Liu, W. Shi, Z. Wang, L. Dai, and X. Zhang, *Langmuir* **2007**, *23*, 7911–7915.

[93] K. C. Etika, F. D. Jochum, M. A. Cox, P. Schattling, P. Théato, and J. C. Grunlan, *Macromolecules* **2010**, *43*, 9447–9453.

[94] K. C. Etika, F. D. Jochum, P. Théato, and J. C. Grunlan, *J. Am. Chem. Soc.* **2009**, *131*, 13598–13599.

[95] J. Luan, A. Zhang, Y. Zheng, and L. Sun, *Compos. Part A* **2012**, *43*, 1032–1037.

[96] J. Liu, R. Wang, L. Cui, J. Tang, Z. Liu, Q. Kong, W. Yang, and J. Gooding, *J. Phys. Chem. C* **2012**, *116*, 17939–17946.

[97] H. Shang, G. Peng, W. Liu, H. Zhang, W. Niu, Y. Liao, M. Qu, and Z. Xie, *Energy Technol.* **2020**, *8*, 2000671.

[98] W. Liu, Y. Hu, Y. Qiao, J. Jiang, M. Huang, M. Qu, G. Peng, and Z. Xie, *Solid state ionics* **2021**, *369*, 115724.

[99] T. Nokami, T. Matsuo, Y. Inatomi, N. Hojo, T. Tsukagoshi, H. Yoshizawa, A. Shimizu, H. Kuramoto, K. Komae, H. Tsuyama, and J. Yoshida, *J. Am. Chem. Soc.* **2012**, *134*, 19694–19700.

[100] H. Wang, Z. Li, Z. Meng, X. Guo, Y. Du, and H. Yang, *New J. Chem.* **2021**, *45*, 7060–7064.

[101] S. Bandyopadhyay, C. Singh, P. Jash, H. M. Waseem, A. Paul, and A. Patra, *Chem. Commun.* **2018**, *54*, 6796–6799.

[102] C. Mao, M. Wood, L. David, S. J. An, Y. Sheng, Z. Du, H. M. Meyer III, R. E. Ruther, and D. L. Wood III, *J. Electrochem. Soc.* **2018**, *165*, A1837–A1845.

[103] Y. Jiang, H. Zhao, L. Yue, J. Liang, T. Li, Q. Liu, Y. Luo, X. Kong, S. Lu, X. Shi, K. Zhou, and X. Sun, *Electrochem. commun.* **2021**, *122*, 106881.

[104] J. P. Zhu, X. H. Wang, and X. X. Zuo, *R. Soc. open sci* **2019**, *6*, 190634.

[105] V. Shrivastav, S. Sundriyal, P. Goel, H. Kaur, S. K. Tuteja, K. Vikrant, K.-H. Kim, U. K. Tiwari, and A. Deep, *Coord. Chem. Rev.* **2019**, *393*, 48–78.

[106] A. E. Baumann, D. A. Burns, B. Liu, and V. S. Thoi, *Commun. Chem.* **2019**, *2*, 86.

[107] R. Zhao, Z. Liang, R. Zou, and Q. Xu, *Joule* **2018**, *2*, 2235–2259.

[108] X. Gao, Y. Dong, J. Zhou, L. Wang, and B. Wang, *Electrochem. Energy Rev.* **2020**, *3*, 81–126.

[109] V. K. H. Bui, T. N. Pham, J. Hur, and Y.-C. Lee, *Nanomaterials* **2021**, *11*, 2001.

[110] W. Zhang, L. Du, Z. Chen, J. Hong, and L. Yue, *J. Nanomater.* **2016**, *2016*, 8056302.

[111] T. Li, Y. Bai, Y. Wang, H. Xu, and H. Jin, *Coord. Chem. Rev.* **2020**, *410*, 213221.

[112] Y. Lin, Q. Zhang, C. Zhao, H. Li, C. Kong, C. Shen, and L. Chen, *Chem. Commun.* **2015**, *51*, 697–699.

[113] S.-B. Xia, F.-S. Li, X. Shen, X. Li, F.-X. Cheng, C.-K. Sun, H. Guo, and J.-J. Liu, *Dalt. Trans.* **2018**, *47*, 13222–13228.

[114] L. Bai, B. Tu, Q. Gao, D. Liu, L. Zhizhou, L. Zhao, Q. Li, and Y. Zhao, *Chem. Commun.* **2016**, *52*, 3003–3006.

[115] X. Li, F. Cheng, S. Zhan, and J. Chen, *J. Power Sources* **2006**, *160*, 542–547.

[116] K. Saravanan, M. Nagarathinam, P. Balaya, and J. J. Vittal, *J. Mater. Chem.* **2010**, *20*, 8329–8335.

[117] L. Wang, G. Zhang, Q. Liu, and H. Duan, *Chem. Front.* **2018**, *2*, 1414–1435.

[118] Y. Song, Y. Chen, J. Wu, Y. Fu, R. Zhou, S. Chen, and L. Wang, *J. Alloys Compd.* **2017**, *694*, 1246–1253.

[119] Y. Fu, B. Zhong, Y. Chen, Y. Song, R. Zhou, Y. Song, and S. Chen, *J. Porous Mater.* **2017**, *24*, 613–620.

[120] G. Huang, F. Zhang, X. Du, Y. Qin, D. Yin, and L. Wang, *ACS Nano* **2015**, *9*, 1592–1599.

[121] H. Zhang, Y. Wang, W. Zhao, M. Zou, Y. Chen, L. Yang, L. Xu, H. Wu, and A. Cao, *ACS Appl. Mater. Interfaces* **2017**, *9*, 37813–37822.

[122] R. Li, W. Yue, and X. Chen, *J. Alloys Compd.* **2019**, *784*, 800–806.

[123] K. Cai, Y. Liu, X. Lang, L. Li, Q. Zhang, T. Xu, and D. Chen, *Ionics* **2020**, *26*, 61–67.

[124] Y. Han, P. Qi, J. Zhou, X. Feng, S. Li, X. Fu, J. Zhao, D. Yu, and B. Wang, *ACS Appl. Mater. Interfaces* **2015**, *7*, 26608–26613.

[125] Y. R. Leroux, H. Fei, J.-M. Noel, C. Roux, and P. Hapiot, *J. Am. Chem. Soc.* **2010**, *132*, 14039–14041.

[126] K. L. Parry, A. G. Shard, R. D. Short, R. G. White, J. D. Whittle, and A. Wright, *Surf. Interface Anal.* **2006**, *38*, 1497–1504.

[127] D. Weingarth, M. Zeiger, N. Jäckel, M. Aslan, G. Feng, and V. Presser, *Adv. Energy Mater.* **2014**, *4*, 1400316.

[128] N. Shpigel, M. D. Levi, S. Sigalov, O. Girshevitz, D. Aurbach, L. Daikhin, N. Jäckel, and V. Presser, *Angew. Chem.* **2015**, *127*, 12530–12533.

[129] Y. Zhu, J. Wang, F. Zhang, S. Gao, A. Wang, W. Fang, and J. Jin, *Adv. Funct. Mater.* **2018**, *28*, 1804121.

[130] X. Zheng, R. D. Gandour, and K. J. Edgar, *Biomacromolecules* **2013**, *14*, 1388–1394.

[131] A. Shodiev, E. Primo, O. Arcelus, M. Chouchane, M. Osenberg, A. Hilder, I. Manke, J. Li, and A. A. Franco, *Energy Storage Mater.* **2021**, *38*, 80–92.

[132] S. Kesavan and S. A. John, *RSC Adv.* **2016**, *6*, 62876–62883.

[133] G. Ambrosio, G. Drera, G. Di Santo, L. Petaccia, L. Daukiya, A. Brown, B. Hirsch, S. De Feyter, L. Sangaletti, and S. Pagliara, *Sci. Rep.* **2020**, *10*, 4114.

[134] R. Imhof and P. Novák, *J. Electrochem. Soc.* **1998**, *145*, 1081–1087.

[135] S. S. Zhang, *J. Power Sources* **2006**, *162*, 1379–1394.

[136] M. Bengamra, A. Khlifi, N. Ktari, S. Mahouche-Chergui, B. Carbonnier, N. Fourati, R. Kalfat, and M. M. Chehimi, *Langmuir* **2015**, *31*, 10717–10724.

[137] O. Guselnikova, V. Svorcik, O. Lyutakov, M. M. Chehimi, and P. S. Postnikov, *Sensors* **2019**, *19*, 2110.

[138] S. Ghosh, X. An, R. Shah, D. Rawat, B. Dave, S. Kar, and S. Talapatra, *J. Phys. Chem. C* **2012**, *116*, 20688–20693.

[139] J. D. Velásquez, M. Tomczykowa, M. E. Plonska-Brzezinska, and M. N. Chaur, *Materials* **2020**, *13*, 1141.

[140] E. Y. L. Teo, H. N. Lim, R. Jose, and K. F. Chong, *RCS Adv.* **2015**, *5*, 38111–38116.

[141] A. Celzard, J. F. Marêché, F. Payot, and G. Furdin, *Carbon* **2002**, *40*, 2801–2815.

[142] N. Deprez and D. S. McLachlan, *J. Phys. D Appl. Phys.* **1988**, *21*, 101–107.

[143] R. J. Waltman, *J. Electroanal. Chem.* **1985**, *194*, 49–62.

[144] D. C. Northrop and O. Simpson, *Proc. R. Soc. Lond. A* **1956**, *234*, 124–135.

[145] H. Hu, X. Lou, C. Li, X. Hu, T. Li, Q. Chen, M. Shen, and B. Hu, *Chem., New J.* **2016**, *40*, 9746–9752.

[146] K. Kihara and G. Donnay, *Can. Mineral.* **1985**, *23*, 647–654.

[147] S. J. Yang, S. Nam, T. Kim, J. H. Im, H. Jung, J. H. Kang, S. Wi, B. Park, and C. R. Park, *J. Am. Chem. Soc.* **2013**, *135*, 7394–7397.

[148] D. Wu, Y. Wang, N. Ma, K. Cao, W. Zhang, J. Chen, D. Wang, Z. Gao, F. Xu, and K. Jiang, *Electrochim. Acta* **2019**, *305*, 474–483.

[149] X. H. Huang, X. H. Xia, Y. F. Yuan, and F. Zhou, *Electrochim. Acta* **2011**, *56*, 4960–4965.

[150] J. Fonseca, T. Gong, L. Jiao, and H.-L. Jiang, *J. Mater. Chem. A* **2021**, *9*, 10562–10611.

[151] Y. Ahmad, M. Colin, C. Gerville-Mouravieff, M. Dubois, and K. Guérin, *Synth. Met.* **2021**, *280*, 116864.

[152] M. Walter, M. V. Kovalenko, and K. V. Kravchyk, *New J. Chem.* **2020**, *44*, 1677.

Appendix

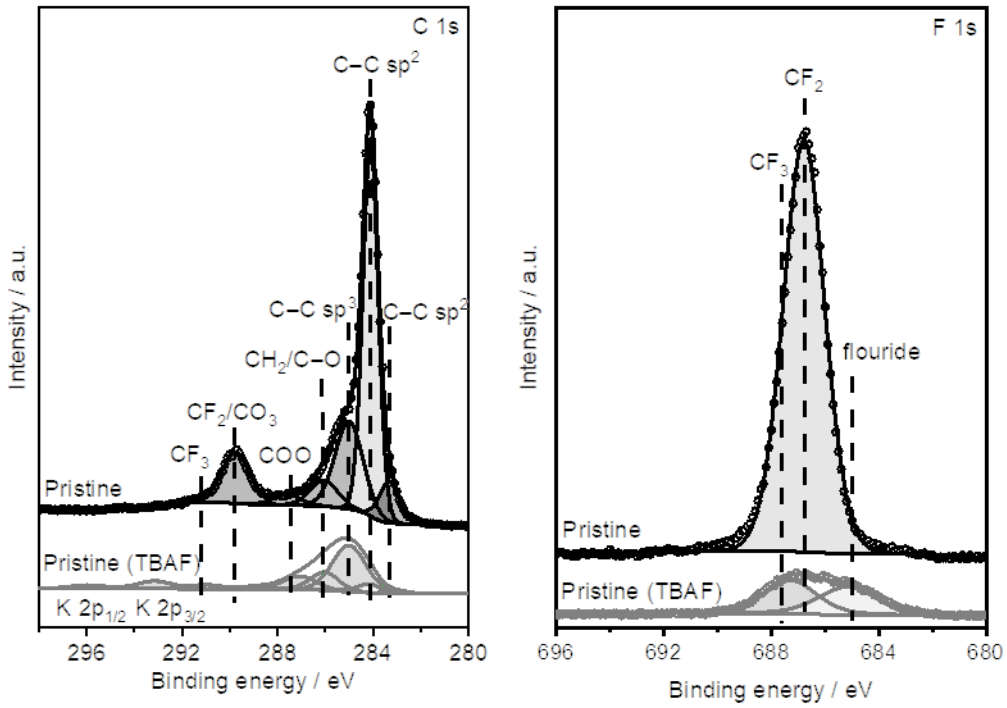

Figure S1. C 1s and F 1s spectra of pristine and with TBAF treated graphite electrodes.

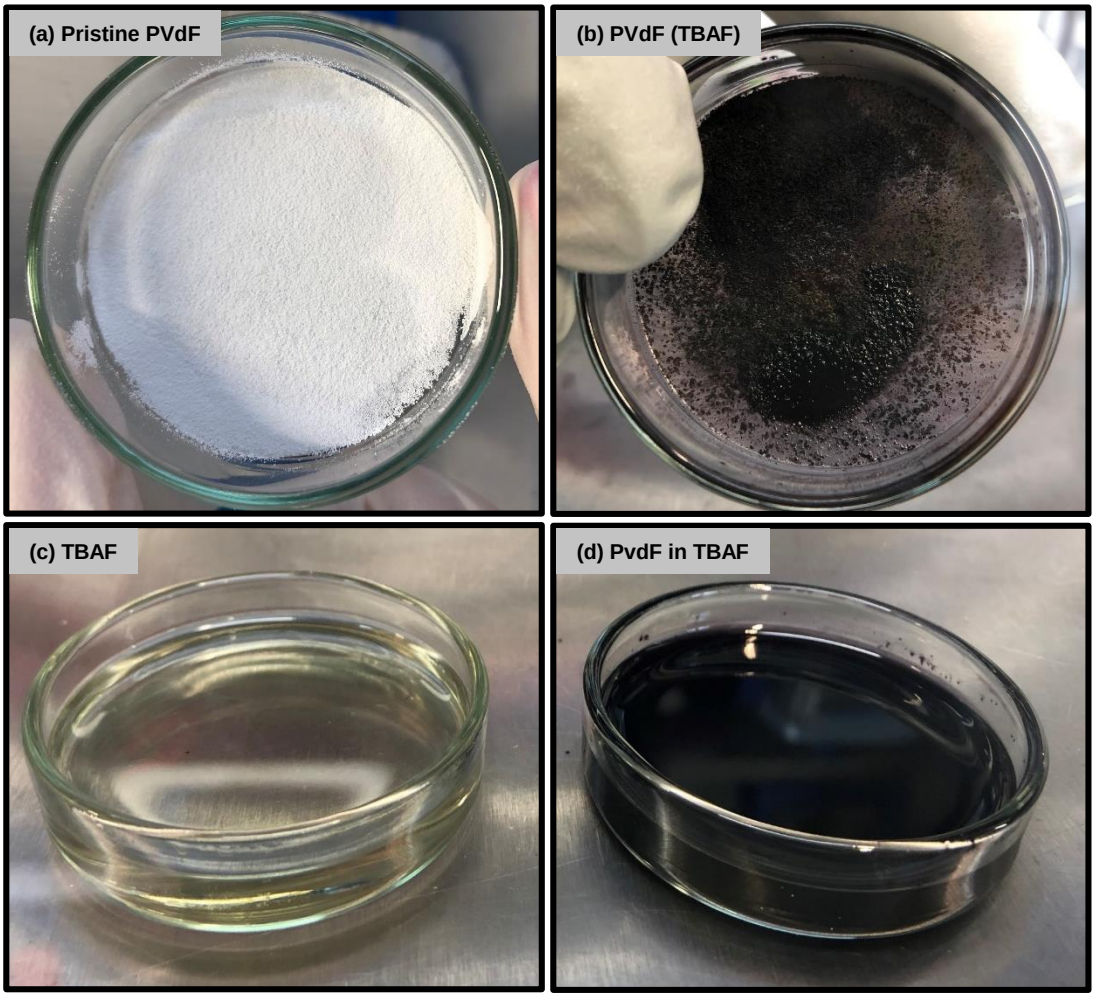

Figure S2. (a) Pristine PVdF powder as purchased, (b) PVdF after immersion in TBAF, (c) TBAF in THF as purchased, (d) PVdF immersed in TBAF.

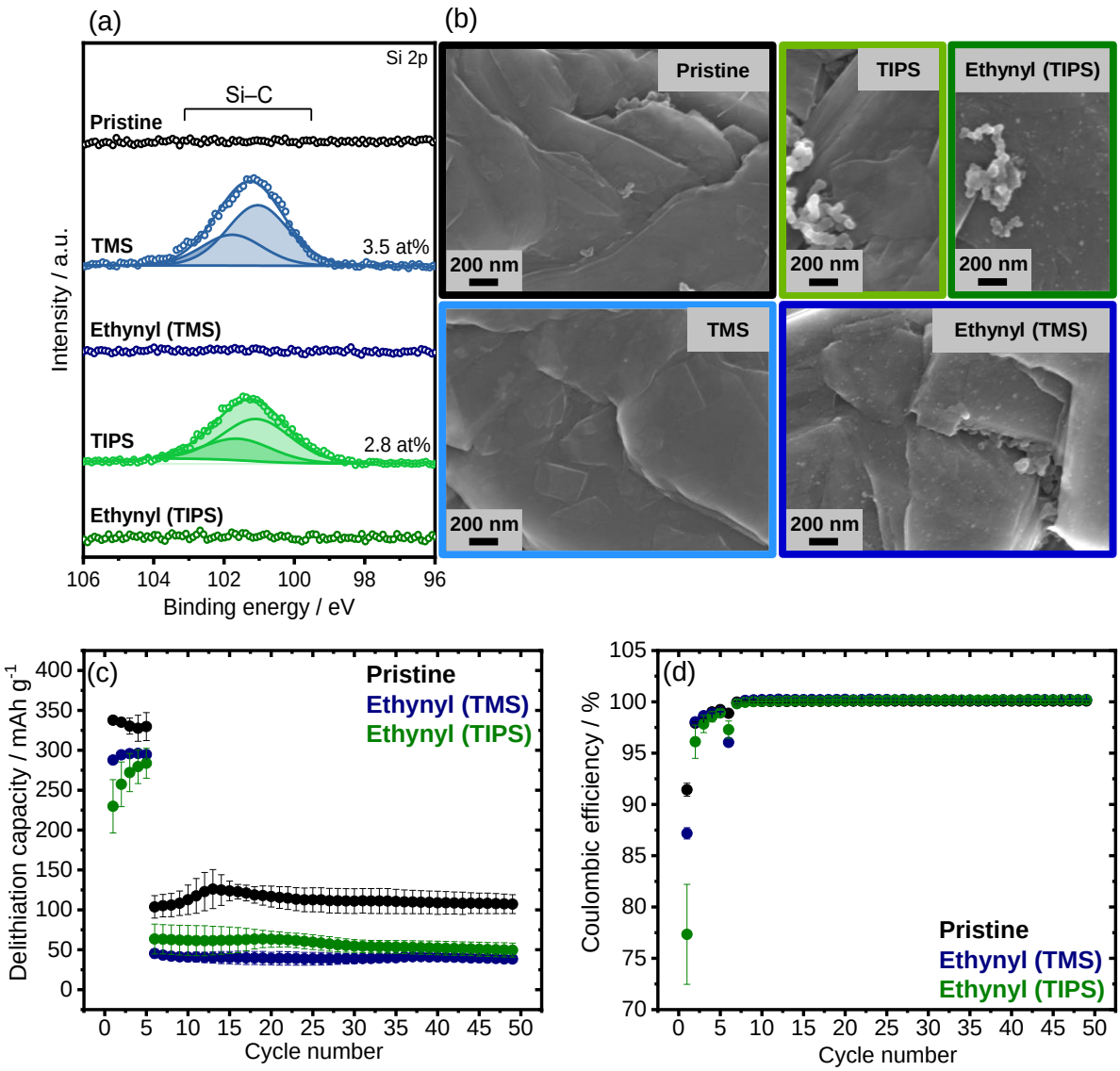

Figure S3. (a) Si 2p spectra and (b) SEM images of pristine graphite, electrografted and deprotected electrodes with CMC/SBR binder, (c) electrochemical cycling stability at C/10 for 5 cycles and 1C for 45 cycles and (d) corresponding Coulombic efficiencies of the pristine and deprotected electrodes with CMC/SBR binder.

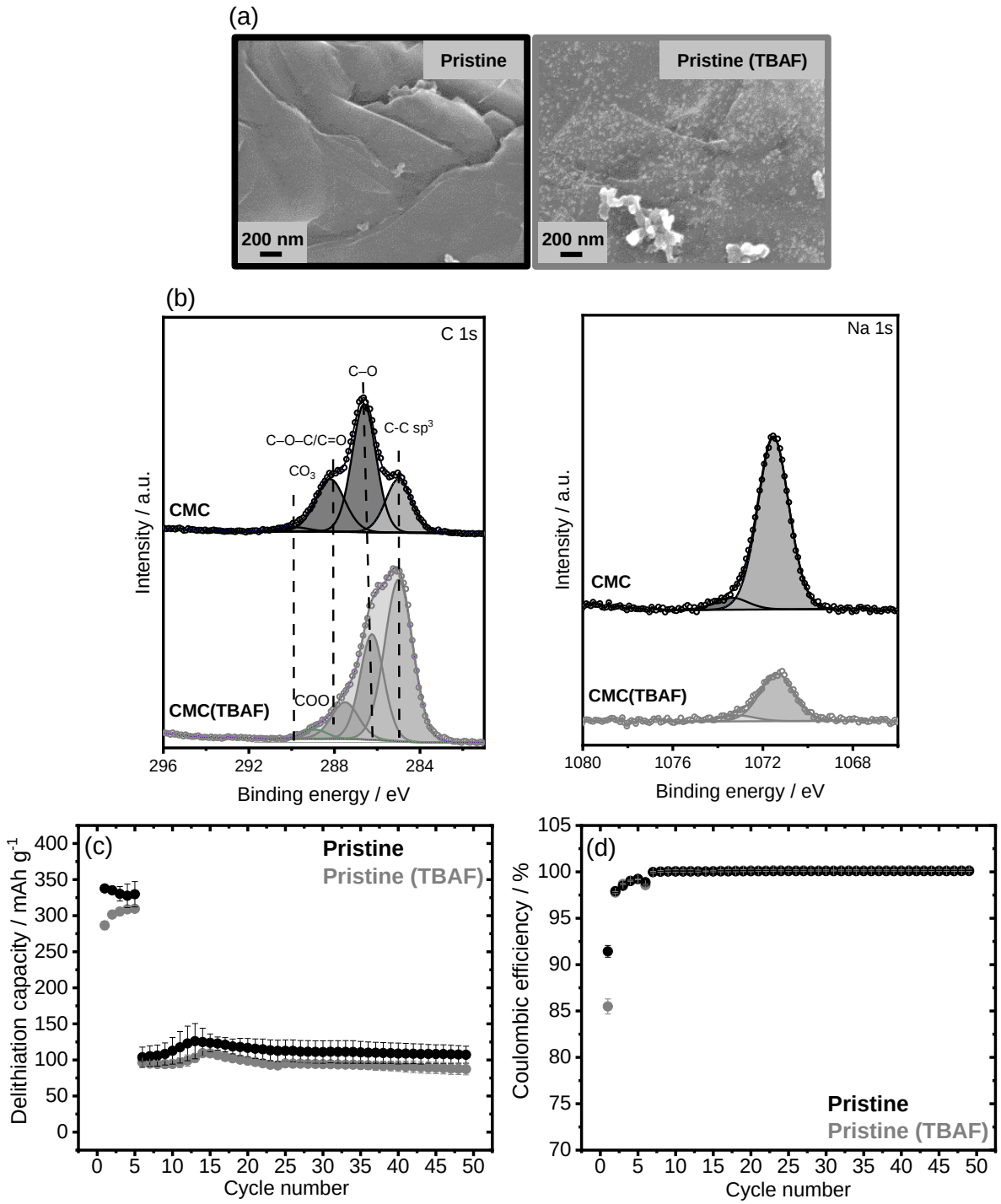

Figure S4. (a) SEM images and (b) C 1s and Na 1s spectra of pristine and with TBAF treated graphite electrodes with CMC/SBR binder, (c) electrochemical cycling stability at C/10 for 5 cycles and 1C for 45 cycles and (d) corresponding Coulombic efficiencies of pristine and with TBAF treated graphite electrode with CMC/SBR binder.

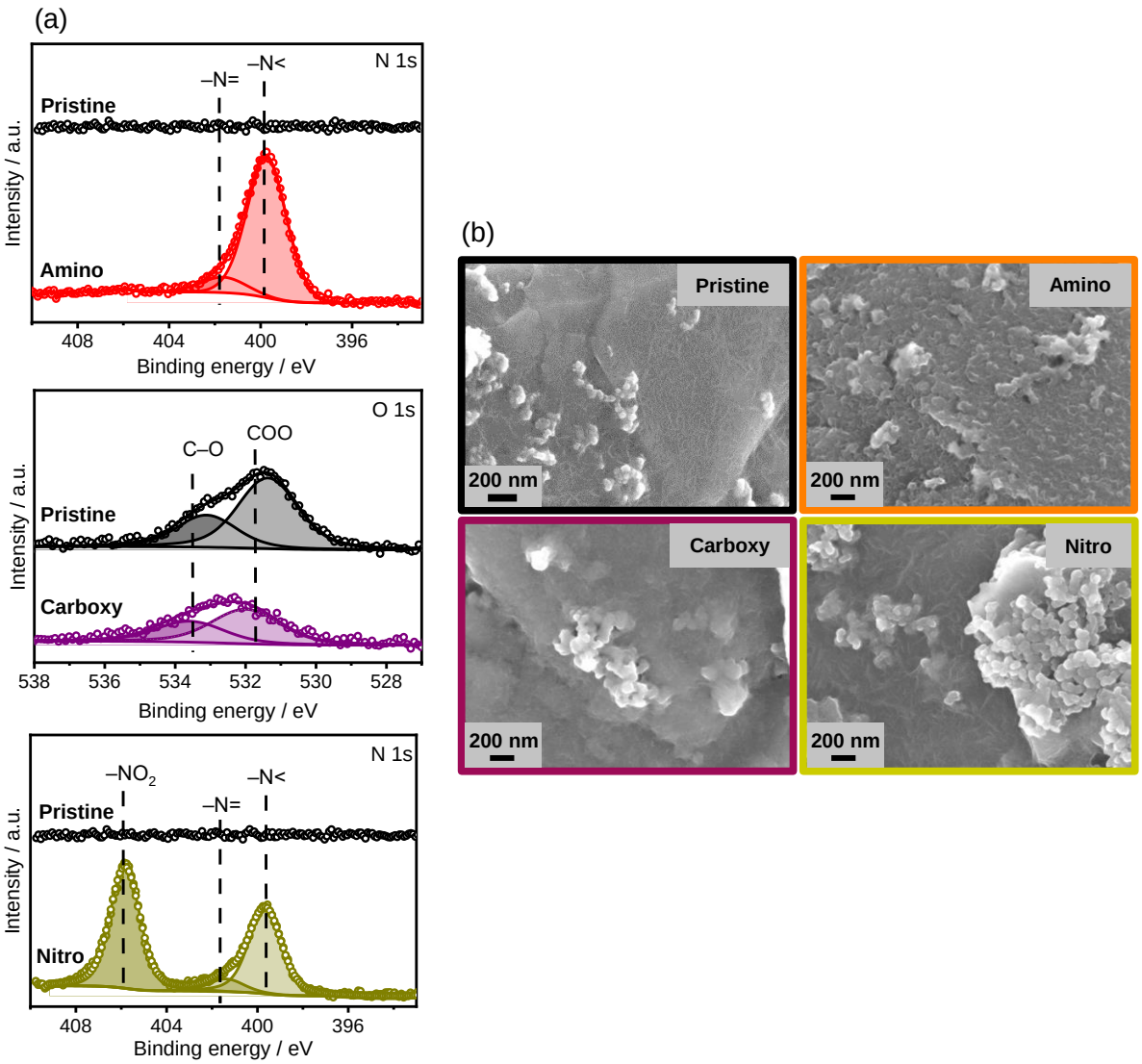

Figure S5. (a) N 1s and O 1s spectra and (b) SEM images of pristine and electrografted amino, carboxy and nitro electrodes.

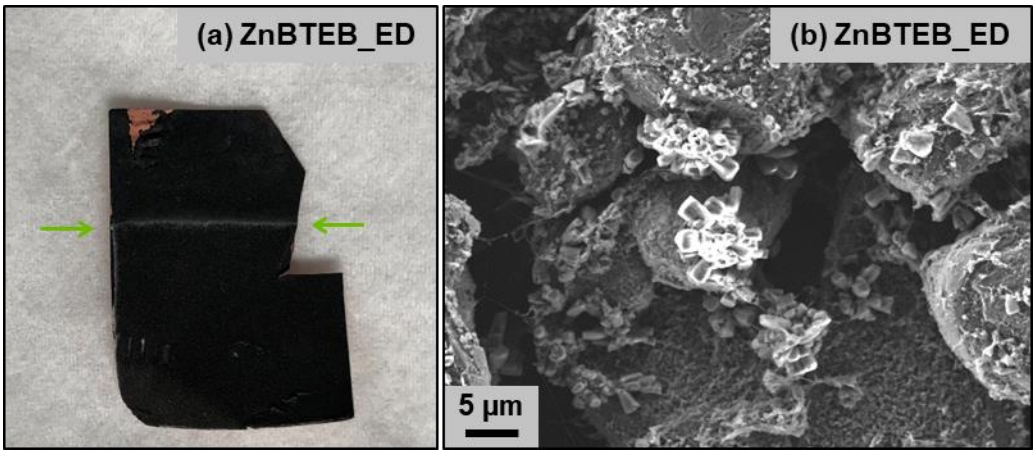

Figure S6. (a) Picture of the ZnBTEB_ED electrode (green arrows mark the white stripe appearing after electrodeposition) and (b) SEM image of ZnBTEB_ED showing crystal-structured islands on the electrode.

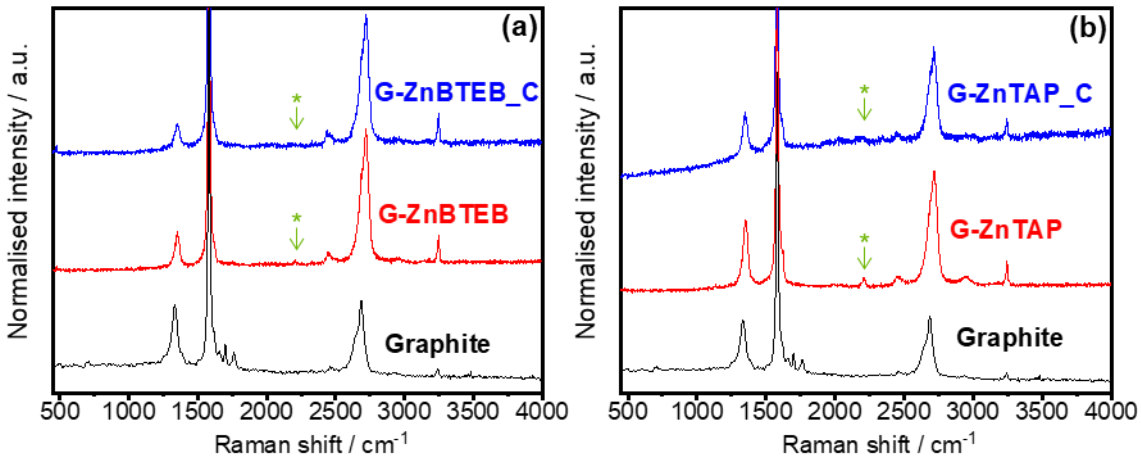

Figure S7. Raman spectra of (a) G-ZnBTEB and G-ZnBTEB_C powder and (b) G-ZnTAP, G-ZnTAP_C powder compared to graphite powder (green asterisks mark the C≡C alkyne vibration at 2211 cm^{-1} of the BTEB and TAP ligand).

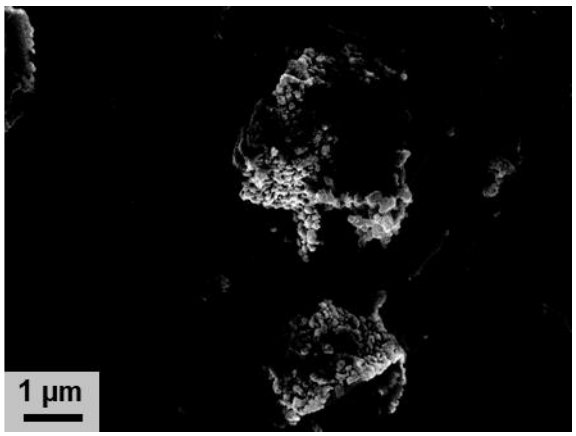

Figure S8. SEM image of a G-ZnBTEB_C electrode recorded with EsB detector (lighter atoms appear darker, heavier atoms appear lighter).

Scientific contributions

Publications

[1] **M. Bauer**, K. Pfeifer, X. Luo, H. Radinger, H. Ehrenberg, F. Scheiba, Functionalisation of graphite electrodes with aryl diazonium salts for lithium-ion batteries, *ChemElectroChem*, **2022**, *9*, e202101434.

[2] **M. Bauer**, P. Konnerth, H. Radinger, K. Pfeifer, F. Bauer, H. Ehrenberg, F. Scheiba, Crucial interactions of pyrene-functionalised graphite for lithium-ion batteries, **2022**, *submitted manuscript*.

[3] Q. Fu, X. Wu, X. Luo, S. Indris, A. Sarapulova, **M. Bauer**, Z. Wang, M. Knapp, H. Ehrenberg, Y. Wei, S. Dsoke, High-voltage aqueous Mg-ion batteries enabled by solvation structure reorganization, *Adv. Funct. Mater.*, **2022**, *32*, 2110674.

[4] H. Zhao, Q. Fu, X. Luo, X. Wu, S. Indris, **M. Bauer**, Y. Wang, H. Ehrenberg, M. Knapp, Y. Wie, Unraveling a Cathode/Anode Compatible Electrolyte for High-Performance Aqueous Rechargeable Zinc Batteries, **2022**, *submitted manuscript*.

Conferences

[1] **M. Bauer**, K. Kutonova, B. Bitterer, R. Azmi, F. Scheiba, Functionalisation of graphite electrodes towards an artificial solid electrolyte interphase, *National Conference, Jena (Germany) – Bunsentagung*, **2019**, Poster Presentation.

[2] **M. Bauer**, K. Kutonova, B. Bitterer, R. Azmi, F. Scheiba, Functionalisation of graphite electrodes towards an artificial solid electrolyte interphase, *International Conference, Durban (South Africa) – International Society of Electrochemistry (ISE)*, **2019**, Poster Presentation.